

Dissertation zur Erlangung des Doktorgrades
der Fakultät für Chemie und Pharmazie
der Ludwig-Maximilians-Universität München

Towards Novel Inorganic Nanosheet
Materials: Exfoliation of Layered
Ruthenium and Iridium Compounds

Daniel Weber

aus

München, Deutschland

2017

Erklärung

Diese Dissertation wurde im Sinne von §7 der Promotionsordnung vom 28. November 2011 von Frau Prof. Dr. Bettina V. Lotsch betreut.

Eidesstattliche Versicherung

Diese Dissertation wurde eigenständig und ohne unerlaubte Hilfe erarbeitet.

München, 12.01.2017

Daniel Weber

Dissertation eingereicht am	12.01.2017
1. Gutachterin:	Prof. Dr. Bettina V. Lotsch
2. Gutachter:	Prof. Dr. Robert Dinnebier
Mündliche Prüfung am	08.02.2017

I've already got the prize:
the prize is the pleasure of finding the thing out, the kick
in the discovery, the observation that other people use it.

– *Richard P. Feynman*

Dedicated to my family & friends.

Dedications

First, I thank Prof. Bettina V. Lotsch for giving me the opportunity to do science in her group and partaking in the exciting endeavor of lab building as her first PhD student in Stuttgart. Afterwards she gave me the freedom necessary to explore and develop my own ideas as well as the means for two conference visits abroad.

Thanks also goes to Prof. Robert Dinnebier for deepening my understanding of diffraction, the determination of crystal structures and being my second adviser, as well as Prof. Konstantin Karaghiosoff, Prof. Karlheinz Sünkel, Prof. Dirk Johrendt and Prof. Hans-Christian Böttcher for being the examiners at my PhD defense.

Eternal gratitude goes to my two friends and mentors Alexander Kuhn and Leslie M. Schoop. Your critical feedback on my divergent thoughts as well as the lessons on convergence were essential to where I am today. Alex: continue to be a great teacher and father! Leslie: Thanks for all the advice on planning, publishing, and politics. Keep up the pace and passion, I am curious how it will all turn out!

I would also like to thank my collaborators on various projects: Matthias Kühne, who always gave a chance to my initial ideas; Soudabeh Mashhadi Sheikholharam, Alex Hoyer, Junhong Na and Marko Burkhard; Nils Richter and Matthias Kläui, Reinhard K. Kremer, Marcus Rose and Regina Palkovits.

Thanks goes to our permanent MPI staff: From Lotsch group - Viola Duppel for a variety of measurements of and conversations on electron diffraction and other topics, Willi Hölle for co-handling the frail old rig otherwise known as the DTA-TG-MS machine, Claudia Kamella for being the group's mother and organizer, Roland for passing along his experience regarding highly energetic solid state synthesis and Marie-Luise Schreiber for the countless ICP-AES measurements and dry solvents. From other groups - Jürgen Nuss for determining crystal structures, Armin Schulz for Raman spectroscopy measurements,

Ulrike Waizmann, Bernhard Fenk, Thomas Reindl and Marion Hagel for taking care of the clean room and Merlin, the chemical service group consisting of Dr. Reinhard Kremer, Eva Brücher, Gisela Siegle and Stefan Höhn for MPMS and PPMS measurements as well as assistance in data interpretation.

Special thanks goes to the 2D subgroup and its alumni: Pirmin Ganter, Tanja Holzmänn, Christian Ziegler and Stephan Werner. Special thanks to Frederik Haase for the many discussions and distractions, may they be of scientific nature or otherwise. Also special thanks to the post-lunch coffee circle and other great conversationalists: Vincent Wing-Hei Lau, Brian Tuffy, Linus Stegbauer, and Filip Podjaski. Thanks to all the other members of the Lotsch group for the great atmosphere.

I would also like to thank the students whom I supervised during my PhD and thank them for their great work: Daniel Wurmbrand, Judith Maria Lippmann, Claudia Göbel, Sarah Mentzel and Nitin Saxena.

Thank you for your friendship and making my time in Stuttgart a pleasant one: Sabrina Graf, Marleen Willig, Henrik Aicher, Lukas Jantschik, John & Emma Gibbs as well as Nico "Heimen" Heiming and Edith Vollmer.

I am grateful to my parents Ester Piravandi and Günter Weber, for their upbringing, patience, the never ending encouragement and wonder about my various interests as well as financial support. In addition, thanks to my brother Michael, his wife Stefanie and my niece Sophia for the joy they give me every time we meet.

And a special thanks goes to Britta Grehl, who kept me levelheaded in a very interesting time of my life. Let's repeat Stuttgart, Prague, Florence, the Great Lakes and everything in between as often and long as we can!

Contents

1	Introduction	1
2	Magnetism in restacked RuCl_3 nanosheets	17
2.1	Introduction	19
2.2	Results and Discussion	22
2.2.1	Preparative procedure and general observations	22
2.2.2	Structural characterization	24
2.2.3	Effect of oxidation	25
2.2.4	Investigations on the magnetism	27
2.3	Conclusion	33
3	Layered Triangular Lattices: $\text{K}_{0.75}\text{Na}_{0.25}\text{IrO}_2$ and IrOOH	39
3.1	Introduction	41
3.2	Experimental	42
3.3	Results and discussion	44
3.3.1	Crystal structure and composition of $\text{K}_{0.75}\text{Na}_{0.25}\text{IrO}_2$	44
3.3.2	Crystal structure and composition of IrOOH	47
3.3.3	Bond valence analysis	51
3.3.4	Physiscal Properties of $\text{K}_{0.75}\text{Na}_{0.25}\text{IrO}_2$ and IrOOH	52
3.4	Conclusion	59

4	$[\text{IrO}_2]^{x-}$ Nanosheets and their Electrocatalytic Properties	65
4.1	Introduction	67
4.2	Results and Discussions	69
4.2.1	Preparation of IrOOH from $\text{K}_{0.75}\text{Na}_{0.25}\text{IrO}_2$	69
4.2.2	Synthesis and structure of $[\text{IrO}_2]^{x-}$ nanosheets	72
4.2.3	Electrochemical characterization of $[\text{IrO}_2]^{x-}$ nanosheets	76
4.3	Conclusion	83
4.4	Experimental	85
4.5	Characterization	87
5	Summary	93
6	Outlook	97
A	Supporting Information on Chapter 2	101
A.1	Synthesis	101
A.2	Single crystal X-ray diffraction	103
A.3	Other analytical methods	103
A.4	Further Results	107
A.4.1	Images of $[\text{RuCl}_3]^{x-}$ and RuCl_3 monolayers	107
A.4.2	TEM data on $[\text{RuCl}_3]^{x-}$ nanosheets	109
A.4.3	Magnetic data and Curie-Weiss fits	110
A.4.4	Specific heat measurement	115
B	Supporting Information on Chapter 3	117
B.1	$\text{K}_{0.75}\text{Na}_{0.25}\text{IrO}_2$	118
B.2	Single crystal X-ray diffraction	118
B.2.1	Band structure	120

B.2.2	Density of states	121
B.3	IrOOH	122
B.3.1	Powder X-ray diffraction	122
B.3.2	Thermogravimetry	123
B.4	Electron dispersive X-ray spectroscopy	124
B.5	Magnetometry data including error bars	125
B.6	Bond valence analysis	126
C	Supporting Information on Chapter 4	129
C.1	AFM images of $[\text{IrO}_2]^{x-}$ nanosheets deposited from undiluted dispersion . .	129
C.2	DTA-TG of $(\text{H, TBA})_x\text{IrO}_2 \cdot y\text{H}_2\text{O}$	129
D	Miscellaneous	131
D.1	List of Publications	131
D.1.1	Publications within this Thesis	131
D.1.2	Publications beyond this Thesis	132
D.2	Conference Contributions & Talks	133
D.3	Curriculum Vitae	136
D.3.1	Personal Details	136
D.3.2	Education	136

List of Figures

1.1	Structure of graphene as well as schematic of electronic structure a) without and b) with 1 % uniaxial strain, redrawn from the literature. ⁵	2
1.2	Structure of MoS ₂ in a) bulk and b) monolayer form as well as schematic of electronic structure, the orange arrow indicates the band gap, redrawn from the literature. ¹⁴	3
1.3	Schematic depiction of frustrated magnetism on the triangular lattice as well as its derivatives; the kagome and honeycomb lattice, the arrows indicate spins.	7
2.1	a) α -RuCl ₃ crystals, scale bar 2 mm, b) Li _{0.2} RuCl ₃ platelets, scale bar 2 mm, c) [RuCl ₃] ^{x-} nanosheet in aqueous dispersion, d) honeycomb structure of α -RuCl ₃ viewed along [001], e) layered structure of α -RuCl ₃ viewed along [010], f) [RuCl ₃] ^{x-} single layer on 270 nm SiO ₂ /Si substrate, imaged by optical microscopy, g) AFM image of highlighted [RuCl ₃] ^{x-} monolayer from optical image with 1.69(9) nm height.	23

2.2	a) In-plane PXRD of α -RuCl ₃ single crystals, [RuCl ₃] ^{x-} and t-RuCl ₃ nanosheet pellets measured in reflection geometry, b) in-plane PXRD of α -RuCl ₃ single crystals, [RuCl ₃] ^{x-} and t-RuCl ₃ nanosheet pellets measured in transmission geometry, inset features the (020) peak of [RuCl ₃] ^{x-} with a Warren-type shape due to turbostratic disorder.	25
2.3	a) TEM bright field image of partially folded [RuCl ₃] ^{x-} on lacey carbon grid, b) SAED pattern of [RuCl ₃] ^{x-} , viewed along the [001] zone axis.	26
2.4	a) In-plane susceptibility (blue) and inverse susceptibility (black) of t-RuCl ₃ nanosheet pellet vs temperature at a field of $\mu_0 H = 1$ T, Curie-Weiss fit as red line, inset shows susceptibility from T = 2 K to 23 K with broad peak at T _N = 7 K, b) out-of-plane data for the same samples measured in a field of $\mu_0 H = 1$ T, inset displays relevant region with no visible peaks in the same scale as a), c) in-plane susceptibility (blue) and inverse susceptibility (black) of α -RuCl ₃ crystal vs temperature at a field of $\mu_0 H = 1$ T, Curie-Weiss fit as red line, inset shows susceptibility from T = 2 K to 23 K with magnetic transitions at T _{N1} = 7 K and T _{N2} = 13 K, d) out-of-plane data for the same α -RuCl ₃ crystal measured in a field of $\mu_0 H = 1$ T, inset displays relevant region between 2 and 23 K.	28
2.5	Evolution of the Weiss temperature θ_{CW} and effective magnetic moment μ_{eff} in-plane (blue) and out-of-plane (green) for α -RuCl ₃ , Li _{0.2} RuCl ₃ , [RuCl ₃] ^{x-} , and t-RuCl ₃ . The dashed lines indicate the general trend between cooperative and non cooperative magnetism, which depends on the electronic state. θ_{CW} values were plotted as absolute values to ease comparability.	29

2.6	Schematic summary of the presented phases, the chemical steps necessary to obtain them and illustrations to explain the differences in the stacking. Simplified molecular orbitals for a monomeric $[\text{RuCl}_6]^{3-}$ complex constituting a RuCl_3 layer visualize the differences in the electronic state and in combination with the stacking, help to explain the evolution of the spin order.	32
3.1	Projection of the unit cell of $\text{K}_{0.75}\text{Na}_{0.25}\text{IrO}_2$ with anisotropic ADPs, displayed along the a) $[201]$ and b) $[001]$ zone axis, c) and d) show the first coordination sphere of the Ir and (K,Na) position.	45
3.2	Optical microscopy (left) and SEM images (right) of $\text{K}_{0.75}\text{Na}_{0.25}\text{IrO}_2$ and IrOOH ; SEM recorded with BSE (left) and SE (right) detection.	46
3.3	a) Comparison of PXRD diffraction patterns of IrOOH and $\text{K}_{0.75}\text{Na}_{0.25}\text{IrO}_2$, b) observed and calculated diffraction pattern of IrOOH as well as the difference curve as determined by Rietveld refinement; ticks mark the positions of reflections for IrOOH and KIr_4O_8	49
3.4	Representation of the crystal structure of IrOOH along the a) $[001]$ and b) $[411]$ zone axis, including hypothetical positions of protons.	50
3.5	Plot of the bond valences of tri-, tetra- and pentavalent iridates containing IrO_6 octahedra against the Ir-O bond length, color denotes structure type, while the shape describes the formal iridium oxidation state; based on data from Table S7 and S8.	52
3.6	Temperature dependent resistivity of $\text{K}_{0.75}\text{Na}_{0.25}\text{IrO}_2$ and IrOOH measured in the range of 40 to 300 K; inset shows Arrhenius plot $\ln \rho(T)$ vs. $10^3/T$ for $\text{K}_{0.75}\text{Na}_{0.25}\text{IrO}_2$	53

3.7	Susceptibility (blue) and inverse susceptibility (black) of a) $\text{K}_{0.75}\text{Na}_{0.25}\text{IrO}_2$ single crystals and b) IrOOH powder measured in a field of $\mu_0 H = 1 \text{ T}$, Curie-Weiss fits shown as a red line.	55
3.8	XPS spectra of the iridium $4f$ states of IrOOH , IrO_2 and IrCl_3	57
4.1	PXRD patterns of $\text{K}_{0.75}\text{Na}_{0.25}\text{IrO}_2$ synthesized at 850°C (black) and after purification by washing with MeOH (blue), as well as $\text{K}_{0.75}\text{Na}_{0.25}\text{IrO}_2$ prepared at 900°C (orange), asterisks the reflections of the side phase. . .	70
4.2	a) PXRD pattern of IrOOH compared to $\text{K}_{0.75}\text{Na}_{0.25}\text{IrO}_2$, b) TEM bright field image and c) SAED diffraction pattern with (hkl) indices of IrOOH , d) simulated SAED pattern based on crystallographic data of IrOOH in the space group $P\bar{3}m1$ along $[001]$ zone axis.	71
4.3	a) Optical microscope and b) AFM image of $[\text{IrO}_2]^{x-}$ nanosheets, inset in a) shows blue aqueous dispersion of $[\text{IrO}_2]^{x-}$ nanosheets, inset in b) displays an exemplary height profile with average height value of a $[\text{IrO}_2]^{x-}$ single layer measured on a $\text{SiO}_2(270 \text{ nm})$ -Si substrate.	73
4.4	a) TEM image and b) SAED pattern of $[\text{IrO}_2]^{x-}$ nanosheets, c) simulated SAED pattern based on crystallographic data from IrOOH in space group $P\bar{3}m1$ along $[001]$ zone axis.	75
4.5	SEM images of $\text{H}_2\text{C}_2\text{O}_4$ -etched Ti substrates with low (a) and high (b) magnification, imaged with SE (left) and BSE (right) detection.	77
4.6	SEM images of $[\text{IrO}_2]^{x-}$ nanosheets on etched Ti substrate, deposition at 160°C	78
4.7	SEM images of $[\text{IrO}_2]^{x-}$ nanosheets applied in different temperature regimes on Ti substrate.	79

4.8	Plot of a) the current density j against the potential with the red dotted line as a visual cue for the readout of j at $\eta = 0.3$ V and b) the overpotential η against the logarithmic representation of the current density j , scan rate was 5 mV sec^{-1} and Ag/AgCl/saturated KCl as a reference electrode. . . .	81
6.1	Number of papers published on the topics 'graphene' and 'nanosheet', from Web of Science. ⁷	98
A.1	Optical microscope and AFM images of $[\text{RuCl}_3]^{x-}$ with height from line scan in purple/orange. The height of a single layer with a hydrate shell is consistently around $1.69(9)$ nm on the wafer and around $1.06(6)$ nm when measured on an underlayer of $[\text{RuCl}_3]^{x-}$	107
A.2	Second set of optical microscope and AFM images of $[\text{RuCl}_3]^{x-}$ with height from line scan in purple. The height of a single layer with a hydrate shell is consistently around $1.69(9)$ nm on the wafer and around $1.06(6)$ nm when measured on an underlayer of $[\text{RuCl}_3]^{x-}$	108
A.3	AFM images of oxidized RuCl_3 monolayer with height from line scan in purple. The height of an oxidized single layer without a hydrate shell is consistently around $0.72(11)$ nm for all measured batches.	108
A.4	a) Selected area electron diffraction pattern of $[\text{RuCl}_3]^{x-}$ along $[001]$ zone axis, b) simulation of $\alpha\text{-RuCl}_3$ based on the space group $C2/m$ obtained from single crystal X-ray diffraction.	109
A.5	In-plane magnetic susceptibility and inverse magnetic susceptibility of $\alpha\text{-RuCl}_3$ vs temperature at $\mu_0 H = 1$ T, inset shows susceptibility from $T = 3$ K to 23 K.	110
A.6	Plot of dMT/dT for $T = 3$ K to 23 K for the in-plane measurement of $\alpha\text{-RuCl}_3$. Magnetization (M) is taken as χH	111

A.7	Out-of-plane magnetic susceptibility and inverse magnetic susceptibility of α -RuCl ₃ vs temperature at $\mu_0 H = 1$ T, inset shows susceptibility from T = 3 K to 23 K. The discontinuity at around 160 K was observed in the literature ⁶ and assumed to be a change in the stacking behavior resulting in a structural phase transition from $C2/m$ to $R\bar{3}$	111
A.8	In-plane magnetic susceptibility and inverse magnetic susceptibility of Li _{0.2} RuCl ₃ vs temperature at $\mu_0 H = 1$ T, inset shows susceptibility from T = 3 K to 23 K.	112
A.9	Out-of-plane magnetic susceptibility and inverse magnetic susceptibility of Li _{0.2} RuCl ₃ vs temperature at $\mu_0 H = 1$ T, inset shows susceptibility from T = 3 K to 23 K.	112
A.10	In-plane magnetic susceptibility and inverse magnetic susceptibility of [RuCl ₃] ^{x-} vs temperature at $\mu_0 H = 1$ T, inset shows susceptibility from T = 3 K to 23 K.	113
A.11	Out-of-plane magnetic susceptibility and inverse magnetic susceptibility of [RuCl ₃] ^{x-} vs temperature at $\mu_0 H = 1$ T, inset shows susceptibility from T = 3 K to 23 K.	113
A.12	In-plane magnetic susceptibility and inverse magnetic susceptibility of t-RuCl ₃ vs temperature at $\mu_0 H = 1$ T, inset shows susceptibility from T = 3 K to 23 K.	114
A.13	Out-of-plane magnetic susceptibility and inverse magnetic susceptibility of t-RuCl ₃ vs temperature at $\mu_0 H = 1$ T, inset shows susceptibility from T = 3 K to 23 K.	114
A.14	Temperature dependent specific heat of t-RuCl ₃ . A magnetic transition is visible at 8.5 K, no further transitions can be detected below 20 K.	115

B.1	Electronic band structure of $\text{K}_{0.75}\text{Na}_{0.25}\text{IrO}_2$ based on FP-LAPW (PBE-GGA) with spin-orbit coupling (SOC), simulated with alkali position fully occupied by K^+	120
B.2	Total density of states in $\text{K}_{0.75}\text{Na}_{0.25}\text{IrO}_2$ calculated with FP-LAPW (PBE-GGA), simulated with alkali position fully occupied by K^+	121
B.3	TG of IrOOH , measured from 30 °C to 200 °C with 2 °C / min in air. . . .	123
B.4	Susceptibility (blue) and inverse susceptibility (black) of a) $\text{K}_{0.75}\text{Na}_{0.25}\text{IrO}_2$ single crystals and b) IrOOH powder measured in a field of $\mu_0 H = 1$ T with error bars based on the standard deviation and R^2 fit parameter of the sample position, Curie-Weiss fits shown as a red line.	125
C.1	Exemplary AFM images of $[\text{IrO}_2]^{x-}$ nanosheets deposited from an undiluted dispersion.	129
C.2	DTA-TG curve of $\text{TBA}_x\text{IrO}_2 \cdot y \text{H}_2\text{O}$ heated in air with 5 K / min to 800 °C, with first derivative of the TG signal as an indicator for mass change processes.	130

List of Tables

1.1	List of experimentally verified and some predicted (*) monolayered compounds as well as references, R denotes organic functionalities.	5
3.1	Interatomic distances (\AA) and angles ($^\circ$) in $\text{K}_{0.75}\text{Na}_{0.25}\text{IrO}_2$ at 250 K. . . .	47
3.2	Interatomic distances (\AA) and angles ($^\circ$) in IrOOH; values without standard deviation were generated by symmetry relation.	48
3.3	Layer heights in $\text{M}(\text{OH})_2$ and MOOH compounds.	50
3.4	Energy of XPS peaks for Ir 4 <i>f</i> states from this work and literature sources.	58
4.1	Comparison of <i>d</i> -values from TEM of a $[\text{IrO}_2]^{x-}$ single layer, TEM of IrOOH microcrystals, PXRD and single crystal X-ray diffraction of $\text{K}_{0.75}\text{Na}_{0.25}\text{IrO}_2$.	74
4.2	Comparison of <i>b</i> , η and, <i>j</i> of the electrodes of bulk IrO_2 , bulk IrOOH, and $[\text{IrO}_2]^{x-}$ nanosheets.	82
4.3	Comparison of η of $[\text{IrO}_2]^{x-}$ nanosheet electrode to values reported in the recent literature or calculated (*) from literature data to fit $j_0 = 10 \text{ mA cm}^{-2}$.	84
A.1	Crystal data and structure refinement data of $\alpha\text{-RuCl}_3$	105
A.2	Atomic coordinates and equivalent displacement parameters U^{eq} ($\text{\AA}^2 \times 10^4$) for $\alpha\text{-RuCl}_3$ at 298 K.	106
A.3	Anisotropic displacement parameters U^{ij} ($\text{\AA}^2 \times 10^4$) for $\alpha\text{-RuCl}_3$ at 298 K.	106

A.4	Comparison of d -values from TEM of a $[\text{RuCl}_3]^x$ single layer, PXRD on the restacked pellet of $[\text{RuCl}_3]^x$ and single crystal X-ray diffraction on α - RuCl_3 .	109
A.5	Weiss temperature θ_{CW} and effective magnetic moment μ_{eff} from Curie-Weiss fits for the in-plane (ip) and out-of-plane (op) direction.	110
B.1	Crystallographic data of $\text{K}_{0.75}\text{Na}_{0.25}\text{IrO}_2$	118
B.2	Atomic coordinates and isotropic displacement parameters U^{iso} (\AA^2) for $\text{K}_{0.75}\text{Na}_{0.25}\text{IrO}_2$ at 250 K; parameters without standard deviation were not refined.	119
B.3	Anisotropic atomic displacement parameters U^{ij} (\AA^2) in $\text{K}_{0.75}\text{Na}_{0.25}\text{IrO}_2$ at 250 K; parameters without standard deviation were not refined.	119
B.4	Crystallographic data of IrOOH	122
B.5	Atomic coordinates and isotropic displacement parameters U^{eq} (\AA^2) for IrOOH at 298 K; parameters without standard deviation were not refined, * marks constrained parameters.	123
B.6	Expected and measured atomic percentages of K, Na, Ir and O averaged over 12 measurements for each $\text{K}_{0.75}\text{Na}_{0.25}\text{IrO}_2$ and IrOOH	124
B.7	List of ternary iridium oxide compounds with tri- and pentavalent iridium, their structure type (ST), formal oxidation state (OS), the bond-valence parameters R_0 and B (both in \AA), ¹ average Ir-O distance \bar{R}_{ij} (in \AA), average bond valence per bond \bar{S}_{ij} and bond valence sum $\sum \bar{S}_{ij}$	126
B.8	Rutile and ternary iridium oxide compounds with tetravalent iridium, their structure type (ST), formal oxidation state (OS), the bond-valence parameters R_0 and B (both in \AA), ¹ average Ir-O distance \bar{R}_{ij} (in \AA), average bond valence per bond \bar{S}_{ij} and bond valence sum $\sum \bar{S}_{ij}$	127

Nomenclature

η	Overpotential [mV]
b	Tafel Slope [mV dec ⁻¹]
j	Current Density [mA cm ⁻²]
j_0	Exchange Current Density [mA cm ⁻²]
p	Pressure [Pa]
T	Temperature [K] or [°C]
2D	two-dimensional
AES	Atomic Emission Spectroscopy
AF	Antiferromagnet, Antiferromagnetic
AFM	Atomic Force Microscope
CVD	Chemical Vapor Deposition
DSA	Dimensionally Stable Anode
EDX	Energy Dispersive X-Ray Spectroscopy
FM	Ferromagnet, Ferromagnetic
ip	in-plane
LDH	Layered Double Hydroxide
OER	Oxygen Evolution Reaction
op	out-of-plane
PXRD	Powder X-Ray Diffraction

QSL	Quantum Spin Liquid
SAED	Selected Area Electron Diffraction
SG	Space Group
SOC	Spin Orbit Coupling
TBA	Tetrabutylammonium $\text{N}(\text{C}_4\text{H}_9)_4^+$
TEM	Transmission Electron Microscope
TMD	Transition-Metal Dichalcogenide

1 On the Monolayers of Inorganic Compounds

The solid state sciences are crucial to the technological advancement of humanity in the last 100 years. The ability to grow large defined arrangements of atoms or ions as single crystals, to determine their structure by diffraction methods and to describe their properties by quantum theory¹ has enabled research into their properties and driven the development of many devices such as the field effect transistor, photovoltaics and new quantum states of matter.² To gain insights into the properties of single crystals, where all the constituting atoms of a similar kind share a similar environment due to translational symmetry, experiments in various temperature (T) and pressure (p) regimes as well as electrical or magnetic fields were conducted. Yet, some critical properties such as chemical reactivity, the wetting of the crystals by liquids or electrochemical properties are specific to surfaces instead of the bulk of the material.

Early on it was established that the atoms at the surfaces of single crystals significantly differ from their bulk counterparts due to their undersaturated coordination. To reduce their energy, the surface either reconstructs under symmetry breaking, for example as known from Si(111),³ or relaxes into a state with similar structural motifs with shorter, stronger bonds. One example are MoS₂ single crystals, where it was early established that the bond length at the surface shrinks by 5 %.⁴ These relaxation processes lead to changes in the electronic structure represented in the band structure diagrams as well as a change in properties.

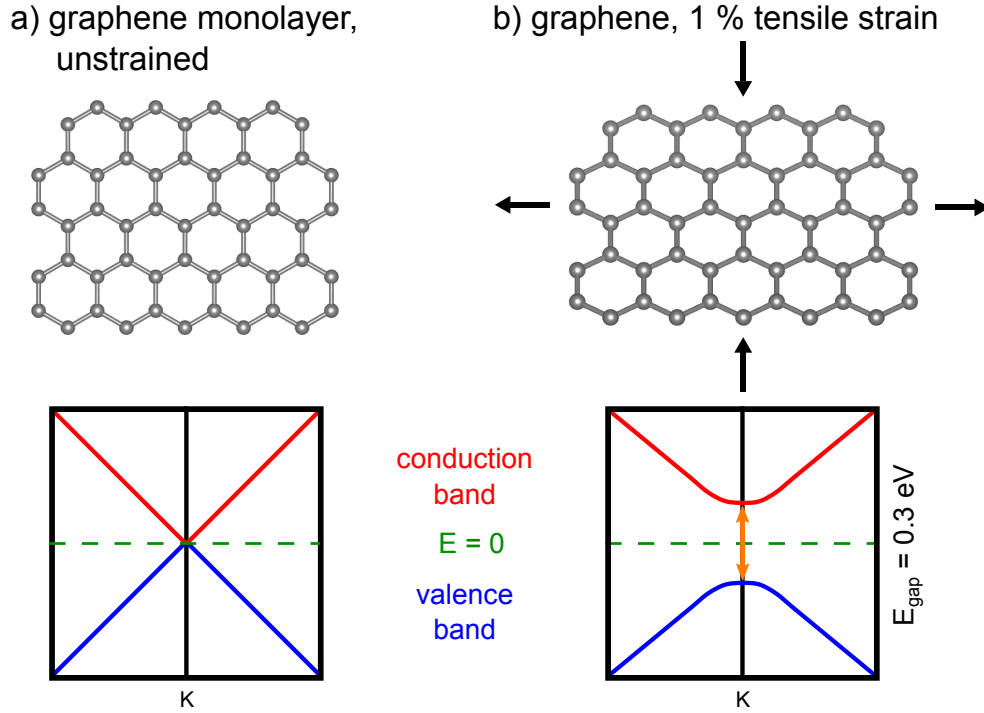


Figure 1.1: Structure of graphene as well as schematic of electronic structure a) without and b) with 1 % uniaxial strain, redrawn from the literature.⁵

These changes are usually overshadowed as the largest part of atoms are contained in the bulk of a compound compared to those that inhabit the surface, but not in single layers of inorganic compounds, which consist only of surface structures. These monolayers show bonding characteristics similar to the surfaces and have been known for some time^{6,7}. In the last 15 years, the interest in monolayers rose sharply once the link between exfoliation of layered compounds and the consequences of the changes of the electronic structure became apparent. The most prominent case is graphene, a single layer of graphite, where exfoliation yielded single layers of carbon in a honeycomb arrangement.⁸ The band structure of graphene has bands that are linearly dispersed when crossing the Fermi level. Therefore the electrons that populate these bands are massless and follow Dirac rather than Schrödinger statistics.⁵ This gives researchers an additional tuning parameter to tailor the electronic structure, which is very sensitive to various parameters. One example is the application of

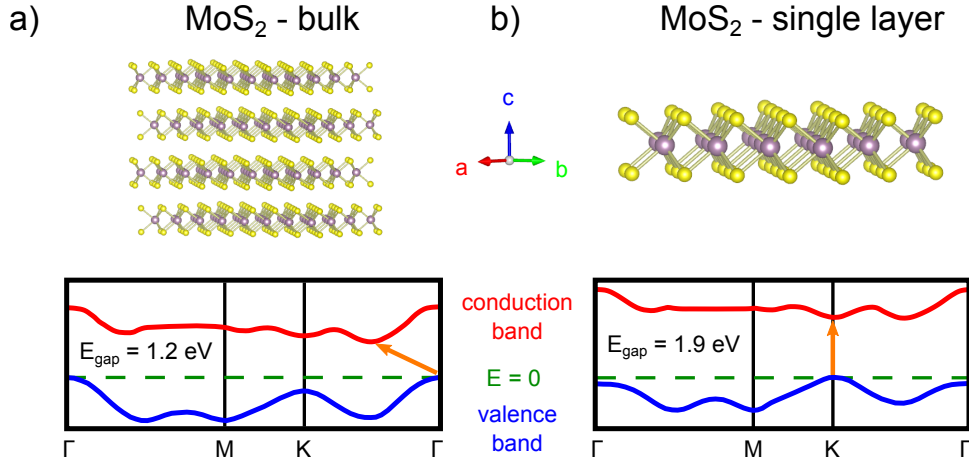


Figure 1.2: Structure of MoS₂ in a) bulk and b) monolayer form as well as schematic of electronic structure, the orange arrow indicates the band gap, redrawn from the literature.¹⁴

uniaxial strain on the monolayer. Upon the deformation of the lattice, the linear dispersion is broken, leading the opening of a band gap and semiconducting behavior.⁹

While exfoliation leads to massless electrons in graphene, it has a different effect on other layered materials depending on their real space and band structure. In MoS₂ and WS₂,^{10–14} exfoliation lowers the position of the band at the Γ -point, which consists of a combination of d -orbital of the transition metal and antibonding p_z orbitals of S, relative to the unaffected bands at the K-point. Thus, the indirect band gap of bulk MoS₂ and WS₂ turns into a direct band gap in the monolayers, vastly increasing the photon absorption compared to the bulk.^{11–13} A schematic representation of the crystal and electronic structure of bulk and monolayer MoS₂ are displayed in Figure 1.2.

Another example for the property changes in monolayers due to the proximity of electron density is seen by the variation of the electron mobility of graphene measured on different substrates. When placed on SiO₂, which has a rough surface as well as an inhomogeneous charge-density distribution due to impurities, the electrons scatter at these ”charge puddles” and the mobility drops.¹⁵ The reversed trend is observed when graphene is sandwiched between layers of highly crystalline hexagonal BN.¹⁶ As h-BN has a smooth

surface as well as a homogeneous charge distribution, the electron mobility is close to the ideal one predicted by theory.

The sensitivity of the electronic structure to proximate electron density, photo-activation of charge carriers, spin polarisation under circular light illumination¹⁷, mechanical flexibility to bending yet strength against tear sparked various ideas for applications of conductive two-dimensional (2D) graphene and transition-metal dichalcogenides (TMDs) as active components in electrical devices, sensors, battery electrodes, conductive part for hybrids with otherwise insulating materials as well as materials for spin- instead of electron based electronics.^{18–21} To satisfy the anticipated demand for monolayer materials as well as extend the library of available properties, research efforts lead to a library of various, exfoliated layered compounds. Examples of verified monolayer compounds as well as some compounds predicted by theory relevant to this work are summarized in Table 1.1.^{10,22} Four synthetical routes were established, two based on chemical reactions, and two based on the application of mechanical force.

The first is called chemical exfoliation and relies on osmotic pressure created by the solvation of cations present in the interlayer space. These are either present in the parent compound²⁷, introduced by exchanging non-solvateable cations for solvateable ones⁴¹ or intercalated by redox reactions, i.e. lithium insertion by reaction of the layered compound with butyl-lithium or LiBH_4 with a concomitant reduction of the layer constituents.⁶ The second route is chemical vapor deposition (CVD), where a metal precursor compound like MoO_3 is volatilized in the presence of a gaseous species containing the anion of the desired product, i.e. sulfur vapors for MoS_2 .⁶⁶ The single layers are then deposited on a substrate, depending on a specific set of conditions regarding temperature, total and partial pressures, flow velocity as well as substrate termination. In the liquid phase exfoliation technique, exfoliation is achieved by applying shear forces onto the layered bulk in the presence of a solvent with a surface energy in the range of the van-der-Waals interlayer forces.⁶⁷ The

Table 1.1: List of experimentally verified and some predicted (*) monolayered compounds as well as references, R denotes organic functionalities.

<u>Elemental</u>	<u>Nitrides</u>	<u>Other Chalcogenides</u>
graphene ⁸	BN, hexagonal ²³	Bi ₂ Se ₃ ²⁴
borophene, on Ag(111) ²⁵	<u>TMDs</u>	SnS ₂ ²⁶ , [Sn _{1-x} S ₂] ^{4x-27}
silicene, on Ag(111) ²⁸	MoS ₂ ^{6,29}	TiS ₃ ³⁰
phosphorene ³¹	MoSe ₂ ³²	MnPS ₃ ³³ , NiPS ₃ ³⁴
stanene, on Ag(111) ³⁵	MoTe ₂ ³⁶	CrSiTe ₃ ³⁷
<u>Halides</u>	<u>WS₂⁷</u>	<u>Oxides & Hydroxides</u>
CrX ₃ * ^{38,39}	WSe ₂ ⁴⁰	[Ti _{0.92} O ₂] ^{0.7-41}
α -RuCl ₃ * ³⁸	WTe ₂ ⁴²	[MnO ₂] ^{x-43}
BiI ₃ * ^{38,44}	VS ₂ ⁴⁵	[CoO ₂] ^{x-46}
<u>Hydrides</u>	<u>VSe₂⁴⁷</u>	<u>[MoO₂]^{x-48}</u>
CH _x ⁴⁹	NbS ₂ ⁵⁰	[RuO ₂] ^{x-51}
GeH ⁵²	NbSe ₂ ²⁹	W ₂ O ₇ ²⁻⁵³
<u>Functionalized</u>	<u>TaS₂⁵⁴</u>	<u>Cs₄W₁₁O₃₆²⁻⁵⁵</u>
Ge-(H,R) ⁵⁶	TaSe ₂ ⁵⁴	various oxide
MoS ₂ -R ⁵⁷	TiS ₂ ⁵⁴	perovskites ^{58,59}
<u>Others</u>	<u>TiSe₂⁶⁰</u>	<u>various layered double</u>
MXenes ^{61,62}	ZrS ₂ ⁵⁴	hydroxides (LDH) ⁶³
Oxypnictides ⁶⁴	ReS ₂ ⁶⁵	

single layers then get stabilized by interacting with the solvent. The last technique is mechanical cleavage, where interlayer forces are overcome by the use of an adhesive tape.⁸

In van der Waals compounds such as graphite and TMDs, all techniques mentioned above yield nanosheets ranging from single layers to few layered stacks. Yet, the yield of few single layers and a broad layer number distribution are typical for mechanical cleavage and liquid phase exfoliation techniques. CVD requires substrates of smooth surfaces able to withstand high heat as well as low pressures. As scale-up requires a good yield of monolayers, chemical exfoliation is key.

Incidentally, chemical exfoliation is also the technique which allows the exfoliation of oxides and hydroxides, which do not feature a van der Waals gap, but are held together by the Coulomb force between the polyionic layers and counterions present in the interlayer space.^{41,46,51,63,68,69} In these material classes, the strong Coulomb interaction impedes exfoliation attempts by the application of mechanical force. CVD is not possible due to the high evaporation temperature of oxides as well as the dehydration of LDHs at elevated temperatures. Yet, the exfoliation of these layered compounds offers materials with a set of properties complementary to the conductive graphene and TMD materials which typically feature band gaps of up to 2 eV. In oxides and hydroxides, the metal cation-anion interaction is more ionic, which leads to electronic structures with band gaps of up to 5 eV, filling the band gap region between 1.8 eV of MoS₂ and 6.5 eV of BN. Especially the high band gap insulators are less sensitive to variations of their electronic behavior and feature a high resistance to chemical attacks and high temperatures even in monolayer form. Therefore, the oxide and hydroxide nanosheets are discussed as photoelectrocatalysts in water splitting as well as for applications as insulating layers in electronics.^{58,63}

Another class of compounds, which has received little attention so far, are halides. Especially in chlorides, the hardness of the anion should be an intermediate between the hard O²⁻ and the relatively soft S²⁻ anion, and there exist van der Waals compounds

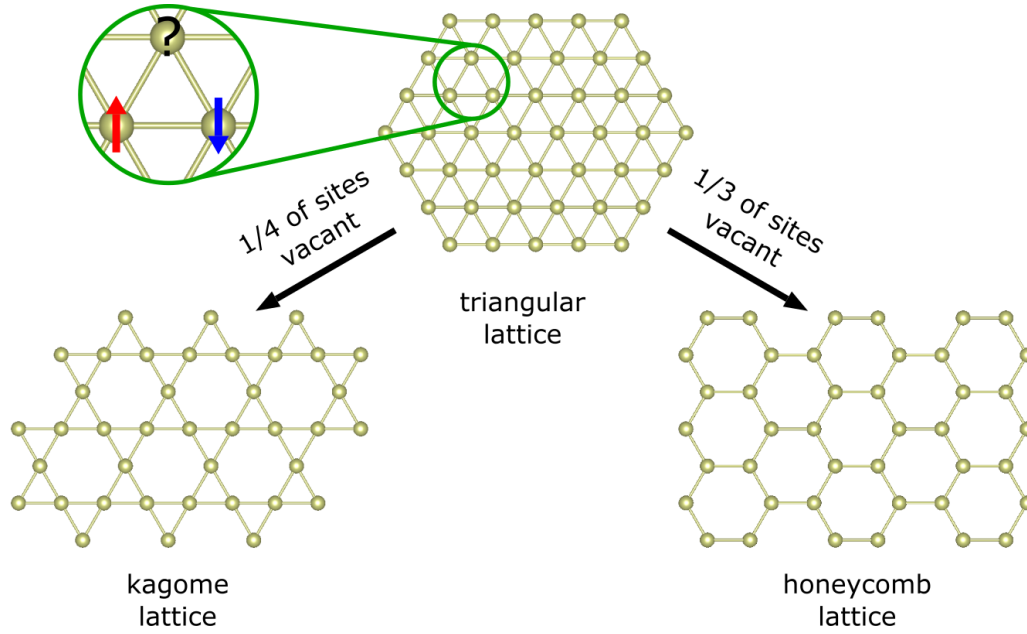


Figure 1.3: Schematic depiction of frustrated magnetism on the triangular lattice as well as its derivatives; the kagome and honeycomb lattice, the arrows indicate spins.

such as CrCl_3 and $\alpha\text{-RuCl}_3$. Hypothetically, these could combine the lack of unscreened Coulomb potential from TMDs with the stability of the oxide monolayers.

The other major factor influencing the electronic behavior as well as structure and magnetic behavior of monolayers is the electron configuration of the cation. In MoS_2 , the Mo^{4+} ion is trigonal prismatic coordinated by six S^{2-} , which is known as the 2H-phase. The injection of electron density into the layer, for example by exfoliation by lithium insertion, leads to a phase transition to the 1T-phase, which hosts molybdenum ions in an octahedral coordination.^{70,71} This phase change is accompanied by a transition from semiconducting to metallic behavior with drastic implications for the catalytic properties. In electrocatalytic water splitting, the catalytically active sites sit at the edge of 2H- MoS_2 and have a Tafel slope of 80 mV dec^{-1} , while in the 1T-phase, the whole monolayer becomes catalytically active with a drastically decreased Tafel slope of 40 mV dec^{-1} . Therefore, the exfoliation does not only affect the conductivity, but also increases the number of active sites.⁷²

Frustrated magnetism is another property where the parameter control offered by the exfoliation of 2D compounds can spark interesting investigations. In geometrically frustrated magnets, the spins try to order in an antiferromagnetic lattice, where the magnetic interactions to the next neighbor are of opposite sign. Yet, due to symmetry restrictions based on the triangular and kagome lattice of the magnetic ions, such an arrangement cannot result in an antiferromagnetic order, which leads to a suppression of the ordering phenomenon.⁷³ In honeycombs, the spins could order antiferromagnetically, but interactions with the second coordination sphere counterbalance those of the first, leading to frustration by a slightly different mechanism.⁷⁴ A schematic of the geometric suppression mechanism as well as of the three lattices is depicted in Figure 1.3. In real compounds, interlayer interactions usually introduce additional interactions, which allows a system to order. By exfoliating these layered compounds and suspending them in vacuum additional interlayer interactions can be excluded, potentially opening up a platform for investigations into interlayer effects in magnetically frustrated systems.

Objectives The main goal of this thesis was the preparation of inorganic monolayers of novel compositions and properties. Two strategies were pursued. While the first one was based on the synthesis of monolayers with unprecedented halide anions, the second strategy focused on the preparation of cations with interesting electron and spin configurations, which are either applicable for catalysis or, combined with the triangular based structural motifs, promote magnetic frustration for potential applications in spin-based electronics.

α -RuCl₃ represents a new candidate for the realization of the quantum spin liquid (QSL) state due to the honeycomb arrangement of Ru³⁺ with its 4d⁵ electron configuration ($S = \frac{1}{2}$).^{75–79} As the QSL state stays elusive due to interactions between the RuCl₃ layers, a single layer potentially offers a possibility to investigate the influence of the interlayer magnetic interactions on the magnetic phase diagram by decoupling the layers from each other.

This additional degree of freedom in tuning the magnetic interactions in RuCl_3 should be particularly relevant to the growing community of researchers currently interested in bulk $\alpha\text{-RuCl}_3$.⁸⁰ The investigations on the preparation of single layered RuCl_3 and of its restacked pellet are presented in chapter 2.

Another class of compounds with interesting properties for frustrated magnetism as well as electrocatalytic water splitting are iridates with an iridium valency of four or higher. There, the oxidation state of iridium and the character of the iridium-oxygen bond are crucial for the interpretation of the observed behavior. Lower valencies and thus longer iridium-oxygen bonds are rare due to the influence of the relativistic effect on the orbitals of iridium, but represent an important cornerstone for the understanding of the bonding in ternary and quaternary iridates. In chapter 3, the structure, electric, magnetic and ion exchange properties of the new layered alkali iridate with the composition $\text{K}_{0.75}\text{Na}_{0.25}\text{IrO}_2$ are investigated.

Binary and ternary iridium oxide compounds are among the best electrocatalysts for water oxidation under a wide set of conditions. As the overpotential necessary to drive the water splitting reaction varies with the highest and lowest valence state of the metal oxide as well as the active surface area, bulk IrOOH was exfoliated into $[\text{IrO}_2]^{x-}$ nanosheets to increase the surface area. After investigations on the structural integrity of the nanosheets, their electrocatalytic behavior as well as that of IrOOH and IrO_2 were characterized in chapter 4.

References

- [1] Hoddeson, L.; Braun, E.; Teichmann, J.; Weart, S. *Out of the Crystal Maze: Chapters from the History of Solid State Physics*, 1st ed.; Oxford University Press: New York, USA, 1992.

-
- [2] Bradlyn, B.; Cano, J.; Wang, Z.; Vergniory, M. G.; Felser, C.; Cava, R. J.; Bernevig, B. A. *Science* **2016**, *353*.
- [3] Binnig, G.; Rohrer, H.; Gerber, C.; Weibel, E. *Physical Review Letters*. **1983**, *50*, 120.
- [4] Mrstik, B. J.; Kaplan, R.; Reinecke, T. L.; Van Hove, M.; Tong, S. Y. *Phys. Rev. B* **1977**, *15*, 897.
- [5] Novoselov, K.; Geim, A. K.; Morozov, S.; Jiang, D.; Katsnelson, M.; Grigorieva, I.; Dubonos, S.; Firsov, A. *Nature* **2005**, *438*, 197–200.
- [6] Joensen, P.; Frindt, R.; Morrison, S. R. *Materials Research Bulletin* **1986**, *21*, 457–461.
- [7] Yang, D.; Frindt, R. *Journal of Physics and Chemistry of Solids* **1996**, *57*, 1113–1116.
- [8] Novoselov, K. S.; Geim, A. K.; Morozov, S. V.; Jiang, D.; Zhang, Y.; Dubonos, S. V.; Grigorieva, I. V.; Firsov, A. A. *Science* **2004**, *306*, 666–669.
- [9] Ni, Z. H.; Yu, T.; Lu, Y. H.; Wang, Y. Y.; Feng, Y. P.; Shen, Z. X. *ACS Nano* **2008**, *2*, 2301–2305.
- [10] Wang, Q. H.; Kalantar-Zadeh, K.; Kis, A.; Coleman, J. N.; Strano, M. S. *Nature Nanotechnology* **2012**, *7*, 699–712.
- [11] Lee, C.; Yan, H.; Brus, L. E.; Heinz, T. F.; Hone, J.; Ryu, S. *ACS Nano* **2010**, *4*, 2695–2700.
- [12] Conley, H. J.; Wang, B.; Ziegler, J. I.; Haglund, R. F.; Pantelides, S. T.; Bolotin, K. I. *Nano Lett.* **2013**, *13*, 3626–3630.
- [13] Rice, C.; Young, R. J.; Zan, R.; Bangert, U.; Wolverson, D.; Georgiou, T.; Jalil, R.; Novoselov, K. S. *Phys. Rev. B* **2013**, *87*, 081307.

- [14] Kuc, A.; Zibouche, N.; Heine, T. *Physical Review B* **2011**, *83*, 245213.
- [15] Nagashio, K.; Yamashita, T.; Nishimura, T.; Kita, K.; Toriumi, A. *J. Appl. Phys.* **2011**, *110*, 024513.
- [16] Gannett, W.; Regan, W.; Watanabe, K.; Taniguchi, T.; Crommie, M. F.; Zettl, A. *Applied Physics Letters* **2011**, *98*.
- [17] Ganichev, S.; Ivchenko, E.; Bel’Kov, V.; Tarasenko, S.; Sollinger, M.; Weiss, D.; Wegscheider, W.; Prettl, W. *Nature* **2002**, *417*, 153–156.
- [18] Ferrari, A. C. et al. *Nanoscale* **2015**, *7*, 4598–4810.
- [19] Novoselov, K. S.; Fal’ko, V. I.; Colombo, L.; Gellert, P.; Schwab, M.; Kim, K. *Nature* **2012**, *490*, 192–200.
- [20] Traversi, F.; Raillon, C.; Benameur, S.; Liu, K.; Khlybov, S.; Tosun, M.; Krasnozhan, D.; Kis, A.; Radenovic, A. *Nature Nanotechnology* **2013**, *8*, 939–945.
- [21] Sarkar, D.; Liu, W.; Xie, X.; Anselmo, A. C.; Mitragotri, S.; Banerjee, K. *ACS Nano* **2014**, *8*, 3992–4003.
- [22] Miró, P.; Audiffred, M.; Heine, T. *Chem. Soc. Rev.* **2014**, *43*, 6537.
- [23] Song, L.; Ci, L.; Lu, H.; Sorokin, P. B.; Jin, C.; Ni, J.; Kvashnin, A. G.; Kvashnin, D. G.; Lou, J.; Yakobson, B. I.; Ajayan, P. M. *Nano Letters* **2010**, *10*, 3209–3215.
- [24] Sun, Y.; Cheng, H.; Gao, S.; Liu, Q.; Sun, Z.; Xiao, C.; Wu, C.; Wei, S.; Xie, Y. *Journal of the American Chemical Society* **2012**, *134*, 20294–20297.
- [25] Mannix, A. J.; Zhou, X.-F.; Kiraly, B.; Wood, J. D.; Alducin, D.; Myers, B. D.; Liu, X.; Fisher, B. L.; Santiago, U.; Guest, J. R.; Yacaman, M. J.; Ponce, A.; Oganov, A. R.; Hersam, M. C.; Guisinger, N. P. *Science* **2015**, *350*, 1513–1516.

- [26] Sun, Y.; Cheng, H.; Gao, S.; Sun, Z.; Liu, Q.; Liu, Q.; Lei, F.; Yao, T.; He, J.; Wei, S.; Xie, Y. *Angewandte Chemie International Edition* **2012**, *51*, 8727–8731.
- [27] Kuhn, A.; Holzmann, T.; Nuss, J.; Lotsch, B. V. *Journal of Materials Chemistry A* **2014**, *2*, 6100–6106.
- [28] Vogt, P.; De Padova, P.; Quaresima, C.; Avila, J.; Frantzeskakis, E.; Asensio, M. C.; Resta, A.; Ealet, B.; Le Lay, G. *Phys. Rev. Lett.* **2012**, *108*, 155501.
- [29] Novoselov, K. S.; Jiang, D.; Schedin, F.; Booth, T. J.; Khotkevich, V. V.; Morozov, S. V.; Geim, A. K. *Proceedings of the National Academy of Sciences* **2005**, *102*, 10451–10453.
- [30] Island, J. O.; Barawi, M.; Biele, R.; Almazn, A.; Clamagirand, J. M.; Ares, J. R.; Snchez, C.; van der Zant, H. S. J.; lvarez, J. V.; D’Agosta, R.; Ferrer, I. J.; Castellanos-Gomez, A. *Advanced Materials* **2015**, *27*, 2595–2601.
- [31] Li, L.; Yu, Y.; Ye, G. J.; Ge, Q.; Ou, X.; Wu, H.; Feng, D.; Chen, X. H.; Zhang, Y. *Nature Nanotechnology* **2014**, *9*, 372–377.
- [32] Gordon, R. A.; Yang, D.; Crozier, E. D.; Jiang, D. T.; Frindt, R. F. *Physical Review B* **2002**, *65*, 125407.
- [33] Li, X.; Wu, X.; Yang, J. *Journal of the American Chemical Society* **2014**, *136*, 11065–11069.
- [34] Jenjeti, R. N.; Austeria, M. P.; Sampath, S. *ChemElectroChem* **2016**, *3*, 1392–1399.
- [35] Zhu, F.-f.; Chen, W.-j.; Xu, Y.; Gao, C.-l.; Guan, D.-d.; Liu, C.-h.; Qian, D.; Zhang, S.-C.; Jia, J.-f. *Nat. Mater.* **2015**, *14*, 1020–1025.
- [36] Ruppert, C.; Aslan, O. B.; Heinz, T. F. *Nano Letters* **2014**, *14*, 6231–6236.

- [37] others,, et al. *Journal of Materials Chemistry C* **2016**, *4*, 315–322.
- [38] Nicolosi, V.; Chhowalla, M.; Kanatzidis, M. G.; Strano, M. S.; Coleman, J. N. *Science* **2013**, *340*, 1226419–1226437.
- [39] Zhang, W.-B.; Qu, Q.; Zhu, P.; Lam, C.-H. *Journal of Materials Chemistry C* **2015**, *3*, 12457–12468.
- [40] Fang, H.; Chuang, S.; Chang, T. C.; Takei, K.; Takahashi, T.; Javey, A. *Nano Letters* **2012**, *12*, 3788–3792.
- [41] Sasaki, T.; Watanabe, M. *Journal of the American Chemical Society* **1998**, *120*, 4682–4689.
- [42] Ye, F.; Lee, J.; Hu, J.; Mao, Z.; Wei, J.; Feng, P. X.-L. *Small* **2016**, *12*, 5802–5808.
- [43] Omomo, Y.; Sasaki, T.; Wang,, Watanabe, M. *Journal of the American Chemical Society* **2003**, *125*, 3568–3575.
- [44] Ma, F.; Zhou, M.; Jiao, Y.; Gao, G.; Gu, Y.; Bilic, A.; Chen, Z.; Du, A. *Scientific Reports* **2015**, *5*.
- [45] Feng, J.; Sun, X.; Wu, C.; Peng, L.; Lin, C.; Hu, S.; Yang, J.; Xie, Y. *Journal of the American Chemical Society* **2011**, *133*, 17832–17838.
- [46] Kim, T. W.; Oh, E.-J.; Jee, A.-Y.; Lim, S. T.; Park, D. H.; Lee, M.; Hyun, S.-H.; Choy, J.-H.; Hwang, S.-J. *Chemistry - A European Journal* **2009**, *15*, 10752–61.
- [47] Xu, K.; Chen, P.; Li, X.; Wu, C.; Guo, Y.; Zhao, J.; Wu, X.; Xie, Y. *Angewandte Chemie International Edition* **2013**, *52*, 10477–10481.
- [48] Kim, D. S.; Ozawa, T. C.; Fukuda, K.; Ohshima, S.; Nakai, I.; Sasaki, T. *Chemistry of Materials* **2011**, *23*, 2700–2702.

- [49] Elias, D. C.; Nair, R. R.; Mohiuddin, T. M. G.; Morozov, S. V.; Blake, P.; Hall-sall, M. P.; Ferrari, A. C.; Boukhvalov, D. W.; Katsnelson, M. I.; Geim, A. K.; Novoselov, K. S. *Science* **2009**, *323*, 610–613.
- [50] Ge, W.; Kawahara, K.; Tsuji, M.; Ago, H. *Nanoscale* **2013**, *5*, 5773–5778.
- [51] Sugimoto, W.; Iwata, H.; Yasunaga, Y.; Murakami, Y.; Takasu, Y. *Angew. Chem. Int. Ed.* **2003**, *42*, 4092–6.
- [52] Bianco, E.; Butler, S.; Jiang, S.; Restrepo, O. D.; Windl, W.; Goldberger, J. E. *ACS Nano* **2013**, *7*, 4414–4421.
- [53] Waller, M. R.; Townsend, T. K.; Zhao, J.; Sabio, E. M.; Chamousis, R. L.; Browning, N. D.; Osterloh, F. E. *Chemistry of Materials* **2012**, *24*, 698–704.
- [54] Zeng, Z.; Yin, Z.; Huang, X.; Li, H.; He, Q.; Lu, G.; Boey, F.; Zhang, H. *Angewandte Chemie International Edition* **2011**, *50*, 11093–11097.
- [55] Fukuda, K.; Akatsuka, K.; Ebina, Y.; Ma, R.; Takada, K.; Nakai, I.; Sasaki, T. *ACS Nano* **2008**, *2*, 1689–1695.
- [56] Jiang, S.; Butler, S.; Bianco, E.; Restrepo, O. D.; Windl, W.; Goldberger, J. E. *Nature Communications* **2014**, *5*.
- [57] Voiry, D.; Goswami, A.; Kappera, R.; e Silva, C. d. C. C.; Kaplan, D.; Fujita, T.; Chen, M.; Asefa, T.; Chhowalla, M. *Nature chemistry* **2015**, *7*, 45–49.
- [58] Osada, M.; Sasaki, T. *Advanced Materials* **2012**, *24*, 210–228.
- [59] Bizeto, M. A.; Shiguihara, A. L.; Constantino, V. R. L. *Journal of Materials Chemistry* **2009**, *19*, 2512–2525.

- [60] Goli, P.; Khan, J.; Wickramaratne, D.; Lake, R. K.; Balandin, A. A. *Nano Letters* **2012**, *12*, 5941–5945.
- [61] Naguib, M.; Kurtoglu, M.; Presser, V.; Lu, J.; Niu, J.; Heon, M.; Hultman, L.; Gogotsi, Y.; Barsoum, M. W. *Advanced Materials* **2011**, *23*, 4248–4253.
- [62] Lei, J.-C.; Zhang, X.; Zhou, Z. *Frontiers of Physics* **2015**, *10*, 276–286.
- [63] Wang, Q.; O'Hare, D. *Chemical Reviews* **2012**, *112*, 4124–4155.
- [64] Ida, S.; Okamoto, Y.; Matsuka, M.; Hagiwara, H.; Ishihara, T. *J. Am. Chem. Soc.* **2012**, *134*, 15773–15782.
- [65] Chenet, D. A.; Aslan, O. B.; Huang, P. Y.; Fan, C.; van der Zande, A. M.; Heinz, T. F.; Hone, J. C. *Nano letters* **2015**, *15*, 5667–5672.
- [66] others,, et al. *Advanced Materials* **2012**, *24*, 2320–2325.
- [67] Hernandez, Y. et al. *Nature Nanotechnology* **2008**, *3*, 563–8.
- [68] Sasaki, T.; Watanabe, M.; Hashizume, H.; Yamada, H.; Nakazawa, H. *Journal of the American Chemical Society* **1996**, *118*, 8329–8335.
- [69] Omomo, Y.; Sasaki, T.; Wang, L.; Watanabe, M. *Journal of the American Chemical Society* **2003**, *125*, 3568–75.
- [70] Kertesz, M.; Hoffmann, R. *Journal of the American Chemical Society* **1984**, *106*, 3453–3460.
- [71] Kan, M.; Wang, J. Y.; Li, X. W.; Zhang, S. H.; Li, Y. W.; Kawazoe, Y.; Sun, Q.; Jena, P. *The Journal of Physical Chemistry C* **2014**, *118*, 1515–1522.
- [72] Voiry, D.; Salehi, M.; Silva, R.; Fujita, T.; Chen, M.; Asefa, T.; Shenoy, V. B.; Eda, G.; Chhowalla, M. *Nano Letters* **2013**, *13*, 6222–6227.

-
- [73] Lacroix, C.; Mendels, P.; Mila, F. *Introduction to Frustrated Magnetism: Materials, Experiments, Theory*; Springer Science & Business Media, 2011; Vol. 164.
- [74] Balents, L. *Nature* **2010**, *464*, 199–208.
- [75] Fletcher, J. M.; Gardener, W. E.; Hooper, E. W.; Hyder, K. R.; Moore, F. H.; Woodhead, J. L. *Nature* **1963**, *199*, 1089–1090.
- [76] Kim, H.-S.; V., V. S.; Catuneanu, A.; Kee, H.-Y. *Physical Review B* **2015**, *91*, 241110.
- [77] Kitaev, A. *Annals of Physics* **2006**, *321*, 2–111.
- [78] Banerjee, A. et al. *Nature Materials* **2016**, *15*, 733–740.
- [79] Fletcher, J. M.; Gardner, W. E.; Fox, A. C.; Topping, G. *J. Chem. Soc. A* **1967**, 1038–1045.
- [80] Kim, H.-S.; Kee, H.-Y. *Physical Review B* **2016**, *93*, 155143.

2 Magnetic properties of restacked 2D spin $1/2$ honeycomb RuCl_3 nanosheets

Daniel Weber, Leslie M. Schoop, Viola Duppel, Judith M. Lippmann, Jürgen Nuss, Bettina V. Lotsch

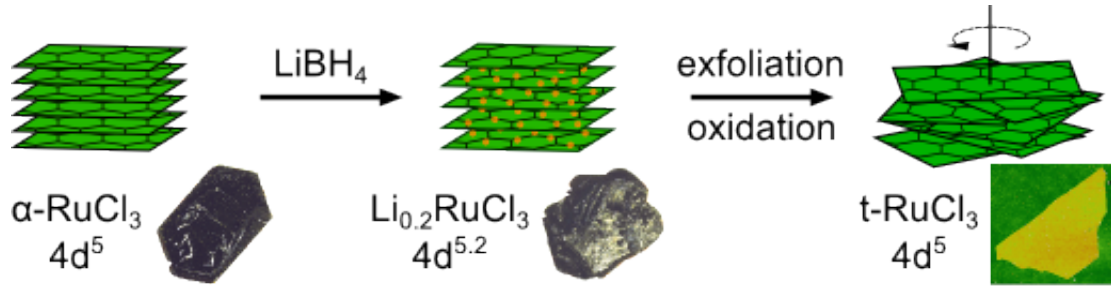
published in: *Nano Letters* **2016**, *16*, 3578-3584; DOI: 10.1021/acs.nanolett.6b00701

Reprinted (adapted) with permission from *Nano Letters*. Copyright 2016 American Chemical Society.

Abstract

Spin $\frac{1}{2}$ honeycomb materials have gained substantial interest due to their exotic magnetism and possible application in quantum computing. However, in all current materials out-of-plane interactions are interfering with the in-plane order, hence a true 2D magnetic honeycomb system is still of demand. Here, we report the exfoliation of the magnetic semiconductor $\alpha\text{-RuCl}_3$ into the first halide monolayers and the magnetic characterization of the spin $\frac{1}{2}$ honeycomb arrangement of turbostratically stacked RuCl_3 monolayers. The exfoliation is based on a reductive lithiation/hydration approach, which gives rise to a loss of cooperative magnetism due to the disruption of the spin $\frac{1}{2}$ state by electron injection into the layers. The restacked, macroscopic pellets of RuCl_3 layers lack symmetry along the stacking direction. After an oxidative treatment, cooperative magnetism similar to

the bulk is restored. The oxidized pellets of restacked single layers feature a magnetic transition at $T_N = 7$ K if the field is aligned parallel to the ab -plane, while the magnetic properties differ from bulk $\alpha\text{-RuCl}_3$ if the field is aligned perpendicular to the ab -plane. The deliberate introduction of turbostratic disorder to manipulate the magnetic properties of RuCl_3 is of interest for research in frustrated magnetism and complex magnetic order as predicted by the Kitaev-Heisenberg model.



2.1 Introduction

The emergence of graphene^{1,2} initiated the development of a variety of single layer compounds as well as investigations into their electronic, optical and mechanical properties. The materials that are most actively examined are monolayers either composed of a single element, such as carbon based graphene or black phosphorus single layers, or binary transition metal chalcogenides.³⁻⁶ Binary halide nanosheets have been predicted based on chemical intuition^{3,4} or *ab initio* calculations.⁷ Yet, no single layer halides have been synthesized so far, even though this class of compounds features an array of interesting electrical and magnetic properties.

The magnetic semiconductor α -RuCl₃ is one such example. While it was investigated in the past as a host for intercalants^{8,9} and as a lithium ion conductor¹⁰, current research focuses on its magnetic properties. These are determined by the nearly perfect honeycomb lattice of $4d^5$ Ru³⁺ centers with $S = \frac{1}{2}$ due to the intermediate spin-orbit coupling (SOC) of ruthenium.^{11,12} For these reasons, α -RuCl₃ is currently debated as a candidate for the Kitaev-Heisenberg model. Within this model, spin $\frac{1}{2}$ centers are arranged on a honeycomb lattice with competing exchange interactions up to the third neighbor, leading to a variety of exotic spin phases.¹³ The model suggests that the system could possibly be pushed into a quantum spin liquid regime by the manipulation of the competing interactions, thereby opening up applications in quantum computing.¹⁴

The first candidate material for showing physics predicted by the Kitaev-Heisenberg model was Na₂IrO₃,^{15,16} which features a zigzag antiferromagnetic (AF) order as its ground state.¹⁷⁻¹⁹ In this type of spin order, the magnetic moments form ferromagnetic (FM) zigzag chains, whose magnetization direction is opposed to the neighboring chains within the plane. Yet, the Na⁺ ions in the interlayer space of Na₂IrO₃ lead to disadvantageous interactions between the iridate layers, which interfere with theoretical predictions of a

honeycomb arrangement of spin $\frac{1}{2}$ magnetic arrays.²⁰ Eliminating the interlayer interaction could provide a route to manipulate the spin structure of real materials featuring a spin $\frac{1}{2}$ honeycomb arrangement.

In RuCl_3 , where no charged ions are in between the honeycomb layers, the interlayer interactions are smaller than in Na_2IrO_3 , but are not negligible.²¹ RuCl_3 was shown to feature two magnetic transitions at 7-8 K and 14 K; below 8 K the system was shown to enter a zigzag magnetic ground state similar to Na_2IrO_3 , but the spins are modulated over a three layer periodicity and tilted 35° out of the RuCl_3 plane.²² The presence of ABAB stacking faults in the ABC ordered layers of RuCl_3 disrupts the layer periodicity, causing the appearance of several additional magnetic transitions above $T_N = 8$ K,²² including the one at 14 K.²³⁻²⁵ This observation indicates the importance of the stacking sequence, but also of the interlayer interactions for the magnetic properties in this material. While one possibility for investigating the influence of stacking faults on the magnetism of RuCl_3 is the growth of perfect single crystals to eliminate stacking faults,²² another one is to introduce completely random stacking.

There are two options to structurally alter and possibly decouple the magnetic interactions between two layers. The first is to increase the interlayer space by introducing a non-magnetic compound. This approach has been realized in $\text{Na}_3\text{Ni}_2\text{SbO}_6$ and $\text{Na}_3\text{Ni}_2\text{BiO}_{6-\delta}$, where hydration of the interlayer Na^+ ions increases the interlayer distance by about one Ångstrom. This increase in distance caused a more 2D like magnetic behavior in the compound.^{26,27} Another example is the CrCl_3 -graphite intercalation compound $\text{C}_{20.9}\text{CrCl}_3$, where the intercalation of CrCl_3 single layers into graphite resulted in the emergence of spin glass behavior.²⁸ Exfoliation of 2D honeycomb compounds into monolayers and restacking the layers to form a solid with turbostratic disorder is the second strategy to reduce interlayer coupling. This kind of disorder can be described by random rotations and/or translations of the sheets around an axis perpendicular to the monolayer. Recently, it was

shown that the stacking angle of two MoS₂ monolayers has a strong effect on the electronic interlayer coupling.²⁹ Thus, the restacking of single layers into a turbostratically disordered solid should significantly alter the magnetic properties of a layered compound.

Here, we present a form of RuCl₃ with turbostratic disorder (t-RuCl₃) introduced by exfoliation into single layers and subsequent restacking into a lamellar, disordered solid. To the best of our knowledge, this is the first report of a single layer halide as well as of a single layer compound with a $S = \frac{1}{2}$ honeycomb order. Furthermore, we show the disappearance of cooperative magnetism in the intermediary compound Li_{0.2}RuCl₃ and in the restacked pellet of the partially reduced [RuCl₃]^{x-} single layers. By an oxidative reaction step, a multisheet stack of [RuCl₃]^{x-} is converted to t-RuCl₃, which features a magnetic transition at $T_N = 7$ K as well as highly anisotropic magnetism. The similarities and differences of the magnetic properties between bulk α -RuCl₃ and restacked t-RuCl₃ will be discussed in regards to the changes of the electronic and crystal structure.

2.2 Results and Discussion

2.2.1 Preparative procedure and general observations

For the synthesis of t-RuCl_3 , large single crystals of $\alpha\text{-RuCl}_3$ were prepared by chemical vapor transport from 1023 K to 973 K. X-ray diffraction on a single crystal confirmed the recently reported monoclinic space group $C2/m$ ¹² (SG, no. 12), in which the $\alpha\text{-RuCl}_3$ layers consist of edge sharing RuCl_6 octahedra and are separated by a van der Waals gap. Every third octahedron is vacant, resulting in a honeycomb lattice of Ru^{3+} centers. The crystal structure is shown in Figure 2.1 d) and e). The crystals were treated with LiBH_4 in THF under inert atmosphere to yield $\text{Li}_{0.2}\text{RuCl}_3$ according to a modified literature procedure.¹⁰ Energy dispersive X-ray (EDX) and atomic emission spectroscopy (AES) confirmed the composition of $\text{Li}_{0.2}\text{RuCl}_3$. In contact with H_2O , $\text{Li}_{0.2}\text{RuCl}_3$ spontaneously starts to exfoliate into $[\text{RuCl}_3]^{x-}$ single layers. After shaking for 24 h, the black suspension was centrifuged to separate unreacted crystallites and larger agglomerates from the liquid. The dispersion was further washed three times by centrifugation and replacement of the supernatant liquid with water. The nanosheets form a stable suspension in water as indicated by the zeta potential of -51.4 mV. $[\text{RuCl}_3]^{x-}$ nanosheets were both characterized as monolayers on 270 nm SiO_2/Si substrates by optical and atomic force microscopy (AFM) and on lacey carbon grids by transmission electron microscopy (TEM). Pellets of $[\text{RuCl}_3]^{x-}$ nanosheets were prepared by evaporation of the solvent and were characterized by powder X-ray diffraction (PXRD). Monolayers on substrates and pellets of $[\text{RuCl}_3]^{x-}$ were oxidized in an atmosphere of Br_2 over night to yield t-RuCl_3 , which was characterized by AFM and PXRD. All compounds were examined by EDX, confirming the Ru : Cl ratio of 1 : 3.

Figures 2.1 a) to e) show the images of $\alpha\text{-RuCl}_3$ crystals, the intermediate product $\text{Li}_{0.2}\text{RuCl}_3$ and an aqueous $[\text{RuCl}_3]^{x-}$ dispersion as well as the crystal structure of $\alpha\text{-RuCl}_3$.

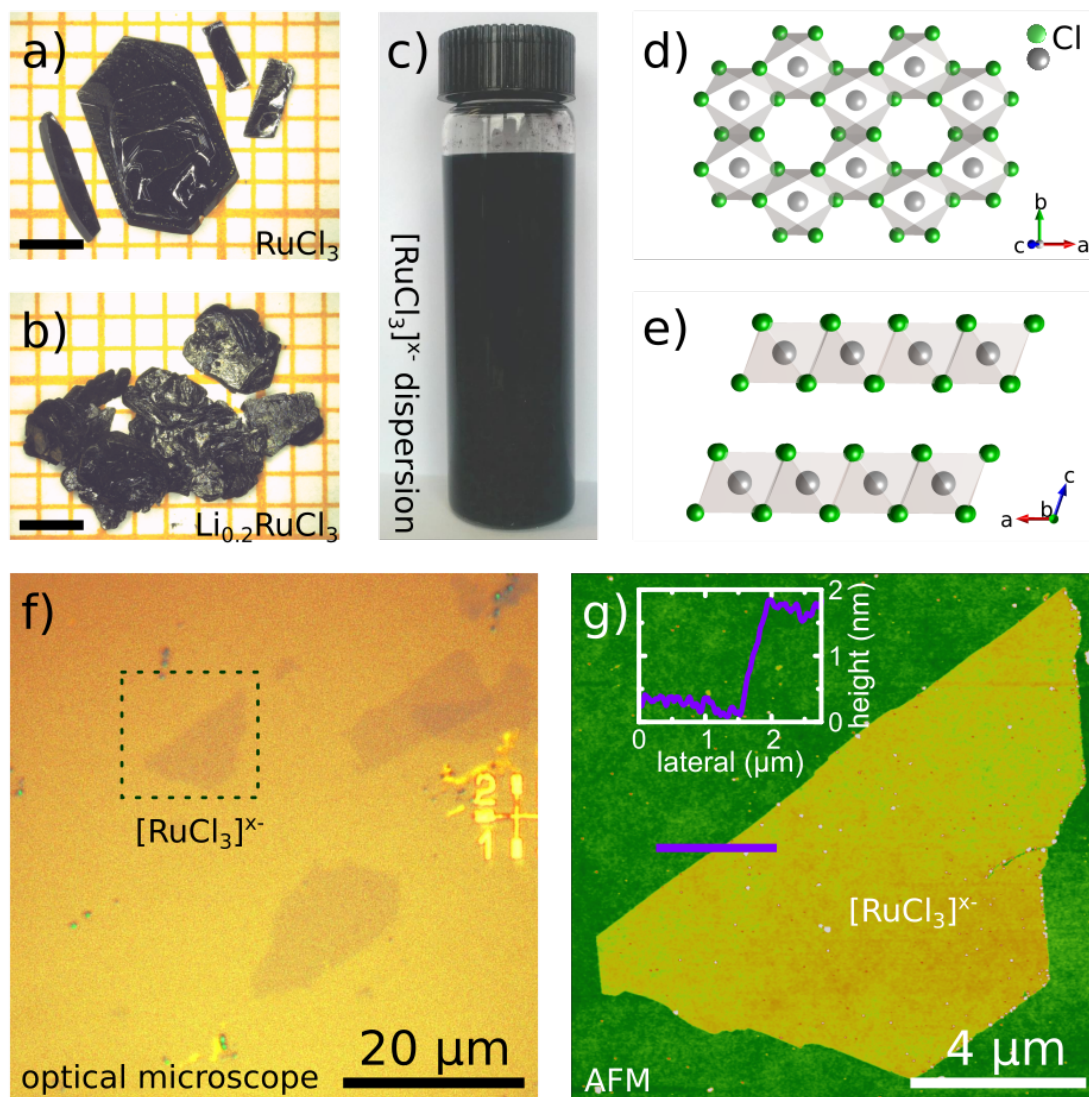


Figure 2.1: a) α - RuCl_3 crystals, scale bar 2 mm, b) $\text{Li}_{0.2}\text{RuCl}_3$ platelets, scale bar 2 mm, c) $[\text{RuCl}_3]^{x-}$ nanosheet in aqueous dispersion, d) honeycomb structure of α - RuCl_3 viewed along $[001]$, e) layered structure of α - RuCl_3 viewed along $[010]$, f) $[\text{RuCl}_3]^{x-}$ single layer on 270 nm SiO_2/Si substrate, imaged by optical microscopy, g) AFM image of highlighted $[\text{RuCl}_3]^{x-}$ monolayer from optical image with 1.69(9) nm height.

As seen in Figure 2.1 f), monolayers of $[\text{RuCl}_3]^{x-}$ were located by the enhanced interference contrast on the SiO_2/Si substrate, a method known from investigations on graphene and MoS_2 .^{30,31} Different batches of $[\text{RuCl}_3]^{x-}$ dispersions were analyzed to ensure reproducibility; some more examples are displayed in Figure A.1 and A.2. The single layers covered areas of up to $450 \mu\text{m}^2$ and thus their areas are of the same order of magnitude as the largest chemically exfoliated MoS_2 monolayers known to date.³²

2.2.2 Structural characterization

The height of the $[\text{RuCl}_3]^{x-}$ single layers was analyzed by AFM for the monolayer on the SiO_2/Si substrate and by PXRD for the restacked pellet. Figure 2.1 g) shows one exemplary AFM image with a height of $1.69(9) \text{ nm}$ for a $[\text{RuCl}_3]^{x-}$ monolayer. It is a common phenomenon that the monolayer height on the substrate differs from the nanosheet terrace height on top of another nanosheet due to the difference in chemical potential.³³ The height of a $[\text{RuCl}_3]^{x-}$ single layer folded onto itself was determined to be $1.06(6) \text{ nm}$, as verified by additional exemplary images in Figure A.1 and A.2 in the supporting information. This value is similar to that of chemically exfoliated MoS_2 , where the single layer has a height of $1.0 - 1.2 \text{ nm}$,³⁴ but still deviates from the height of a single crystalline slab due to a water layer adsorbed on the substrate and nanosheets. Out-of-plane PXRD measurements of the $[\text{RuCl}_3]^{x-}$ pellet (fig. 2.2 a) in reflection geometry yielded a height of $d_{(001)} = 1.12 \text{ nm}$, confirming the results from AFM indicating the presence of a water layer between the RuCl_3 slabs.⁸ The small height difference between AFM and PXRD data might originate from variations in relative humidity, which recently were shown to have a large influence on the layer height of phosphatoantimonic acid $\text{H}_3\text{Sb}_3\text{P}_2\text{O}_{14}$ nanosheets.³⁵

Though the height of a single layer from PXRD and AFM are in agreement, there is still a discrepancy compared to the height of a single layer of the $\alpha\text{-RuCl}_3$ crystal structure

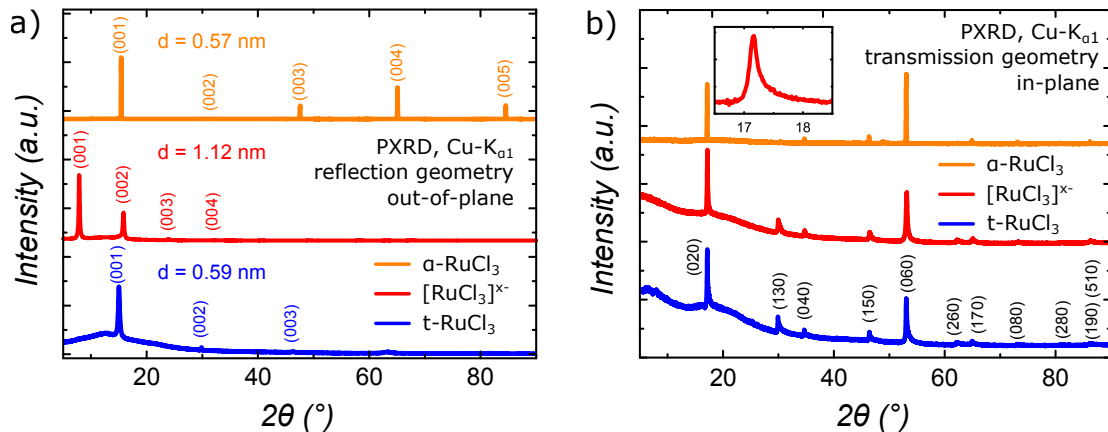


Figure 2.2: a) In-plane PXRD of α -RuCl₃ single crystals, [RuCl₃]^{x-} and t-RuCl₃ nanosheet pellets measured in reflection geometry, b) in-plane PXRD of α -RuCl₃ single crystals, [RuCl₃]^{x-} and t-RuCl₃ nanosheet pellets measured in transmission geometry, inset features the (020) peak of [RuCl₃]^{x-} with a Warren-type shape due to turbostratic disorder.

(0.57 nm). This is most likely due to the presence of residual charge on a single [RuCl₃]^{x-} layer, which is indicated by the high zeta potential of - 51.4 mV of the [RuCl₃]^{x-} dispersion. The negative surface charge is compensated by hydrated protons, thus increasing the layer height. After the reductive intercalation, the ratio of Ru : Cl = 1 : 3 remains unchanged according to EDX. Therefore, we assume that the charge injected by LiBH₄ resides in the *d*-bands of Ru, leading to a $4d^{5+x}$ state of Ru^{(3-x)+} in [RuCl₃]^{x-}.

2.2.3 Effect of oxidation

The [RuCl₃]^{x-} monolayers and pellets were oxidized in a Br₂ atmosphere to remove the residual layer charge and thus the protons and their hydrate shell, leading to t-RuCl₃. The single layer height measured on the substrate by AFM shrank from 1.69(9) nm to 1.08(17) nm, which is higher than the slab in the crystal due to the change in chemical potential between substrate and sample measured by AFM. The height of a single layer folded onto itself decreased from 1.06(6) nm to 0.72(11) nm, which is very close to the expected height of a monolayer. Example images of RuCl₃ monolayers are shown in Figure

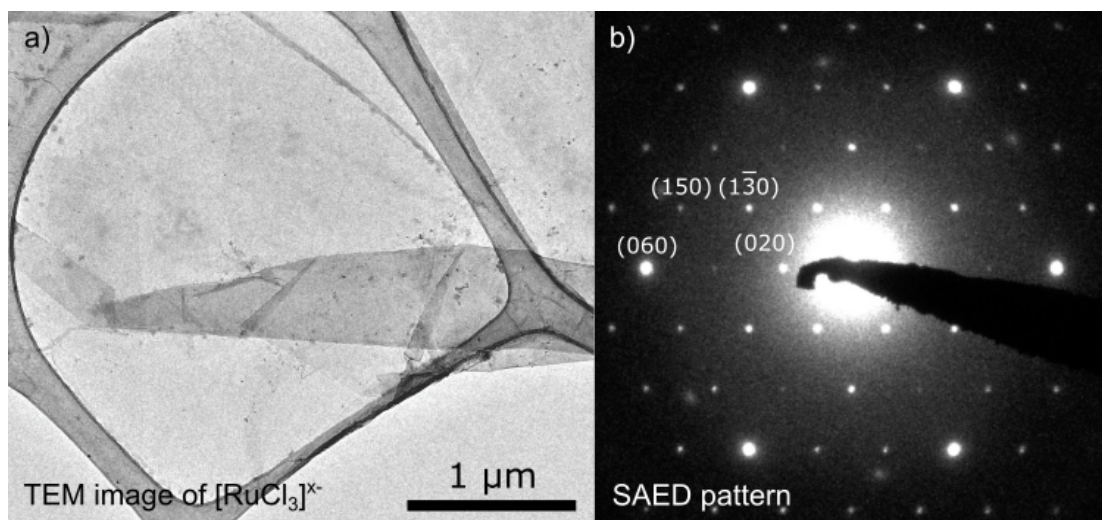


Figure 2.3: a) TEM bright field image of partially folded $[\text{RuCl}_3]^{x-}$ on lacey carbon grid, b) SAED pattern of $[\text{RuCl}_3]^{x-}$, viewed along the $[001]$ zone axis.

A.3. According to PXRD measurements, the restacked layers in the pellet feature a similar decrease of the stacking distance from 1.12 nm before to 0.59 nm after oxidation, which is close to the layer height of 0.57 nm in bulk $\alpha\text{-RuCl}_3$ as seen in Figure 2.2 a). Again, the AFM and PXRD data are in good agreement with a slightly higher value from AFM, possibly due to surface roughness. Hence the present counterions in $[\text{RuCl}_3]^{x-}$ were expelled by the oxidative treatment with Br_2 to yield the oxidized nanosheets and HBr .

Since the exfoliation process induces physical stress and bromine's high oxidative power could potentially damage the sample, the integrity of the in-plane crystal structure was investigated by TEM on the $[\text{RuCl}_3]^{x-}$ single layer as well as PXRD on a multilayer stack of $[\text{RuCl}_3]^{x-}$ and t-RuCl_3 . Figure 2.3 a) displays a TEM bright field image of a single $[\text{RuCl}_3]^{x-}$ layer partially folded onto itself on a lacey carbon grid. Figure 2.3 b) features the in-plane $(hk0)$ reflections from selected area electron diffraction (SAED). The reflections were assigned by simulating the diffraction pattern based on the space group $C2/m$ of bulk $\alpha\text{-RuCl}_3$. Figure A.4 shows the simulated diffraction pattern. The d -values of the first five most intense reflections, as listed in Table A.4, coincide with the d -values from the

simulation based on the single crystal data within the margin of error in TEM. Therefore, we conclude that the in-plane structure is maintained in the exfoliation process.

Additionally, PXRD was performed on the pellet of restacked $[\text{RuCl}_3]^{\text{x-}}$ layers and t-RuCl₃ in transmission geometry, to check the effect of the Br₂ treatment on the in-plane structure. The resulting diffraction patterns are shown in Figure 2.2 c) and consist of the $(hk0)$ reflections with an intensity tail towards higher angles. The peak positions and d -values coincide with those of the $(hk0)$ reflections of single crystal α -RuCl₃ (Tab. A.4), indicating the retention of the in-plane structure in the $[\text{RuCl}_3]^{\text{x-}}$ pellet, as well as in t-RuCl₃.

The diffraction patterns also offer information about the ordering of the layers in the multistack. A noticeable feature is the Warren-type peak shape tailing off towards higher angles. The anisotropic form originates from the diffraction of the X-ray beam by a lattice with two dimensional translation symmetry without any ordering in the third dimension,^{36–38} signifying turbostratic disorder. A similar conclusion can be drawn from the out-of-plane PXRD, where the pellets of $[\text{RuCl}_3]^{\text{x-}}$ and t-RuCl₃ feature an exponential intensity decay for the series of $(00l)$ reflections with higher order. This is known from tetrabutylammonium (TBA) intercalated, swollen lamellar phases such as TBA_{0.35}Ti_{0.91}O₂, TBA_{0.13}MnO₂ and TBA_{0.2}RuO_{2.1}.^{39–41} The $(00l)$ reflections of the ordered bulk α -RuCl₃ features a different intensity distribution, which is displayed in Figure 2.2 a). Therefore, the presence of turbostratic disorder is confirmed by the in- and out-of-plane PXRD patterns.

2.2.4 Investigations on the magnetism

Next, we investigate the effect of turbostratic disorder on the magnetic properties depending on the in-plane (ip) and out-of-plane (op) direction for the compounds α -RuCl₃ and Li_{0.2}RuCl₃ as well as for the pellets of $[\text{RuCl}_3]^{\text{x-}}$ and t-RuCl₃. The presence of magnetic

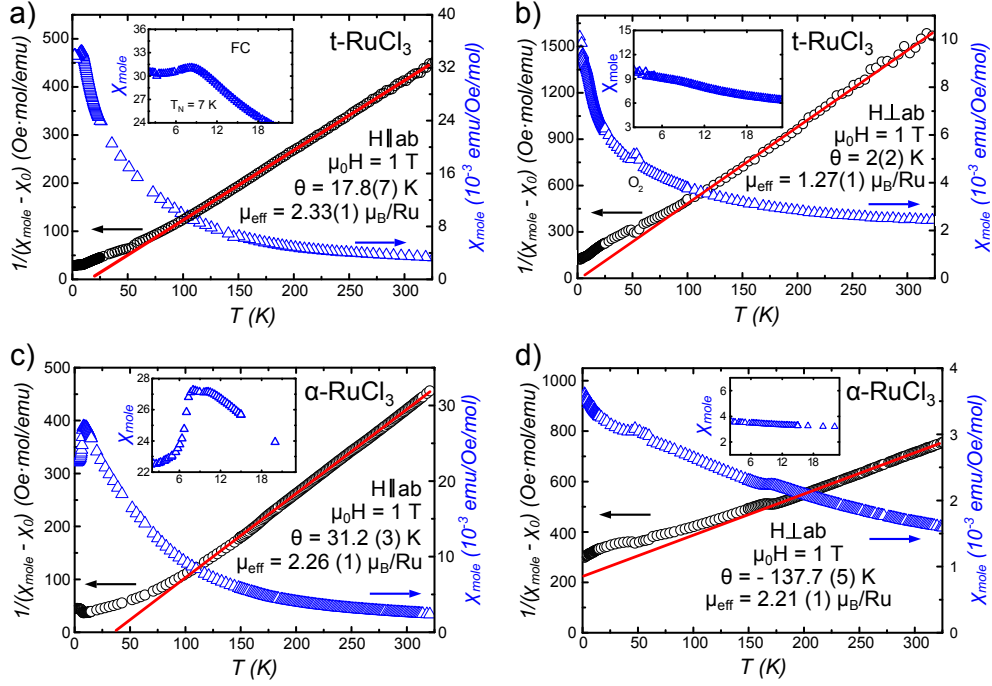


Figure 2.4: a) In-plane susceptibility (blue) and inverse susceptibility (black) of t-RuCl_3 nanosheet pellet vs temperature at a field of $\mu_0 H = 1$ T, Curie-Weiss fit as red line, inset shows susceptibility from $T = 2$ K to 23 K with broad peak at $T_N = 7$ K, b) out-of-plane data for the same samples measured in a field of $\mu_0 H = 1$ T, inset displays relevant region with no visible peaks in the same scale as a), c) in-plane susceptibility (blue) and inverse susceptibility (black) of $\alpha\text{-RuCl}_3$ crystal vs temperature at a field of $\mu_0 H = 1$ T, Curie-Weiss fit as red line, inset shows susceptibility from $T = 2$ K to 23 K with magnetic transitions at $T_{N1} = 7$ K and $T_{N2} = 13$ K, d) out-of-plane data for the same $\alpha\text{-RuCl}_3$ crystal measured in a field of $\mu_0 H = 1$ T, inset displays relevant region between 2 and 23 K.

transitions, the Weiss temperature and the magnetic moment were used as a measure for the cooperative character of the magnetic properties. The magnetic susceptibilities of t-RuCl_3 and $\alpha\text{-RuCl}_3$ are presented in Figure 2.4, while the data for $\text{Li}_{0.2}\text{RuCl}_3$ and $[\text{RuCl}_3]^x$ is shown in the supporting information. Figure 2.5 summarizes the results of Curie-Weiss fits for all compounds.

In bulk $\alpha\text{-RuCl}_3$, we observe two magnetic transitions at $T_{N1} = 7$ K and $T_{N2} = 13$ K for the in-plane measurements, which were determined from the dMT/dT plot displayed in the supporting information. Recent investigations assigned $T_{N1} = 7$ K to an ABC stacking

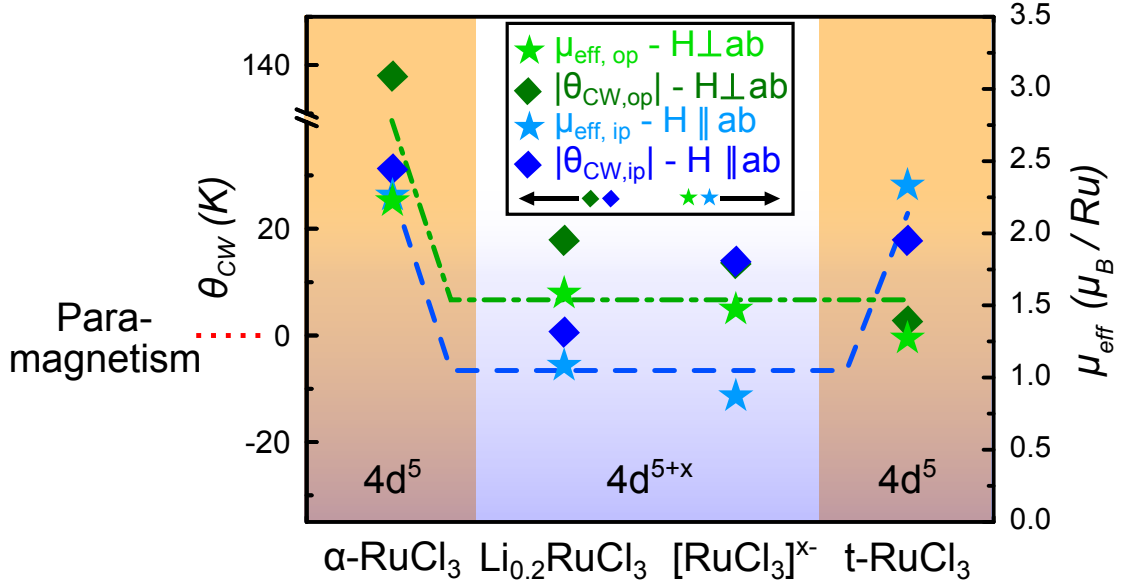


Figure 2.5: Evolution of the Weiss temperature θ_{CW} and effective magnetic moment μ_{eff} in-plane (blue) and out-of-plane (green) for α -RuCl₃, Li_{0.2}RuCl₃, [RuCl₃]^{x-}, and t-RuCl₃. The dashed lines indicate the general trend between cooperative and non cooperative magnetism, which depends on the electronic state. θ_{CW} values were plotted as absolute values to ease comparability.

order, while the transition at $T_{N2} = 13$ K is induced by the presence of AB stacking faults.^{12,22} The Weiss temperatures $\theta_{CW,ip}$ of 31.2(3) K and $\theta_{CW,op}$ of - 137.7(5) K suggest an in-plane FM exchange and out-of-plane AF interactions. These results are comparable to previous studies, where the values range from $\theta_{CW,ip} = 37$ K to 68 K and $\theta_{CW,op} = -145$ K to - 150 K.^{23,25} The effective magnetic moment $\mu_{eff,ip} = 2.26(1) \mu_B / \text{Ru}$ and $\mu_{eff,op} = 2.22(1) \mu_B / \text{Ru}$ are also in the range of previously reported values ($\mu_{eff,ip} = 2.0 - 2.14 \mu_B / \text{Ru}$ and $\mu_{eff,op} = 2.3 - 2.7 \mu_B / \text{Ru}$) and are much higher than the spin-only value of $1.75 \mu_B / \text{Ru}$, thereby indicating the presence of SOC.^{23,24}

Upon the reductive intercalation of lithium ions into the interlayer space, the 4d⁵ electron configuration of Ru³⁺ changes to a 4d⁶ state with $S = 0$ for roughly 20 % of the Ru centers in Li_{0.2}RuCl₃. This is abbreviated as "4d^{5.2}" in Figure 2.5. The disturbance of the spin $\frac{1}{2}$ order leads to paramagnetic behavior, which is associated with a decay-

ing magnetic susceptibility with increasing temperature without any magnetic transition in the in- and out-of-plane direction. The decrease of the in-plane ($\theta_{CW,ip} = 0.6(2)$ K, $\mu_{eff,ip} = 1.08(2)$ μ_B / Ru) as well as out-of-plane Weiss temperatures and magnetic moments ($\theta_{CW,op} = 17.8(3)$ K, $\mu_{eff,op} = 1.58(1)$ μ_B / Ru) also reflects this trend. This suggest that the cooperative magnetism of $\alpha\text{-RuCl}_3$ has been disturbed by electron injection into the RuCl_3 -layers. Recently, a similar change in magnetism has been reported in Na_2IrO_3 , where holes were injected into the $[\text{Na}_{1/3}\text{Ir}_{2/3}\text{O}_2]^{\frac{2}{3}-}$ layer by oxidation with Br_2 . There, the low spin electron configuration changes from $5d^5$ to $5d^4$ with $S = 0$ due to SOC, inducing paramagnetic behavior.⁴²

The magnetic data of the restacked pellet of $[\text{RuCl}_3]^x$ measured within the plane exhibits a similarly decaying magnetization curve without any features, similar to the paramagnetic behavior of $\text{Li}_{0.2}\text{RuCl}_3$. Although the Weiss temperatures indicate slightly antiferromagnetic behavior ($\theta_{CW,ip} = -13.5(7)$ K and $\theta_{CW,op} = -13.5(3)$ K), no magnetic ordering transitions were observed in the out-of-plane direction and only a slight shoulder is visible in the in-plane direction. The effective magnetic moment is very similar to that of $\text{Li}_{0.2}\text{RuCl}_3$ with values of $\mu_{eff,ip} = 0.87(1)$ μ_B / Ru and $\mu_{eff,op} = 1.47(1)$ μ_B / Ru.

Upon oxidation of the $[\text{RuCl}_3]^x$ pellet by Br_2 to t-RuCl_3 and the associated restoration of the $4d^5$ state, the ordered magnetism within the plane returns. This is reflected by a transition in the in-plane data of the magnetic susceptibility at $T_N = 7$ K. The transition is rather broad, similar to previous observations in more 2D-like magnetic materials.²⁶ The same behavior was observed in the heat capacity, as shown in Figure A.14, featuring a broad peak, which is again typical for 2D-like magnetic compounds with stacking disorder.^{26,43} The appearance of this peak strongly suggests the restoration of the Ru^{3+} oxidation state. Also, it is accompanied by an increase of the Weiss temperature as well as the effective magnetic moment to $\theta_{CW,ip} = 17.8(7)$ K and $\mu_{eff,ip} = 2.33(1)$ μ_B / Ru respectively, values similar to those found in the in-plane data of $\alpha\text{-RuCl}_3$ ($\theta_{CW,ip} = 31.2(3)$ K;

$\mu_{eff,ip} = 2.26(1) \mu_B / \text{Ru}$). In contrast, if the field is applied perpendicular to the *ab*-plane no transitions are observed and the magnetic susceptibility monotonically declines towards higher temperatures. The out-of-plane Weiss temperature $\theta_{CW,op} = 2(2) \text{ K}$ indicates paramagnetic behavior, similar to the low effective magnetic moment $\mu_{eff,op} = 1.27(1) \mu_B / \text{Ru}$, which is much closer to the value found in the paramagnetic $\text{Li}_{0.2}\text{RuCl}_3$ ($\mu_{eff,op} = 1.58(1) \mu_B / \text{Ru}$) than the one found in $\alpha\text{-RuCl}_3$ ($\mu_{eff,op} = 2.22(1) \mu_B / \text{Ru}$). The values of the out-of-plane Weiss temperature and effective magnetic moment are in strong contrast to the bulk values and suggests an increase in the magnetic anisotropy when compared to the values along the in-plane direction.

As seen from the data on the prepared compounds, our procedure presented in 2.6 leads to varying magnetic behavior due to manipulation of the ruthenium electron configuration and the stacking structure. Cooperative magnetism is disrupted by electron injection in $\text{Li}_{0.2}\text{RuCl}_3$ and $[\text{RuCl}_3]^\times$. The data of *t*- RuCl_3 measured with the field aligned parallel to the *ab*-plane features a magnetic transition at $T_N = 7 \text{ K}$, which suggests a restoration of the magnetic order based on the $4d^5$ electron configuration of Ru^{3+} . In $\alpha\text{-RuCl}_3$ a transition at this temperature is linked to ABC order.²² A similar order seems highly unlikely for *t*- RuCl_3 given that the pellet was deposited at 60°C out of a solution that in the vast majority consists of single layers (see Figure A.1 and A.2). While we cannot fully exclude the possibility that the system spontaneously adopts an ordered ABC stacking sequence upon re-stacking, this scenario appears very unlikely given the minute energy differences between the different stacking sequences vs. rotational and translational disorder. Based on the PXRd data, the formation of a locally ordered minority phase upon restacking unlikely exceeds 5-10 %. Measurement on the local level, i.e. on single layers, are therefore of great interest for future investigations.

As observed to a lesser extent for $\alpha\text{-RuCl}_3$, the Curie-Weiss temperature and the magnetic moments in *t*- RuCl_3 are highly anisotropic, which is contrary to the KH-model where

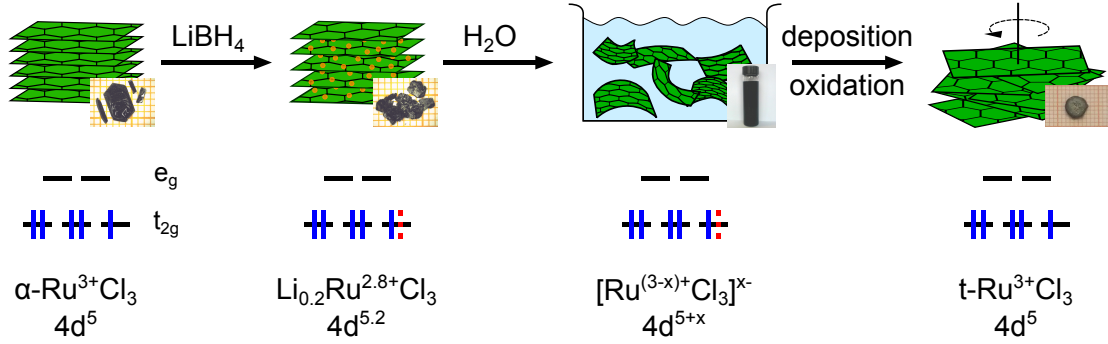


Figure 2.6: Schematic summary of the presented phases, the chemical steps necessary to obtain them and illustrations to explain the differences in the stacking. Simplified molecular orbitals for a monomeric $[\text{RuCl}_6]^{3-}$ complex constituting a RuCl_3 layer visualize the differences in the electronic state and in combination with the stacking, help to explain the evolution of the spin order.

all magnetic exchange interactions are isotropic in regard to the real space xyz coordinate system.^{44,45} This anisotropy likely results from a complex interplay between all exchange interactions in the material, including structural deviations from the ideal honeycomb lattice, different degrees of interlayer interactions, and the zigzag magnetic ground state. The enhanced asymmetry in the magnetic behavior of t-RuCl_3 could suggest that the honeycomb distorts upon exfoliation; we could however find no indications of that in our diffraction data.

Even though the exact spin structure of t-RuCl_3 is yet unknown, the combination of the $4d^5$ electron configuration, the retention of the Ru honeycomb arrangement as well as the magnetic transition at the same temperature as the zigzag order in bulk $\alpha\text{-RuCl}_3$ hint towards the restoration of the magnetic order in t-RuCl_3 , with the zigzag structure being one possible candidate.

2.3 Conclusion

In conclusion, we presented a synthetic route towards large area RuCl_3 nanosheets, the first exfoliation of a binary halide. Investigations of its in-plane crystal structure show that it was retained during the exfoliation process, leading to dispersed, charged $[\text{RuCl}_3]^{x-}$ monolayers in suspension. Deposition of the sheets is possible and is used to create a pellet with turbostratic disorder. Magnetic measurements show that the intermediary pellet is a paramagnet. Upon oxidizing the pellet, the long range magnetic order of the spin $\frac{1}{2}$ honeycomb arrangement is reestablished. A very different Weiss temperature and effective magnetic moment were observed in the out-of-plane direction compared to bulk $\alpha\text{-RuCl}_3$, probably due to turbostratic disorder.

We introduce here the first single layer spin $\frac{1}{2}$ honeycomb material, realized in RuCl_3 monolayers. Therefore, magnetic measurements on large single layers of $\alpha\text{-RuCl}_3$ that can be deposited on any substrate are feasible in the future. To our knowledge, a top-down approach of exfoliation and restacking of nanosheets to deliberately introduce turbostratic disorder enabling the manipulation of the magnetic properties of a solid has not been reported yet. We believe that the approach presented herein provides a synthetic tool to establish macroscopic quasi 2D model systems for Kitaev-Heisenberg physics in spin $\frac{1}{2}$ honeycomb magnets and areas beyond.

References

- [1] Novoselov, K. S.; Geim, A. K.; Morozov, S. V.; Jiang, D.; Zhang, Y.; Dubonos, S. V.; Grigorieva, I. V.; Firsov, A. A. *Science* **2004**, *306*, 666–669.
- [2] Novoselov, K. S.; Geim, A. K.; Morozov, S. V.; Jiang, D.; Katsnelson, M. I.; Grig-

- orieva, I. V.; Dubonos, S. V.; Firsov, A. A. *Nature* **2005**, *438*, 197–200.
- [3] Nicolosi, V.; Chhowalla, M.; Kanatzidis, M. G.; Strano, M. S.; Coleman, J. N. *Science* **2013**, *340*, 1226419–1226437.
- [4] Miró, P.; Audiffred, M.; Heine, T. *Chem. Soc. Rev.* **2014**, *43*, 6537.
- [5] Xia, F.; Wang, H.; Xiao, D.; Dubey, M.; Ramasubramaniam, A. *Nature Photonics* **2014**, *8*, 899–907.
- [6] Fiori, G.; Bonaccorso, F.; Iannaccone, G.; Palacios, T.; Neumaier, D.; Seabaugh, A.; Banerjee, S. K.; Colombo, L. *Nat. Nanotechnol.* **2014**, *9*, 768–779.
- [7] Zhang, W.-B.; Qu, Q.; Zhu, P.; Lam, C.-H. *Journal of Materials Chemistry C* **2015**, *3*, 12457–12468.
- [8] Schöllhorn, R.; Steffen, R.; Wagner, K. *Angewandte Chemie International Edition in English* **1983**, *22*, 555–556.
- [9] Steffen, R. *Solid State Ionics* **1986**, *22*, 31–41.
- [10] Wang, L.; Rocci-Lane, M.; Brazis, P.; Kannewurf, C. R.; Kim, Y.-I.; Lee, W.; Choy, J.-H.; Kanatzidis, M. G. *J. Am. Chem. Soc.* **2000**, *122*, 6629–6640.
- [11] Plumb, K. W.; Clancy, J. P.; Sandilands, L. J.; Shankar, V. V.; Hu, Y. F.; Burch, K. S.; Kee, H.-Y.; Kim, Y.-J. *Physical Review B* 041112.
- [12] Johnson, R. D.; Williams, S. C.; Haghighirad, A. A.; Singleton, J.; Zapf, V.; Manuel, P.; Mazin, I. I.; Li, Y.; Jeschke, H. O.; Valentí, R.; Coldea, R. *Phys. Rev. B* **2015**, *92*, 235119.
- [13] Kitaev, A. *Annals of Physics* **2006**, *321*, 2–111.

-
- [14] Nayak, C.; Simon, S. H.; Stern, A.; Freedman, M.; Das Sarma, S. *Rev. Mod. Phys.* **2008**, *80*, 1083–1159.
- [15] Chaloupka, J.; Jackeli, G.; Khaliullin, G. *Phys. Rev. Lett.* **2010**, *105*, 027204.
- [16] Chaloupka, J.; Jackeli, G.; Khaliullin, G. *Phys. Rev. Lett.* **2013**, *110*, 097204.
- [17] Liu, X.; Berlijn, T.; Yin, W.-G.; Ku, W.; Tsvelik, A.; Kim, Y.-J.; Gretarsson, H.; Singh, Y.; Gegenwart, P.; Hill, J. P. *Physical Review B* 220403.
- [18] Choi, S. K.; Coldea, R.; Kolmogorov, A. N.; Lancaster, T.; Mazin, I. I.; Blundell, S. J.; Radaelli, P. G.; Singh, Y.; Gegenwart, P.; Choi, K. R.; Cheong, S.-W.; Baker, P. J.; Stock, C.; Taylor, J. *Phys. Rev. Lett.* **2012**, *108*, 127204.
- [19] Ye, F.; Chi, S.; Cao, H.; Chakoumakos, B. C.; Fernandez-Baca, J. A.; Custelcean, R.; Qi, T. F.; Korneta, O. B.; Cao, G. *Phys. Rev. B* **2012**, *85*, 180403.
- [20] Kim, H.-S.; V., V. S.; Catuneanu, A.; Kee, H.-Y. *Physical Review B* **2015**, *91*, 241110.
- [21] Kim, H.-S.; Kee, H.-Y. *Physical Review B* **2016**, *93*, 155143.
- [22] Cao, H. B.; Banerjee, A.; Yan, J.-Q.; Bridges, C. A.; Lumsden, M. D.; Mandrus, D. G.; Tennant, D. A.; Chakoumakos, B. C.; Nagler, S. E. *Physical Review B* 134423.
- [23] Sears, J. A.; Songvilay, M.; Plumb, K. W.; Clancy, J. P.; Qiu, Y.; Zhao, Y.; Parshall, D.; Kim, Y.-J. *Physical Review B* **2015**, *91*, 144420.
- [24] Majumder, M.; Schmidt, M.; Rosner, H.; Tsirlin, A. A.; Yasuoka, H.; Baenitz, M. *Physical Review B* 180401.
- [25] Kubota, Y.; Tanaka, H.; Ono, T.; Narumi, Y.; Kindo, K. *Physical Review B* **2015**, *91*, 094422.

- [26] Roudebush, J.; Cava, R. *J. Solid State Chem.* **2013**, *204*, 178–185.
- [27] Seibel, E. M.; Roudebush, J. H.; Ali, M. N.; Ross, K. A.; Cava, R. J. *Inorg. Chem.* **2014**, *53*, 10989–10995.
- [28] Hagiwara, M.; Kanaboshi, A.; Frandroy, S.; Biensan, P.; Matsuura, M. *Journal of Magnetism and Magnetic Materials* **1990**, *90-91*, 277–278.
- [29] Huang, S.; Ling, X.; Liang, L.; Kong, J.; Terrones, H.; Meunier, V.; Dresselhaus, M. S. *Nano Letters* **2014**, *14*, 5500–5508.
- [30] Novoselov, K. S.; Jiang, D.; Schedin, F.; Booth, T. J.; Khotkevich, V. V.; Morozov, S. V.; Geim, A. K. *Proceedings of the National Academy of Sciences* **2005**, *102*, 10451–10453.
- [31] Benameur, M. M.; Radisavljevic, B.; Héron, J. S.; Sahoo, S.; Berger, H.; Kis, A. *Nanotechnology* **2011**, *22*, 125706–125710.
- [32] Zheng, J.; Zhang, H.; Dong, S.; Liu, Y.; Tai Nai, C.; Suk Shin, H.; Young Jeong, H.; Liu, B.; Ping Loh, K. *Nature Communications* **2014**, *5*, 2995.
- [33] Nagashio, K.; Yamashita, T.; Nishimura, T.; Kita, K.; Toriumi, A. *J. Appl. Phys.* **2011**, *110*, 024513.
- [34] Eda, G.; Yamaguchi, H.; Voiry, D.; Fujita, T.; Chen, M.; Chhowalla, M. *Nano Lett.* **2011**, *11*, 5111–5116.
- [35] Szendrei, K.; Ganter, P.; Sánchez-Sobrado, O.; Eger, R.; Kuhn, A.; Lotsch, B. V. *Adv. Mater.* **2015**, *27*, 6341–6348.
- [36] Yang, D.; Frindt, R. F. *Journal of Applied Physics* **1996**, *79*, 2376.

- [37] Breu, J.; Seidl, W.; Stoll, A. *Zeitschrift für anorganische und allgemeine Chemie* **2003**, *629*, 503–515.
- [38] Tsai, H.-L.; Heising, J.; Schindler, J. L.; Kannewurf, C. R.; Kanatzidis, M. G. *Chemistry of Materials* **1997**, *9*, 879–882.
- [39] Sasaki, T.; Watanabe, M. *Journal of the American Chemical Society* **1998**, *120*, 4682–4689.
- [40] Omomo, Y.; Sasaki, T.; Wang,; Watanabe, M. *Journal of the American Chemical Society* **2003**, *125*, 3568–3575.
- [41] Fukuda, K.; Kato, H.; Sato, J.; Sugimoto, W.; Takasu, Y. *J. Solid State Chem.* **2009**, *182*, 2997–3002.
- [42] Wallace, D. C.; McQueen, T. M. *Dalton Trans.* **2015**, *44*, 20344–20351.
- [43] Regnault, L. P.; Rossat-Mignod, J. In *Magnetic Properties of Layered Transition Metal Compounds*; de Jongh, L. J., Ed.; Kluwer Academic Publishers, 1990; Vol. 9; pp 271–322.
- [44] Jackeli, G.; Khaliullin, G. *Physical Review Letters* **2009**, *102*, 017205.
- [45] Rau, J. G.; Lee, E. K.-H.; Kee, H.-Y. *Phys. Rev. Lett.* **2014**, *112*, 077204.

3 Trivalent Iridium Oxides: Layered Triangular Lattice Iridate $\text{K}_{0.75}\text{Na}_{0.25}\text{IrO}_2$ and Oxyhydroxide IrOOH

Daniel Weber, Leslie M. Schoop, Daniel Wurmbrand, Jürgen Nuss, Elizabeth M. Seibel, Fazel Fallah Tafti, Huiwen Ji, Robert J. Cava, Robert E. Dinnebier, Bettina V. Lotsch

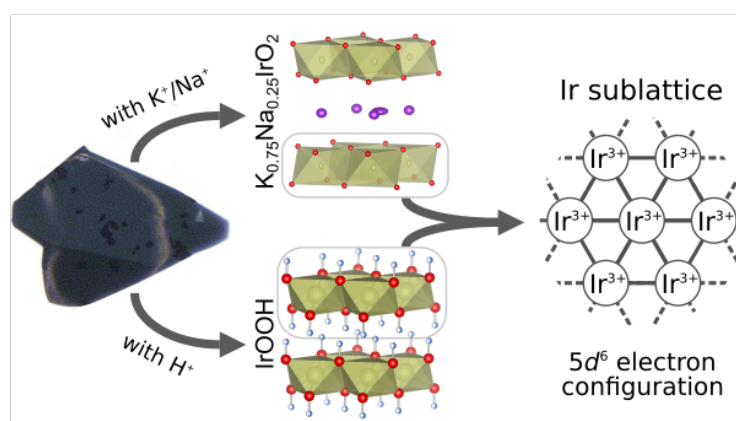
submitted to: *Chemistry of Materials*.

Reprinted (adapted) with permission from *Chemistry of Materials*. Copyright 2017 American Chemical Society.

Abstract

Solid oxides with transition metals ions in unusual oxidation states attract enormous attention due to their electronic, magnetic and catalytic properties. Yet, no crystalline oxide compounds based on purely trivalent iridium have been characterized to date. Here, we present the synthesis and thorough investigation of the properties of the compounds $\text{K}_{0.75}\text{Na}_{0.25}\text{IrO}_2$ and IrOOH , both containing trivalent iridium on a triangular lattice in

layers of $[\text{IrO}_2]^-$. $\text{K}_{0.75}\text{Na}_{0.25}\text{IrO}_2$ crystallizes in a P2-structure with the space group $P6_3/mmc$, while the crystal structure of IrOOH adopts the direct maximal subgroup $P\bar{3}m1$. The trivalent state of the iridium ion is discussed with regards to the iridium-oxygen bond length from X-ray diffraction, the chemical composition, the electronic and magnetic behavior of the material as well as X-ray photoemission spectroscopy. The discovery of a new valence state in ternary crystalline iridium oxides is not only of interest from a fundamental perspective, but has far-reaching implications for such diverse fields as electrochromism, solid-state magnetism, and especially heterogeneous catalysis.



3.1 Introduction

Layered ternary oxides exhibit a large variety of exciting electronic and magnetic properties due to their two-dimensional nature and their inherent anisotropy, with examples ranging from transparent conductors¹ and self-healing semiconductors for solar-driven water splitting² to frustrated magnets³ and metallic oxides with unusually high conductivities along oxide layers.⁴

In A_xBO_2 compounds with alkaline ions on the A site and transition metals on the B site, the crystal structures are composed of $[BO_2]^-$ layers of edge sharing BO_6 octahedral and alkali ions in the interlayer space. Other structure determining factors are the octahedral (O), prismatic (P) or tetragonal environment of the alkali ion as well as the number of layers per unit cell, which depends on the packing of the oxide ions. Examples are the O3 structure with an $ABCABC$ stacking in α - $NaFeO_2$ or the P2 structure with an $ABBA$ oxide stacking in Na_xCoO_2 .⁵

Yet, no ABO_2 compounds where the B site is purely occupied by iridium have been unambiguously identified up to date. The examples that are closest to a full iridium occupancy of the B site are Li_2IrO_3 ,⁶ Na_2IrO_3 ,³ $Cu_3LiIr_2O_6$, $Cu_3NaIr_2O_6$ ⁷ or $Ag_3LiIr_2O_6$.⁸ The rewritten sum formula $A[B'_{1/3}Ir_{2/3}]O_2$ with $B' = Li, Na$ shows that the B site in the BO_2^- layer is occupied to one third by alkali ions and two thirds by Ir^{4+} ions, which form a honeycomb lattice. Besides, a layered compound with the approximate formula sum $K_xIr_yO_z \cdot nH_2O$ has been mentioned in the literature⁹ but a structural characterization, or discussion of the exact composition or oxidation states is lacking.

As spin-orbit coupling is strong in iridium, layered iridates feature many interesting effects such as frustrated magnetism in layered Na_2IrO_3 ³ or a Mott insulating state in Sr_2IrO_4 ,¹⁰ making them worthwhile compounds to investigate.

Here, we present the synthesis of the layered compound $K_{0.75}Na_{0.25}IrO_2$ and investigate

its crystal structure, electrical, and magnetic properties. This is the first report of a crystal structure with fully occupied triangular $[\text{IrO}_2]^-$ layers featuring exclusively trivalent iridium ions in an IrO_6 octahedral environment, in contrast to the mixed valence phases with the hollandite structure^{11,12} or the amorphous electrocatalyst IrO_x .¹³ We note that the compounds reported here might be similar to the layered material $\text{K}_x\text{Ir}_y\text{O}_z \cdot n\text{H}_2\text{O}$, which has been used as a starting material to synthesize a layered electrocatalyst, but has not yet been investigated.⁹ Most importantly, neither the exact composition nor the crystal structure of this material are known. We also show the preparation of the compound IrOOH by ion exchange from its structural relative $\text{K}_{0.75}\text{Na}_{0.25}\text{IrO}_2$, as well as investigations of its physical properties, emphasizing the stability of the $[\text{IrO}_2]^-$ structural motif. The valence state of iridium in both compounds will be discussed in light of the Ir-O bond lengths as well as the observed electrical and magnetic behavior.

3.2 Experimental

Single crystals of $\text{K}_{0.75}\text{Na}_{0.25}\text{IrO}_2$ were prepared by heating 1 eq. iridium and 9 eq. of flux containing 90 mol% dried K_2CO_3 and 10 mol% dried Na_2CO_3 in air for 5-7 days. In the absence of Na_2CO_3 , KIr_4O_8 and other side phases formed instead of KIrO_2 . Note that this in contrast to the report of the phase $\text{K}_x\text{Ir}_y\text{O}_z \cdot n\text{H}_2\text{O}$,⁹ where a layered phase (besides many side phases) was found without the presence of sodium. Despite many attempts, we were not able to obtain a layered compound in the absence of sodium, which is why we conclude that sodium is necessary for a quantitative yield of the layered material. The product was quenched into an argon atmosphere to avoid hydration. Thin (< 0.1 mm), transparent crystalline platelets of dark blue color with a diameter of 3-5 mm grew on top of the melt, which contained microcrystalline $\text{K}_{0.75}\text{Na}_{0.25}\text{IrO}_2$ and a water soluble side phase. Crystals were heated at 600 °C in the presence of microcrystalline product and flux

for two weeks in air to remove stacking faults.

IrOOH was prepared by shaking the microcrystalline powder of $\text{K}_{0.75}\text{Na}_{0.25}\text{IrO}_2$ in 1 M HCl for 5 days. The acid to solid ratio was 1 mL mg^{-1} and the acid was exchanged daily. Washing with water and drying at 100°C for 30 min yielded the product. Macroscopically, the resulting powder has a violet metallic luster, yet under the microscope thin platelets of IrOOH are transparent and blue, similar to $\text{K}_{0.75}\text{Na}_{0.25}\text{IrO}_2$.

Single crystalline samples were characterized by single crystal X-ray diffraction (SXRD) on a Bruker three circle diffractometer with an Apex-I CCD detector using Mo- K_α radiation ($\lambda = 0.71073 \text{ \AA}$) at temperatures of 250 K and 100 K. The data was analyzed using SHELX.¹⁴ Powder X-ray diffraction (PXRD) was performed on a Stoe StadiP utilizing Ag- $\text{K}_{\alpha 1}$ radiation (Ge(111) monochromator, $\lambda = 0.559410 \text{ \AA}$) with a Dectris Mythen 1K detector in Debye-Scherrer geometry. The layered samples were gently ground with glass powder to avoid intensity aberration due to preferred orientation, which results in an amorphous halo between approximately 3 and $17^\circ 2\theta$. PXRD data was analyzed with Topas 5 by Bruker AXS.

A Vega TS 5130 MM SEM by Tescan with a Si/Li EDX-detector by Oxford Instruments was used for imaging and determination of the elemental composition.

Measurements of the magnetic susceptibility were performed on a MPMS by Quantum Design in a field of 1 T on the single crystalline and powdered samples. Data on the electric conductivity was collected on a PPMS by Quantum Design by contacting a single crystal of $\text{K}_{0.75}\text{Na}_{0.25}\text{IrO}_2$ or, in the case of IrOOH, a pressed powder pellet. X-ray photoemission spectroscopy was carried out in a commercial KRATOS AXIS ULTRA system with a monochromatized Al K_α source (1486.6 eV) with a base pressure in the lower 10^{-10} mbar range. The binding energy (BE) was calibrated by setting the C 1s BE to 284.8 eV with respect to the Fermi level. High-resolution spectra were acquired with an analyzer pass energy of 20 eV. Analysis of the XPS data was performed with CasaXPS software.

Electronic structure calculations on $\text{K}_{0.75}\text{Na}_{0.25}\text{IrO}_2$ were performed in the framework of density functional theory using the WIEN2K¹⁵ code with a full-potential linearized augmented plane-wave and local orbitals [FP-LAPW + lo] basis¹⁶ together with the Perdew-Becke-Ernzerhof (PBE) parameterization¹⁷ of the generalized gradient approximation as the exchange-correlation functional. The plane-wave cutoff parameter $R_{\text{MT}}K_{\text{MAX}}$ was set to 7 and the irreducible Brillouin zone was sampled by 132 k-points. Experimental lattice parameters from the X-ray diffraction study were used in the calculations. The interlayer cations were modeled with K sitting on 1/3, 2/3, 1/4. Spin-orbit coupling was included as a second variational procedure.

3.3 Results and discussion

3.3.1 Crystal structure and composition of $\text{K}_{0.75}\text{Na}_{0.25}\text{IrO}_2$

The structure of $\text{K}_{0.75}\text{Na}_{0.25}\text{IrO}_2$ was determined from single crystal x-ray diffraction. The diffraction pattern was indexed to a hexagonal cell with the lattice parameters $a = 3.1202(5)$ Å and $c = 12.440(2)$ Å at a temperature of 250 K. A second measurement at lower temperatures indicated no structural change down to 100 K. The structure was refined in the space group $P6_3/mmc$ and the positions of iridium, potassium, sodium and oxygen ions were determined during the structure solution. The crystallographic data, atom positions and atomic displacement parameters are displayed in Table S1 to S3. The alkali ions were assumed to occupy the same position, which had to be split due to disorder of the interlayer cations (positions Na1/K1 and Na2/K2, see appendix). The K : Na ratio was determined by SEM-EDX to be 3 : 1, as listed in Table S6.

$\text{K}_{0.75}\text{Na}_{0.25}\text{IrO}_2$ is composed of layers of edge sharing iridium oxide octahedra with a distance of $d(\text{Ir-O})$ of $2.070(5)$ Å separating the iridium and oxide ions. The alkali ions

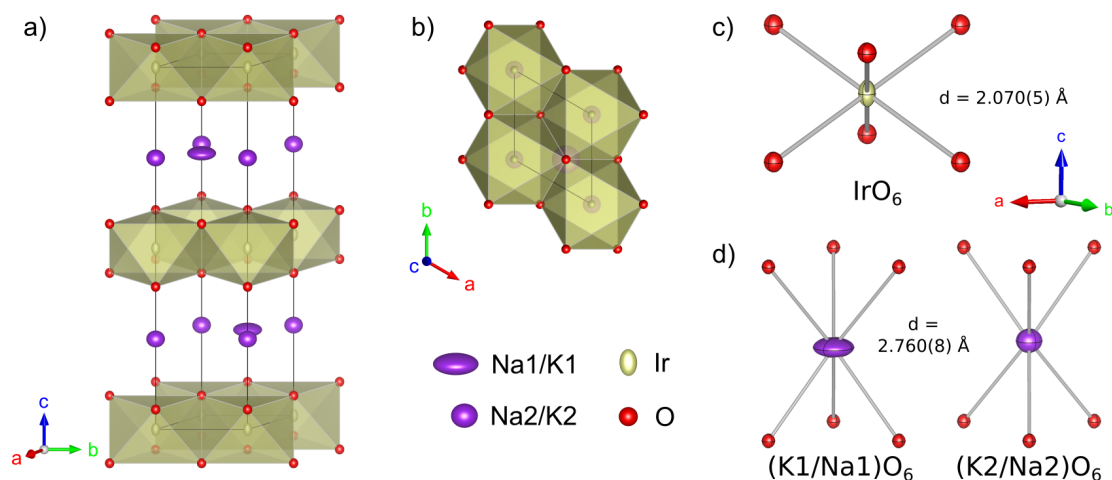


Figure 3.1: Projection of the unit cell of $\text{K}_{0.75}\text{Na}_{0.25}\text{IrO}_2$ with anisotropic ADPs, displayed along the a) $[201]$ and b) $[001]$ zone axis, c) and d) show the first coordination sphere of the Ir and (K,Na) position.

occupy the interlayer space, surrounded by a trigonal prismatic coordination shell. Most of the sodium contained in the compound is located on position 1, with a plate-like anisotropic displacement, indicating that the trigonal prismatic coordination shell is too large for sodium (see Figure 3.1 d), and Figure B.4). Position 2 is almost completely occupied by potassium, and shows isotropic behavior. Thus, $\text{K}_{0.75}\text{Na}_{0.25}\text{IrO}_2$ crystallizes in a P2-type structure according to the notation of Delmas and Hagenmuller.⁵ The Ir-O octahedra are distorted with O-Ir-O angles of $82.2(3)^\circ$, $97.8(3)^\circ$ and $180.0(5)^\circ$. Both (K,Na) positions are prismatically coordinated by oxide ions at a distance of $d = 2.760(8) \text{ \AA}$. Therefore, $\text{K}_{0.75}\text{Na}_{0.25}\text{IrO}_2$ is isostructural to the P2 alkali compounds KCrO_2 ¹⁸ and KTlO_2 ,¹⁹ in which the alkali-oxide distances are $d(\text{K-O}) = 2.669 \text{ \AA}$ and 2.639 \AA , respectively. All interatomic distances and angles are summarized in Table 3.1.

The $[\text{IrO}_2]^-$ layer consists of trivalent iridium ions arranged on a triangular lattice, which is a structural motif not yet observed in an iridium oxide crystal structure. The closest structural relatives are the layered compounds Li_2IrO_3 ,⁶ Na_2IrO_3 ²⁰ and their ion-exchange products $\text{Cu}_3\text{LiIrO}_6$, $\text{Cu}_3\text{NaIrO}_6$ ⁷ and $\text{Ag}_3\text{LiIrO}_6$,⁸ in which iridium assembles

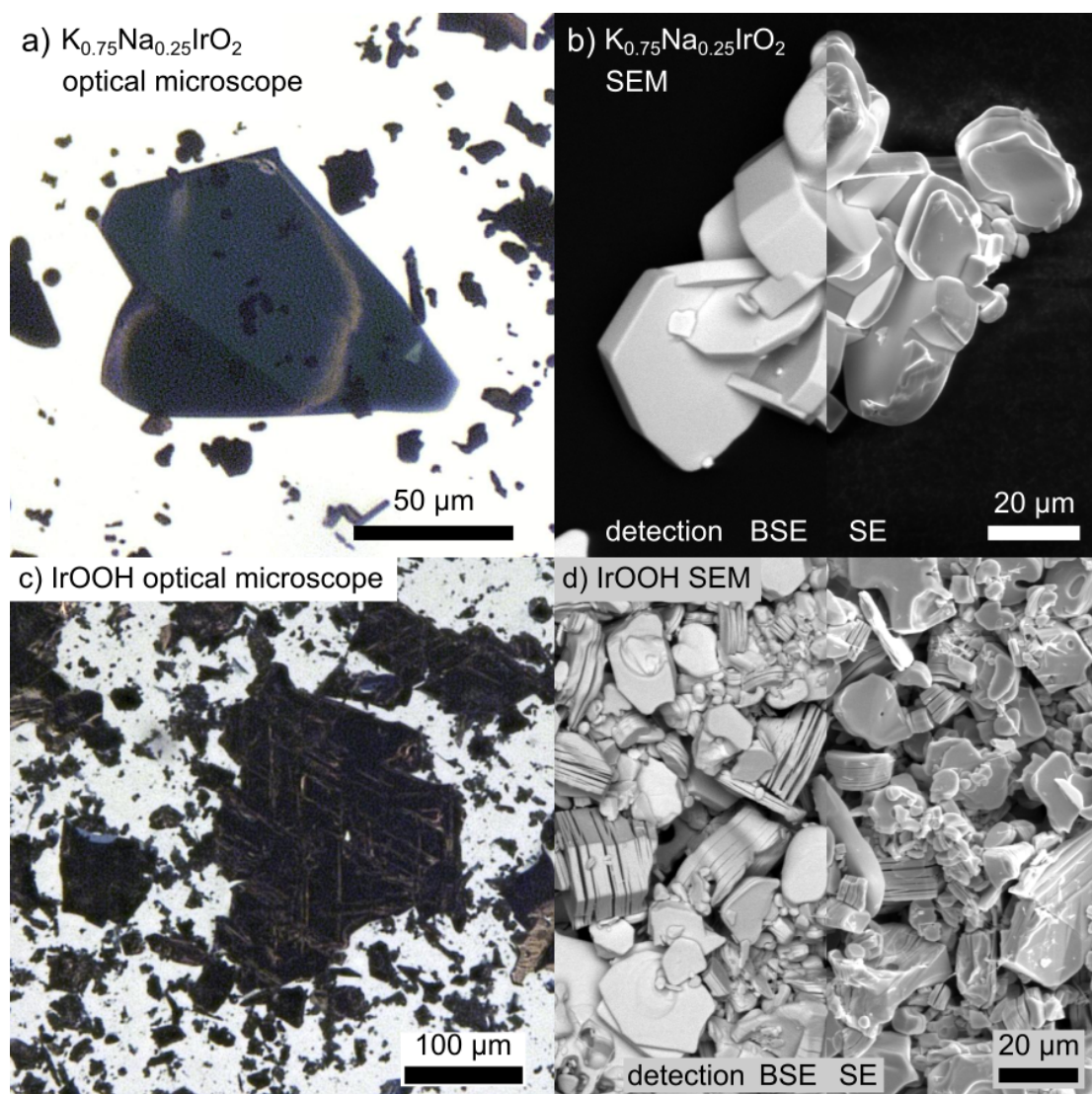


Figure 3.2: Optical microscopy (left) and SEM images (right) of $\text{K}_{0.75}\text{Na}_{0.25}\text{IrO}_2$ and IrOOH ; SEM recorded with BSE (left) and SE (right) detection.

in a honeycomb layer. While the structural relatives contain tetravalent iridium, the composition and crystal structure of $\text{K}_{0.75}\text{Na}_{0.25}\text{IrO}_2$ suggest a trivalent iridium occupying a triangular lattice, which is unprecedented in crystalline ternary oxoironates.

Optical and electron microscopy As seen in the optical microscopy image in Figure 3.2 a), the crystals are translucent and of blue color. The SEM image shows the hexagonal

Table 3.1: Interatomic distances (\AA) and angles ($^\circ$) in $\text{K}_{0.75}\text{Na}_{0.25}\text{IrO}_2$ at 250 K.

Ir-O	2.070(5)	O-Ir-O	82.2(3)
		O-Ir-O	97.8(3)
		O-Ir-O	180.0(5)
(K,Na)-O	2.760(8)	O-(K,Na)-O	68.8(2)
		O-(K,Na)-O	98.5(3)
		O-(K,Na)-O	141.90(12)

platelet morphology of the microcrystallites. The elemental distribution is homogeneous as can be seen by back-scattered electron (BSE) detection. SEM-EDX shows that the K : Na ratio is 3 : 1, while the alkaline ion (K + Na) to iridium ratio is 1 : 1 within the margin of error of EDX. The results are reproducible over several batches of samples and listed in Table S6.

3.3.2 Crystal structure and composition of IrOOH

By immersing $\text{K}_{0.75}\text{Na}_{0.25}\text{IrO}_2$ in diluted hydrochloric acid for several days, the phase IrOOH was obtained. The morphology of the IrOOH crystallites was not altered by the ion-exchange, as can be seen by comparing Figures 3.2 b) and d). Elemental analysis by SEM-EDX shows no sodium and ≤ 1 mol% potassium relative to iridium present in the sample. The results are reproducible over several batches, as shown by the EDX data listed in Table S6. The crystallites are cleaved perpendicular to the stacking direction by the ion exchange reaction. Although the morphology is retained, the diffraction pattern of IrOOH in Figure 3.3 a) differs significantly from the pattern of $\text{K}_{0.75}\text{Na}_{0.25}\text{IrO}_2$ in peak positions as well as broadened peak shapes. Anisotropic peak broadening is present, and while reflections with the Miller indices $hk0$ remain sharp, peaks with non-zero l components broaden due to cracks in the crystals perpendicular to the stacking direction, indicating the reduced

Table 3.2: Interatomic distances (\AA) and angles ($^\circ$) in IrOOH ; values without standard deviation were generated by symmetry relation.

Ir-O	2.041(4)	O-Ir-O	80.6(3)
		O-Ir-O	99.4(3)
		O-Ir-O	180.0

crystallite size along the c -axis. The crystallographic data along with the atomic positions are displayed in Table S4 and S5.

Indexing of the diffraction pattern of IrOOH results in a hexagonal cell with the lattice parameters $a = 3.11345(9) \text{ \AA}$ and $c = 4.6396(3) \text{ \AA}$. The intensities were extracted by applying a Pawley fit to the diffraction pattern. The presence of a Hollandite side phase, KIr_4O_8 , and the amorphous halo from the glass powder were taken into account during intensity extraction. Spherical harmonics were used to simulate the direction-dependent broadening of the line shape.²¹ The initial model for the atomic positions was deduced by using the structural model of $\text{K}_{0.75}\text{Na}_{0.25}\text{IrO}_2$, removing the alkaline ion positions and adjusting the number of formula units per unit cell Z as well as the atomic positions to the modified lattice parameters. The position of H^+ was not included into the refinement. The crystal structure of IrOOH was determined from the PXRD pattern in the presence of 16(1) wt% of the Hollandite KIr_4O_8 as a side phase.

IrOOH consists of trigonal layers of edge sharing Ir-O octahedra, similar to the CdI_2 structure type, indicating the retention of the layered motif during the ion exchange. The space group is $P\bar{3}m1$, which is also found in the mineral Brucite $\text{Mg}(\text{OH})_2$ and its structural relatives $\text{M}(\text{OH})_2$ with $\text{M} = \text{Ca}, \text{Mn}, \text{Co}, \text{Ni}, \text{Cd}$. It should be noted that the space group $P\bar{3}m1$ is symmetry related to $P6_3/mmc$. In $P\bar{3}m1$, a cell with the doubled volume ($a, b, 2c$) is a maximal *klassengleiche* isomorphic subgroup, to which $P6_3/mmc$ is a supergroup. Compared to $\text{K}_{0.75}\text{Na}_{0.25}\text{IrO}_2$, the in-plane lattice parameters of IrOOH are similar with a

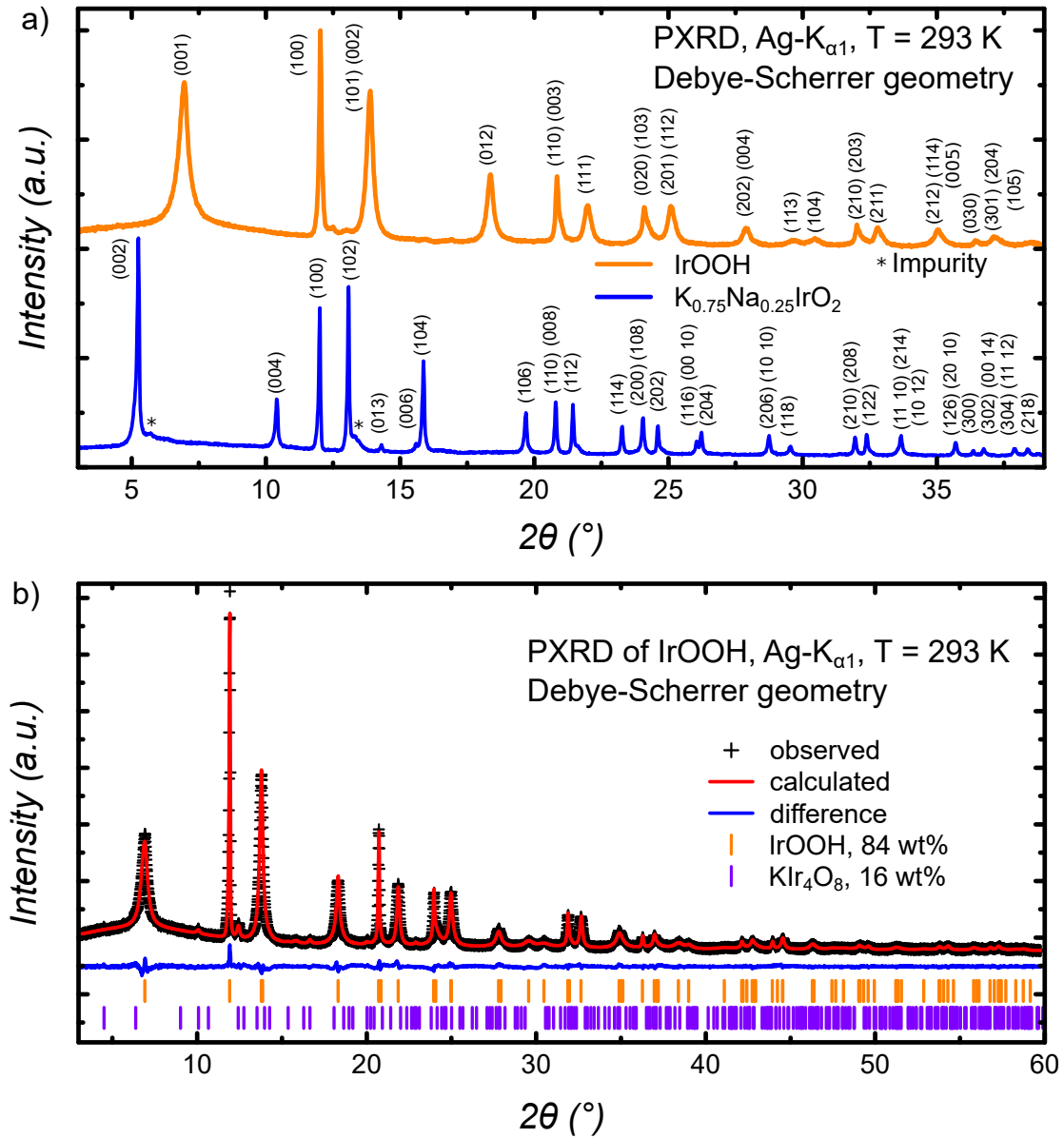


Figure 3.3: a) Comparison of PXRD diffraction patterns of IrOOH and $K_{0.75}Na_{0.25}IrO_2$, b) observed and calculated diffraction pattern of IrOOH as well as the difference curve as determined by Rietveld refinement; ticks mark the positions of reflections for IrOOH and KIr_4O_8 .

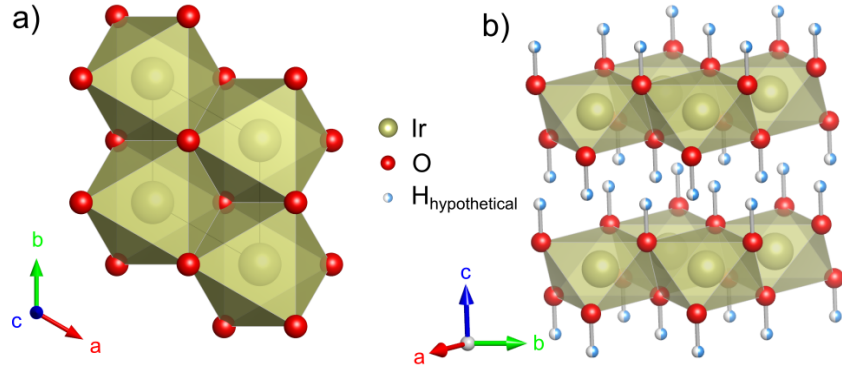


Figure 3.4: Representation of the crystal structure of IrOOH along the a) $[001]$ and b) $[411]$ zone axis, including hypothetical positions of protons.

$= 3.1 \text{ \AA}$. The interlayer distance of the iridium oxide layer shrinks from $d_{(002)} = 6.2 \text{ \AA}$ found in $\text{K}_{0.75}\text{Na}_{0.25}\text{IrO}_2$ to $d_{(001)} = 4.6 \text{ \AA}$ in the proton exchanged compound due to the smaller ionic radius of H^+ , similar to other $\text{M}(\text{OH})_2$ and MOOH compounds as seen in Table 3.3. The change in symmetry also results in a reduction of formula units per unit cell from $Z = 2$ to $Z = 1$. The crystal structure of IrOOH is displayed in Figure 3.4 including the estimated H^+ position in Figure 3.4 b). The crystallographic data and atom positions are listed in Tables S4 and S5.

The Ir-O distances of 2.04 \AA in IrOOH are similar to the distance of 2.07 \AA in the K,Na-compound, indicating that the bonding in IrOOH remains similar to $\text{K}_{0.75}\text{Na}_{0.25}\text{IrO}_2$ after the ion-exchange. Based on the lack of electron density between the layers detected

Table 3.3: Layer heights in $\text{M}(\text{OH})_2$ and MOOH compounds.

Compound	$d \text{ [\AA]}$	Compound	$d \text{ [\AA]}$
$\text{Ca}(\text{OH})_2^{22}$	4.9035(3)	IrOOH	4.6396(3)
$\text{Mg}(\text{OH})_2^{23}$	4.7713(1)	CrOOH^{24}	4.45383(7)
$\text{Mn}(\text{OH})_2^{25}$	4.7699(5)	CoOOH^{26}	4.3833(17)
$\text{Cd}(\text{OH})_2^{27}$	4.7059(1)	CoOOD^{26}	4.4513(17)

in PXRD, the presence of water or hydroxonium ions in the interlayer space was excluded. This is also supported by the short c axis of 4.63 Å, as hydrated layered compounds usually show layer spacings of 6-7 Å,²⁸ as well as by the thermogravimetric measurement of IrOOH, displayed in Figure S1, where no weight loss is observed up to 200 °C. The bond valence analysis, similar magnetic properties of IrOOH compared to $\text{K}_{0.75}\text{Na}_{0.25}\text{IrO}_2$, as well as photoemission spectroscopy indicate a trivalent state of the transition metal and the presence of one proton due to charge neutrality.

The crystal structures of $\text{M}(\text{OH})_2$ (space group $P\bar{3}m1$, $\text{M} = \text{Mg, Ca, Mn, Co, Ni, Cd}$) and $\text{MO}(\text{OH})$ (space group $R\bar{3}mh$, $\text{M} = \text{Co, Cr}$) allow the estimation of the proton position in the interlayer space. In $\text{MO}(\text{OH})$ compounds, the O-H bond ranges from 0.91(2) Å in CrOOH ²⁹ to 1.248(11) Å in CoOOH ²⁶, while in the $\text{M}(\text{OH})_2$ compounds, the distance ranges from $d = 0.956(5)$ in $\text{Mg}(\text{OH})_2$ to $d = 1.041$ Å in $\text{Mn}(\text{OH})_2$.^{25,30} Figure 3.4 b) shows the most likely arrangement of the proton with an estimated O-H distance of 1 Å.

3.3.3 Bond valence analysis

To estimate the valence of iridium, a bond valence analysis of the Ir-O bond was performed based on Equation 3.1 and the parameters predicted by Gagné and Hawthorne³¹:

$$S_{ij} = \exp \frac{R_0 - R_{ij}}{B} \quad (3.1)$$

with S_{ij} being the bond valence between atom i and j , R_{ij} is the measured bond length and R_0 as well as B are the bond-valence parameters. In $\text{K}_{0.75}\text{Na}_{0.25}\text{IrO}_2$, each Ir-O bond is 2.070 Å long and carries 0.467 valence units. Therefore, the valence sum on iridium is 2.804, which is in good agreement with the trivalent state implied by the composition. For IrOOH, the bond valence analysis yields 0.501 valence units per Ir-O bond at an Ir-O

distance of 2.041 Å. The bond valence sum of 3.006 valence units per Iridium indicates the retention of the trivalent state of the iridium ion. A graph comparing the bond valences of various compounds containing tri-, tetra- and pentavalent iridium-oxygen octahedra is displayed in Figure 3.5. The valence bond values as well as the various structure types are listed in Table B.7 and B.8. As no structural information on crystalline solids with trivalent iridium surrounded by oxygen are known in the literature, the validity of the measured data was compared to Ir^{3+} -O distances in amorphous $H_3[Ir(C_2O_4)_3] \cdot 2H_2O$. There, the average Ir-O distance was determined to be $d(Ir-O) = 2.02(6)$ Å by X-ray absorption spectroscopy under the assumption of an octahedral coordination of iridium by oxalate anions, validating the measured distances in $K_{0.75}Na_{0.25}IrO_2$ and $IrOOH$.

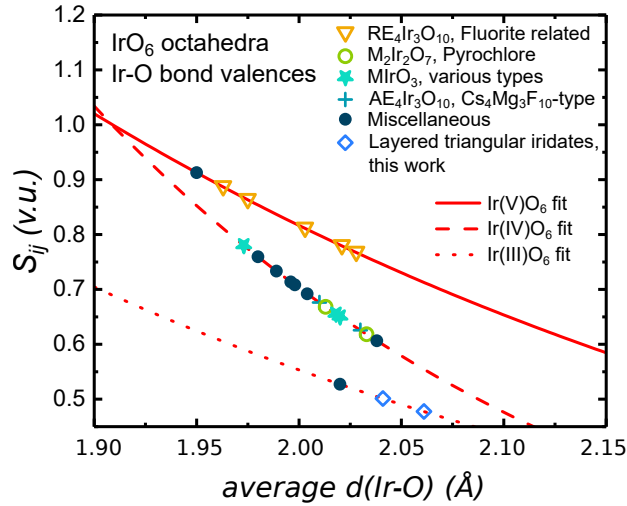


Figure 3.5: Plot of the bond valences of tri-, tetra- and pentavalent iridates containing IrO_6 octahedra against the Ir-O bond length, color denotes structure type, while the shape describes the formal iridium oxidation state; based on data from Table S7 and S8.

3.3.4 Physiscal Properties of $K_{0.75}Na_{0.25}IrO_2$ and $IrOOH$

Electronic conductivity The temperature-dependent resistivity was measured on a single crystal of $K_{0.75}Na_{0.25}IrO_2$ as well as on pelletized $IrOOH$. As seen in Figure 3.6, the

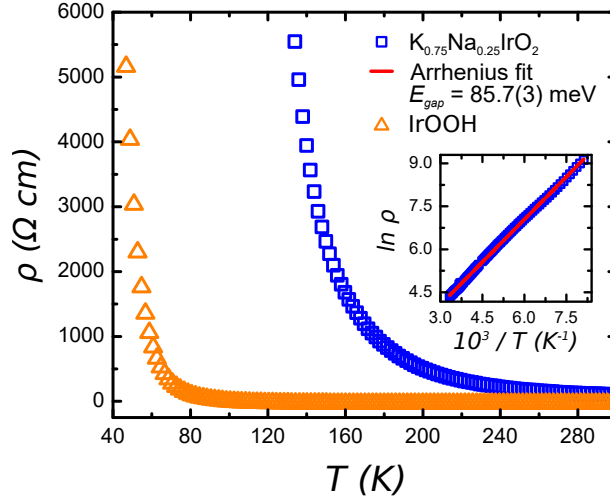


Figure 3.6: Temperature dependent resistivity of $\text{K}_{0.75}\text{Na}_{0.25}\text{IrO}_2$ and IrOOH measured in the range of 40 to 300 K; inset shows Arrhenius plot $\ln \rho(T)$ vs. $10^3/T$ for $\text{K}_{0.75}\text{Na}_{0.25}\text{IrO}_2$.

resistivity in both compounds drops with temperature, indicating semiconducting behavior. To determine the band gap E_{gap} , $\ln \rho$ was plotted against T^{-1} and a linear form of an Arrhenius type equation (eq. 3.3) was fitted to the data.

$$\rho = \rho_0 * \exp \frac{E_{\text{gap}}}{k_B T} \quad (3.2)$$

$$\ln \rho = \frac{E_{\text{gap}}}{k_B} \frac{1}{T} + \ln \rho_0 \quad (3.3)$$

where ρ is the resistivity, E_{gap} the activation energy and k_B Boltzmann's constant. The activation energy was determined to be $E_{\text{gap}} = 85.7(3)$ meV for $\text{K}_{0.75}\text{Na}_{0.25}\text{IrO}_2$. As this value is very low for a semiconductor, this indicates the presence of in-gap states caused by impurities or lattice defects. This is also suggested by band structure calculations based on the PBE functional, which yield a band gap of 0.973 eV. The band structure and DOS are displayed in Figure S1 and S2. In IrOOH , no Arrhenius type behavior was observed due to the presence of impurities, impeding the determination of the band gap via resistivity.

Magnetism $\text{K}_{0.75}\text{Na}_{0.25}\text{IrO}_2$ and IrOOH were investigated by magnetometry, as their magnetic behavior is indicative of the oxidation state of iridium. The data was fitted to the Curie-Weiss law (eq. 3.4-3.6).

$$\chi_{mol} = \frac{C}{T - \theta_{CW}} + \chi_0 \quad (3.4)$$

$$\chi_{mol}^{-1} = \chi_0^{-1} + \frac{T}{C} - \frac{\theta_{CW}}{C} \quad (3.5)$$

$$\mu_{eff} = \sqrt{8C} \quad (3.6)$$

where χ_{mol} is the magnetic susceptibility, C the Curie constant, θ_{CW} the Curie-Weiss temperature, χ_0 the temperature-independent contribution and μ_{eff} the effective magnetic moment.

Oxide compounds with octahedrally coordinated iridium have a strong ligand field inducing a gap between the e_g and t_{2g} states. Due to spin-orbit coupling, the t_{2g} states split into doublet $J_{eff} = \frac{1}{2}$ and quartet $J_{eff} = \frac{3}{2}$ states.^{10,32} With the $5d^6$ electron configuration of Ir^{3+} , all d -electrons should be paired leading to a $J = 0$ ground state and diamagnetic behavior. Thus, the expected magnetic moment μ_{eff} should be low, but not zero, similar to iridates containing Ir^{5+} , where $\mu_{eff} \approx 0.3 \mu_B / \text{Ir}$.³²

Magnetic measurements of single crystals of $\text{K}_{0.75}\text{Na}_{0.25}\text{IrO}_2$ are displayed in Figure 3.7 a). For the single crystals, the signal was lost above 73 K as the magnetic moment shrinks with increasing temperature. This is visible as the error per data point increases with increasing temperature, which is displayed in Figure B.4. As seen in the inverse magnetic susceptibility curve, the sample is a paramagnet. At low temperatures, where the signal is large enough, a fit of the linearized Curie-Weiss law resulted in a Curie constant of $C = 0.00604(4) \text{ emu K}^{-1} \text{ Oe}^{-1} \text{ mol}^{-1} \text{ Ir}$, a Weiss temperature of $\theta_{CW} = -2.4(2) \text{ K}$ and the effective

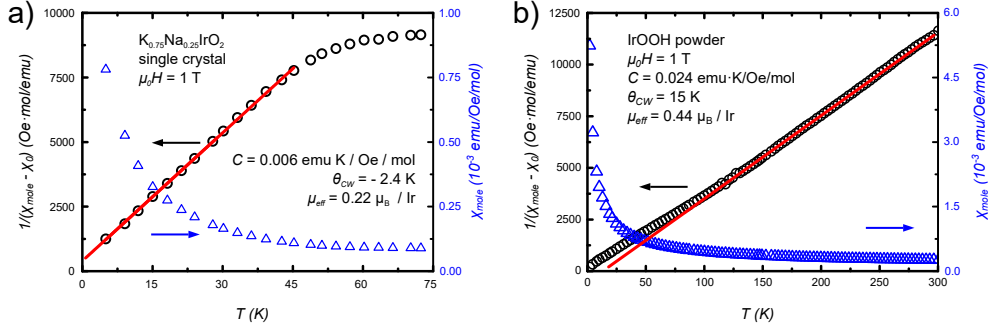


Figure 3.7: Susceptibility (blue) and inverse susceptibility (black) of a) $\text{K}_{0.75}\text{Na}_{0.25}\text{IrO}_2$ single crystals and b) IrOOH powder measured in a field of $\mu_0 H = 1$ T, Curie-Weiss fits shown as a red line.

magnetic moment of $\mu_{\text{eff}} = 0.22 \mu_B / \text{Ir}$. The temperature-independent contribution to the susceptibility χ_0 was found to be $2 \cdot 10^{-5}$ emu Oe $^{-1}$ mol $^{-1}$. No magnetic transition was observed in the magnetic susceptibility before the signal was lost.

In case of IrOOH, the plot of χ_{mol} vs T also shows no magnetic transitions and features paramagnetic behavior, as seen in Figure 3.7 b). The Curie constant $C = 0.024$ emu K $^{-1}$ Oe $^{-1}$ mol $^{-1}$, Curie temperature $\theta_{CW} = 15$ K and effective magnetic moment $\mu_{\text{eff}} = 0.44 \mu_B / \text{Ir}$ were determined from the high temperature data. The correction for the temperature-independent contribution to the susceptibility was $\chi_0 = 1.75 \cdot 10^{-4}$ emu Oe $^{-1}$ mol $^{-1}$ Ir. Compared to $\text{K}_{0.75}\text{Na}_{0.25}\text{IrO}_2$, the data of IrOOH shows a Curie-Weiss-temperature deviating from zero and a slightly increased effective magnetic moment. Yet, the small magnitude of the increased magnetic moment as well as the absence of a ferromagnetic transition indicates that these contributions originate from impurities found in the sample.

The small effective magnetic moment of $0.22 \mu_B / \text{Ir}$ and $0.44 \mu_B / \text{Ir}$ observed in $\text{K}_{0.75}\text{Na}_{0.25}\text{IrO}_2$ and IrOOH is typical for nominally spin paired iridium oxide compounds, as has been recently shown for Ir^{5+} with $\mu_{\text{eff}} \approx 0.3 \mu_B / \text{Ir}$.³² Therefore, the magnetic behavior of $\text{K}_{0.75}\text{Na}_{0.25}\text{IrO}_2$ and IrOOH fits a $J = 0$, $5d^6$ electron configuration of trivalent iridium.

X-ray Photoemission Spectroscopy To further examine the valence state of iridium, XPS was performed on IrOOH , IrO_2 and IrCl_3 , with the results displayed in Figure 3.8 and compared to literature data in Table 3.4. Measurements were also performed on $\text{K}_{0.75}\text{Na}_{0.25}\text{IrO}_2$, yet resulted in very broad, inconclusive peaks of low intensity due to the presence of a thin layer of alkali carbonate flux containing traces of an iridate side phase. For IrOOH , the spectrum was fitted with one additional satellite per peak and yielded binding energies of 62.5 eV and 65.5 eV for the $4f_{7/2}$ and $4f_{5/2}$ peak, respectively. The peak shape of the Ir 4f states was fitted according to the method of Kahk *et al.*,³³ which suggests that more than one peak is necessary for a good fit when both screened and unscreened final states are present. The resistivity data of IrOOH in Figure 3.6 shows that our semiconducting sample has a room temperature conductivity which allows an asymmetric line shape. No additional parameters were needed, excluding the presence of Ir(IV) to below 1 mol%. Note that the hollandite impurity seen in PXRD could be removed for XPS analysis due to the different morphologies of the IrOOH platelets and the hollandite needles.

Binding energies for Ir(III) similar to the measured data were recently published on the amorphous catalyst IrO_x ,³⁴ a highly active water oxidation catalyst investigated by various techniques.^{35–37} This material consists of Ir(III) and Ir(IV) in a ratio of 1 : 4 with iridium in an octahedral coordination shell of oxide or hydroxide ions. The $4f_{7/2}$ and $4f_{5/2}$ Ir(III) peaks appear at 62.4 and 65.4 eV. The binding energies found in IrO_x were validated by theoretical calculations on defective rutile containing Ir(III), yielding calculated binding energies of 62.3 eV and 65.3 eV as well as one satellite per peak. As the calculated binding energies of Ir(III) and the measured data on IrO_x are in good agreement with the data on crystalline IrOOH , this validates the presence of essentially pure Ir^{3+} in IrOOH .

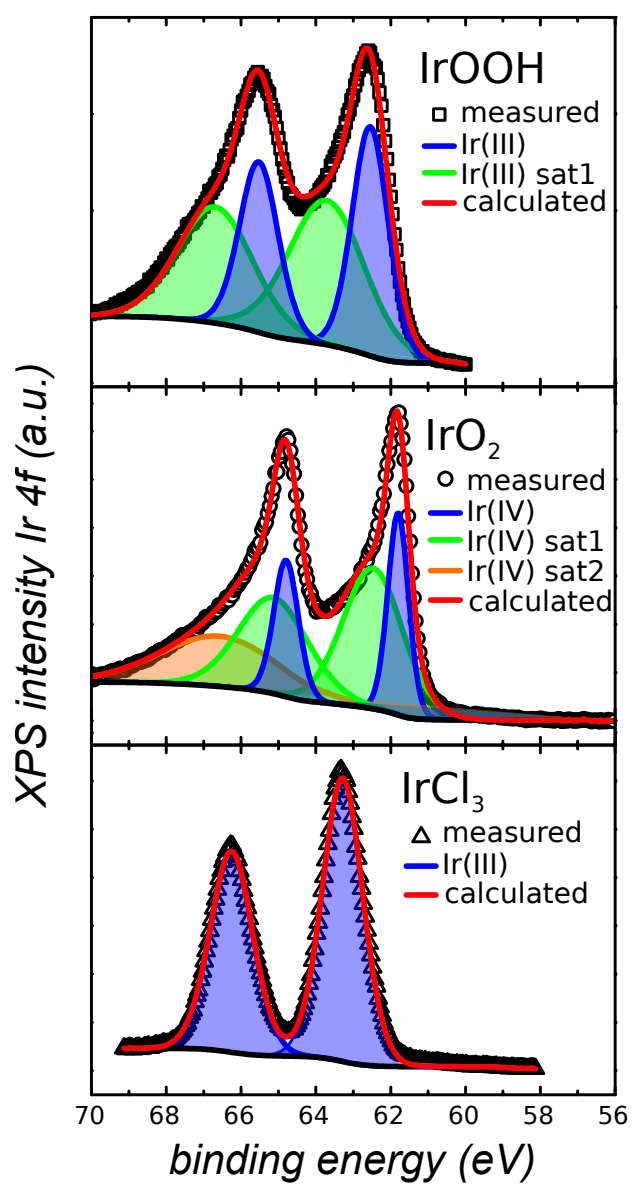


Figure 3.8: XPS spectra of the iridium 4f states of IrOOH, IrO₂ and IrCl₃.

Table 3.4: Energy of XPS peaks for Ir 4*f* states from this work and literature sources.

Source of data	Ir 4 <i>f</i> _{7/2}	Ir 4 <i>f</i> _{5/2}
IrOOH	62.5 eV	65.5 eV
Ir ³⁺ in IrO _x ³⁴	62.4 eV	65.4 eV
Ir ³⁺ defect in rutile-IrO ₂ ³⁴	62.3 eV	65.3 eV
Ir ³⁴	60.9 eV	63.9 eV
IrO ₂ ³⁴	61.7 eV	64.7 eV
IrCl ₃	63.3 eV	66.2 eV

Discussion of the valence state of iridium In the previous sections, we presented the experimental data for $\text{K}_{0.75}\text{Na}_{0.25}\text{IrO}_2$ and IrOOH . For the alkaline compound, the composition was determined by SEM-EDX to have an alkaline ion to iridium ratio of 1:1. The average iridium-oxygen bond lengths were obtained from X-ray diffraction measured on $\text{K}_{0.75}\text{Na}_{0.25}\text{IrO}_2$ single crystals and IrOOH powder, respectively. The average Ir-O distances are longer for $\text{K}_{0.75}\text{Na}_{0.25}\text{IrO}_2$ and IrOOH compared to the bonds in tetravalent iridates in an octahedral environment. The bond valence analysis based on the parameters predicted by Gagné and Hawthorne yields a trivalent state for $\text{K}_{0.75}\text{Na}_{0.25}\text{IrO}_2$ as well as IrOOH . Resistivity measurements on both compounds show semiconducting behavior, which indicates the electron localization due to the $5d^6$ electron state of iridium. In $\text{K}_{0.75}\text{Na}_{0.25}\text{IrO}_2$, this coincides with the results from electronic band structure calculations, yielding a band gap of 0.973 eV. The resistivity of $\text{K}_{0.75}\text{Na}_{0.25}\text{IrO}_2$ follows an Arrhenius type activation mechanism. In combination with magnetometry, the resistivity allows the exclusion of Pauli paramagnetism which would be present in mixed valence iridium ions and leads to metallic conductivity, as seen in Ir(IV) containing iridates with the hollandite structure.^{12,38} Purely tetravalent iridium ions were also excluded due to the effective magnetic moment, which is considerably smaller than the spin-only value of $1.73 \mu_B/\text{Ir}$.

Hence, the low magnetic moments of 0.2 and 0.4 μ_B / Ir for $\text{K}_{0.75}\text{Na}_{0.25}\text{IrO}_2$ and IrOOH are indicative of Ir^{3+} with $J = 0$, similar to Ir^{5+} .³² In XPS, IrOOH features iridium 4*f* binding energies which are in good agreement to the data obtained from theoretical calculations on Ir defects in rutile- IrO_2 as well as XPS measurements on the amorphous mixed valence compound $\text{Ir}^{3.8+}\text{O}_x$.

Past theoretical studies on binary iridium oxide showed a propensity to adopt the rutile structure over the corundum structure, based on the relativistic contraction of the 6*s* orbital and the expansion of the 5*d* orbitals.³⁹ This emphasizes the tendency of iridium to be in the tetravalent state, which is reflected by the large number of Ir^{4+} -containing oxide compounds compared to iridates of higher oxidation states. This trend is summarized in Figure 3.5. The interplay of iridium oxide oxidation states is especially interesting for catalysis, where various cycles involving iridium in the oxidation states III, IV and V have been proposed to explain the extraordinary electrocatalytic activity of rutile- IrO_2 , amorphous IrO_x and layered iridium oxide materials towards oxygen evolution from water.^{9,13,35–37} Thus, $\text{K}_{0.75}\text{Na}_{0.25}\text{IrO}_2$ and IrOOH might serve as crystalline model systems to help understand the energetic landscape of oxide catalysts based on Ir^{3+} and represent a valuable addition to the iridate family as exotic examples of an unusual oxidation state in layered iridium oxide compounds.

3.4 Conclusion

We have presented the synthesis of the layered triangular iridate $\text{K}_{0.75}\text{Na}_{0.25}\text{IrO}_2$ at high temperatures as well as the preparation of IrOOH by an ion exchange reaction in acid. X-ray diffraction shows that both compounds crystallize in a layered structure, with the space group $P6_3/mmc$ for the alkali and $P\bar{3}m1$ for the protonated compound. The in-plane lattice parameter a is 3.1 Å in both compounds, but the layer repeating distance shrinks

from $d_{(002)} = 6.2 \text{ \AA}$ in the K,Na-compound to $c = 4.6 \text{ \AA}$ in the protonated compound. The crystal structure contains triangular layers of Ir^{3+} cations, which are octahedrally coordinated by oxide anions, a structural motif not yet observed in ternary iridium oxides. The ABO_2 composition suggests a trivalent state of the iridium cation, a valence unprecedented for iridium octahedrally coordinated by oxide ions. To exclude deviations from the $5d^6$ electron configuration of the trivalent iridium ion, the samples were investigated by magnetometry and resistivity measurements as well as electronic structure calculations in $\text{K}_{0.75}\text{Na}_{0.25}\text{IrO}_2$ and XPS in case of IrOOH . The results show the presence of localized spins as well as a low effective magnetic moment per iridium, confirming the $J = 0$ state in Ir^{3+} . As iridates are of high interest as frustrated magnets as well as electrocatalysts for water splitting, the new valence state and structural motif offer novel insights into the chemistry and physical properties of ternary iridium oxides.

References

- [1] Kawazoe, H.; Yasukawa, M.; Hyodo, H.; Kurita, M.; Yanagi, H.; Hosono, H. *Nature* **1997**, *389*, 939–942.
- [2] Gu, J.; Yan, Y.; Krizan, J. W.; Gibson, Q. D.; Detweiler, Z. M.; Cava, R. J.; Bockarsly, A. B. *J. Am. Chem. Soc.* **2014**, *136*, 830–833.
- [3] Singh, Y.; Gegenwart, P. *Phys. Rev. B* **2010**, *82*, 064412.
- [4] Hicks, C. W.; Gibbs, A. S.; MacKenzie, A. P.; Takatsu, H.; Maeno, Y.; Yelland, E. A. *Phys. Rev. Lett.* **2012**, *109*, 116401.
- [5] Delmas, C.; Fouassier, C.; Hagenmuller, P. *Physica B+C* **1980**, *99*, 81–85.

- [6] OMalley, M. J.; Verweij, H.; Woodward, P. M. *J. Solid State Chem.* **2008**, *181*, 1803–1809.
- [7] Roudebush, J. H.; Ross, K.; Cava, R. *Dalton Trans.* **2016**, *45*, 8783–8789.
- [8] Todorova, V.; Leineweber, A.; Kienle, L.; Duppel, V.; Jansen, M. *J. Solid State Chem.* **2011**, *184*, 1112–1119.
- [9] Takimoto, D.; Fukuda, K.; Miyasaka, S.; Ishida, T.; Ayato, Y.; Mochizuki, D.; Shimizu, W.; Sugimoto, W. *Electrocatalysis* **2017**, *8*, 144–150.
- [10] Kim, B. J.; Jin, H.; Moon, S. J.; Kim, J.-Y.; Park, B.-G.; Leem, C. S.; Yu, J.; Noh, T. W.; Kim, C.; Oh, S.-J.; Park, J.-H.; Durairaj, V.; Cao, G.; Rotenberg, E. *Phys. Rev. Lett.* **2008**, *101*, 076402.
- [11] Bestaoui, N.; Deniard, P.; Brec, R. *J. Solid State Chem.* **1995**, *118*, 372–377.
- [12] Schoop, L. M.; Krizan, J. W.; Gibson, Q. D.; Cava, R. *J. Solid State Chem.* **2014**, *209*, 37–41.
- [13] Kötz, R.; Neff, H.; Stucki, S. *J. Electrochem. Soc.* **1984**, *131*, 72–77.
- [14] Sheldrick, G. M. *Acta Crystallogr., Sect. A: Found. Crystallogr.* **2008**, *64*, 112–122.
- [15] Blaha, P.; Schwarz, K.; Madsen, G.; Kvasnicka, D.; Luitz, J. *WIEN2k: An Augmented Plane Wave + Local Orbitals Program for Calculating Crystal Properties*. 2001.
- [16] Singh, D. J.; Nordstrom, L. *Planewaves, Pseudopotentials, and the LAPW Method*; Springer Science & Business Media, 2006.
- [17] Perdew, J. P.; Burke, K.; Ernzerhof, M. *Phys. Rev. Lett.* **1996**, *77*, 3865.
- [18] Scheld, W.; Hoppe, R. *Z. Anorg. Allg. Chem.* **1989**, *568*, 151–156.

- [19] Hoppe, R.; Werding, G. *Z. Anorg. Allg. Chem.* **1961**, *307*, 174–186.
- [20] Ye, F.; Chi, S.; Cao, H.; Chakoumakos, B. C.; Fernandez-Baca, J. A.; Custelcean, R.; Qi, T. F.; Korneta, O. B.; Cao, G. *Phys. Rev. B* **2012**, *85*, 180403.
- [21] Järvinen, M. *J. Appl. Crystallogr.* **1993**, *26*, 525–531.
- [22] Pavese, A.; Catti, M.; Ferraris, G.; Hull, S. *Phys. Chem. Miner.* **1997**, *24*, 85–89.
- [23] Kazimirov, V. Y.; Smirnov, M.; Bourgeois, L.; Guerlou-Demourgues, L.; Servant, L.; Balagurov, A.; Natkaniec, I.; Khasanova, N.; Antipov, E. *Solid State Ionics* **2010**, *181*, 1764–1770.
- [24] Ichikawa, M.; Gustafsson, T.; Olovsson, I.; Tsuchida, T. *J. Phys. Chem. Solids* **1999**, *60*, 1875–1880.
- [25] Christensen, A.; Ollivier, G. *Solid State Commun.* **1972**, *10*, 609–614.
- [26] Delaplane, R. G. *Journal of Chemical Physics* **1969**, *50*, 1920.
- [27] Hemmingsen, L.; Bauer, R.; Bjerrum, M.; Schwarz, K.; Blaha, P.; Andersen, P. *Inorg. Chem.* **1999**, *38*, 2860–2867.
- [28] Seibel, E. M.; Roudebush, J. H.; Ali, M. N.; Ross, K.; Cava, R. *Inorg. Chem.* **2014**, *53*, 10989–10995.
- [29] Christensen, A.; Hansen, P.; Lehmann, M. *J. Solid State Chem.* **1977**, *21*, 325–329.
- [30] Chakoumakos, B. C.; Horita, J.; Garlea, V. O. *Am. Mineral.* **2013**, *98*, 1–6.
- [31] Gagné, O. C.; Hawthorne, F. C. *Acta Crystallogr., Sect. B: Struct. Sci.* **2015**, *71*, 562–578.

-
- [32] Phelan, B. F.; Krizan, J.; Xie, W.; Gibson, Q.; Cava, R. *Phys. Rev. B* **2015**, *91*, 155117.
- [33] Kahk, J. M. et al. *Phys. Rev. Lett.* **2014**, *112*, 117601.
- [34] Pfeifer, V. et al. *Surf. Interface Anal.* **2016**, *48*, 261–273.
- [35] Hillman, A. R.; Skopek, M. A.; Gurman, S. J. *Phys. Chem. Chem. Phys.* **2011**, *13*, 5252–5263.
- [36] Reier, T.; Teschner, D.; Lunkenbein, T.; Bergmann, A.; Selve, S.; Kraehnert, R.; Schlögl, R.; Strasser, P. *J. Electrochem. Soc.* **2014**, *161*, F876–F882.
- [37] Minguzzi, A.; Lugaresi, O.; Achilli, E.; Locatelli, C.; Vertova, A.; Ghigna, P.; Rondinini, S. *Chem. Sci.* **2014**, *5*, 3591–3597.
- [38] Talanov, A.; Phelan, W. A.; Kelly, Z. A.; Siegler, M. A.; McQueen, T. M. *Inorg. Chem.* **2014**, *53*, 4500–4507.
- [39] Miao, M.; Seshadri, R. *J. Phys.: Condens. Matter* **2012**, *24*, 215503.

4 Synthesis and Electrocatalytic Properties of $[\text{IrO}_2]^{x-}$ Nanosheets

Daniel Weber, Leslie M. Schoop, Daniel Wurmbrand, Viola Duppel, Bettina V. Lotsch

Manuscript in preparation.

Abstract

Iridium oxide based electrocatalysts show unrivaled stability and activity in highly aggressive media. Thus far, most efforts to reduce the required amount of this costly element by nanostructuring were restricted to the synthesis of nanoparticles with either rutile-type IrO_2 or amorphous IrO_x . Here, we report the synthesis and structural characterization of $[\text{IrO}_2]^{x-}$ nanosheets as well as their potential application as an electrocatalyst for water oxidation. The nanosheets are synthesized from the layered compound $\text{K}_{0.75}\text{Na}_{0.25}\text{IrO}_2$ by exchanging the alkaline ions for protons and then neutralizing the solid acid with TBAOH. TEM studies reveal that the nanosheets adopt a CdI_2 -type structure. With AFM, their lateral sizes were shown to range from $0.5\ \mu\text{m}$ to $7\ \mu\text{m}$, while the height is $1.02(8)\ \text{nm}$. Initial electrochemical investigations of these $[\text{IrO}_2]^{x-}$ nanosheets deposited on titanium

anodes show that the nanosheets outperform bulk IrO_2 in the electrocatalytic water oxidation reaction. The overpotential of the $[\text{IrO}_2]^{x-}$ nanosheets at a current density of 10 mA cm^{-2} is $344(7) \text{ mV}$ and the Tafel slope is 58 mV dec^{-1} . Not only do these findings add iridium oxide layers to the library of available electrocatalysts, but they also show that exfoliation is a useful means to increase the electrocatalytic activity.

4.1 Introduction

Splitting water into hydrogen and oxygen is of immense technological interest to realize a clean and renewable source of energy as an alternative to fossil fuels.¹ Even though the generation of hydrogen is the main goal, the oxygen evolution reaction (OER) is the bottleneck in this process.^{2,3} Due to the number of complex intermediates and the need to transfer four electrons instead of two in a concerted fashion as well as the slower kinetics, a higher overpotential is needed to drive the oxidation of water. Apart from these criteria, OER catalysts also have to be cheap to manufacture, stable over time and chemically resistant to environments of high and/or low pH value.⁴

Due to these stringent requirements, only a few good OER catalysts are known today. Examples are binary oxides with the rutile structure (RuO_2 , IrO_2), spinels (Co_3O_4 , NiCo_2O_4 , NiLa_2O_4), perovskites (SrLaO_3 , MnLaO_3 , CoLaO_3 , CuLaO_3), pyrochlores ($\text{Pb}_2\text{Ru}(\text{Ir})_2\text{O}_7$) and layered double hydroxides (LDH, $\text{Ni}_{1/3}\text{Co}_{2/3}(\text{OH})_2\text{Br}_{1/3} \cdot 0.5 \text{H}_2\text{O}$, $\text{Ni}_{3/4}\text{Fe}_{1/4}(\text{OH})_2(\text{CO}_3)_{1/8} \cdot 0.8 \text{H}_2\text{O}$).⁵⁻⁹ Even though ruthenium and iridium have a low elemental natural abundance, which makes them expensive resources, RuO_2 and IrO_2 stand out regarding their OER activity among binary and ternary systems due to their low overpotentials, long term stability as well as chemical resistance to various pH values and to acid conditions in particular.¹⁰

To further improve their activity in heterogeneous catalysis, three main strategies are applied: doping, facet engineering and nanostructuring. One example for a doped material is the OER catalyst $\text{Ba}_{0.5}\text{Sr}_{0.5}\text{Co}_{0.8}\text{Fe}_{0.2}\text{O}_{3-\delta}$, which derives from the perovskite structure of the generalized formula $\text{A}_{1-x}\text{A}'_x\text{B}_{1-y}\text{B}'_y\text{O}_{3\pm\delta}$, with A and A' being La, Ca, Sr or Ba, and B or B' being transition metals such as Cr, Mn, Fe, Co, Ni and Cu.¹¹ By adjusting the metal species and ratio, the filling of the *eg* molecular orbitals was optimized, leading to Tafel slopes comparable to IrO_2 under alkaline conditions. The second strategy, facet

engineering, aims to expose specific, highly active facets at the interface. One recent study on films of IrO_2 established that the (100) facet has a higher OER activity than the thermodynamically more stable (110) facet.¹² The third strategy is nanostructuring of the catalyst and thereby increasing the available number of coordinatively undersaturated metal sites per mass unit or the active sites, thus countering the disadvantage of the low natural abundance of Ru and Ir and leading to a higher activity per mass unit.

The most heavily investigated nanoscopic oxide systems are nanoparticles, either formed by oxidation of metal nanoparticles¹³ or by hydrolysis of the metal salts, and usually have sizes in the range of several nanometers.^{14,15} Yet, two-dimensional (2D) nanostructures such as mono- or few-layered nanosheets synthesized by exfoliating lamellar compounds started to draw interest for catalytic applications.^{8,16–19} The most prominent example is exfoliated 1T-MoS₂ for hydrogen evolution.¹⁶ There, the metallic surface was found to be the catalytic site with a Tafel slope of 40 mV dec⁻¹, unlike in bulk 2H-MoS₂ where the active sites reside at the edges and show a much higher Tafel slope of 80 mV dec⁻¹. There are only two examples of electrocatalytic nanosheet systems to date for OER, which are the exfoliated Ti₃C₂ MXene²⁰ and Ni_{3/4}Fe_{1/4}(OH)₂(CO₃)_{1/8} · 0.8 H₂O LDH phase (NiFe-LDH)^{8,19}, both investigated under high pH conditions. In the NiFe-LDH example, the exfoliated layers feature a drastic decrease in the overpotential from 342 mV in the bulk to 302 mV in the exfoliated nanosheet. Hence, the exfoliation of layered compounds into single or few layers seems to be a promising technique to increase a catalyst's activity per mass unit, but was limited to alkaline pHs due to the instability of LDHs in acidic environments.

Here, we present the preparation of $[\text{IrO}_2]^{x-}$ nanosheets and the investigation of their electrochemical properties for OER. The nanosheets of $[\text{IrO}_2]^{x-}$ represent a new mono-layered compound with a composition distinct from previously reported iridium oxides. In addition to structural investigation, we show that the nanosheets can act as an active

component on titanium anodes. Here, these act as an OER electrocatalyst which is able to operate under highly acidic conditions, a pH regime where most OER catalysts are unstable.¹⁰ The effect of nanostructuring by exfoliation on electrocatalysis is explored by comparing the performance of the nanosheet electrode to those of bulk iridium compounds.

4.2 Results and Discussions

4.2.1 Preparation of IrOOH from $K_{0.75}Na_{0.25}IrO_2$

Synthesis of $K_{0.75}Na_{0.25}IrO_2$ In a modified synthesis procedure, $K_{0.75}Na_{0.25}IrO_2$ was synthesized at elevated temperatures and in a shorter time compared to the report in chapter 3. The increased temperature of 900 °C was necessary for subsequent exfoliation, as the previously reported product synthesized at 850 °C could not be converted into nanosheets. A possible explanation for this observation is the increased number of defects at elevated temperature. This might lead to more breaking points and thus a higher probability for intercalation and subsequent exfoliation. At the elevated temperature, the reactant mixture has a noticeable vapor pressure, which leads to crystallization of the product at the upper wall of the crucible and slow evaporative loss of the product. Thus, the reaction time was optimized to 15 h to limit evaporation. The modified reaction procedure leads to the presence of the side phases KIr_4O_8 , visible in the PXRD pattern displayed in Figure 4.1.

IrOOH Soaking $K_{0.75}Na_{0.25}IrO_2$ in HCl for five days with a daily exchange of the acid results in IrOOH as seen in chapter 3. Under the optical microscope, the color as well as morphology are unchanged by the acid treatment.

Figure 4.2 shows the results of diffraction experiments on the IrOOH powder. Both

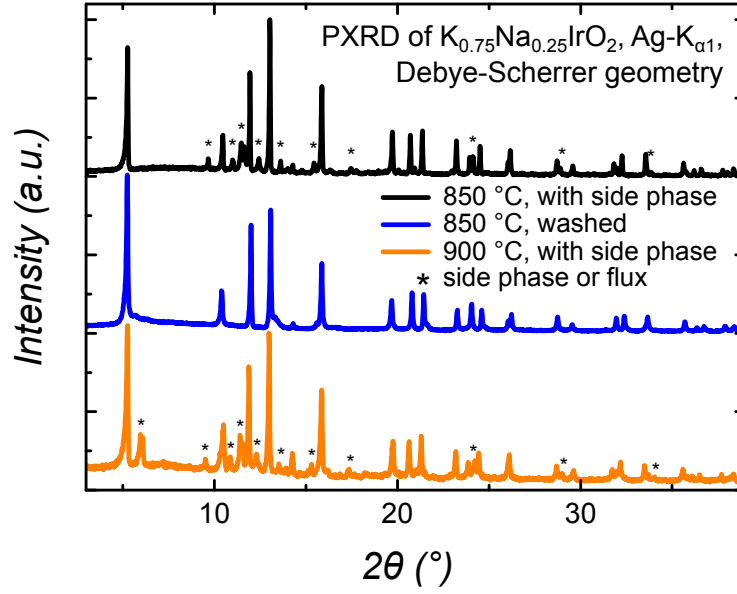


Figure 4.1: PXRD patterns of $\text{K}_{0.75}\text{Na}_{0.25}\text{IrO}_2$ synthesized at 850 °C (black) and after purification by washing with MeOH (blue), as well as $\text{K}_{0.75}\text{Na}_{0.25}\text{IrO}_2$ prepared at 900 °C (orange), asterisks the reflections of the side phase.

$\text{K}_{0.75}\text{Na}_{0.25}\text{IrO}_2$ and IrOOH crystallize in the $P\bar{3}m1$ space group. As a consequence of the ion exchange reaction, the c lattice parameter shortens from $c = 6.254(4)$ Å in $\text{K}_{0.75}\text{Na}_{0.25}\text{IrO}_2$ to $c = 4.6396(3)$ Å in IrOOH , while the a and b axis stay approximately the same. Thus, the PXRD pattern of IrOOH shows a shift of all reflections with $(00l)$ component due to the change of the c -lattice parameter, while the reflections with $(hk0)$ components remain at the same position. Figure 4.2 also depicts a TEM bright field image of IrOOH microcrystals as well as the SAED pattern and its simulation based on the crystallographic data of IrOOH . From the SAED pattern, the d -values $d_{(010)} = 2.71$ Å, $d_{(110)} = 1.56$ Å, $d_{(020)} = 1.35$ Å, $d_{(210)} = 1.02$ Å as well as $d_{(030)} = 0.90$ Å were extracted and indexed according to the SAED simulation. Therefore, TEM-SAED indicates that the in-plane structural motif was retained during the ion exchange, confirming the results of the Rietveld refinement in chapter 3.

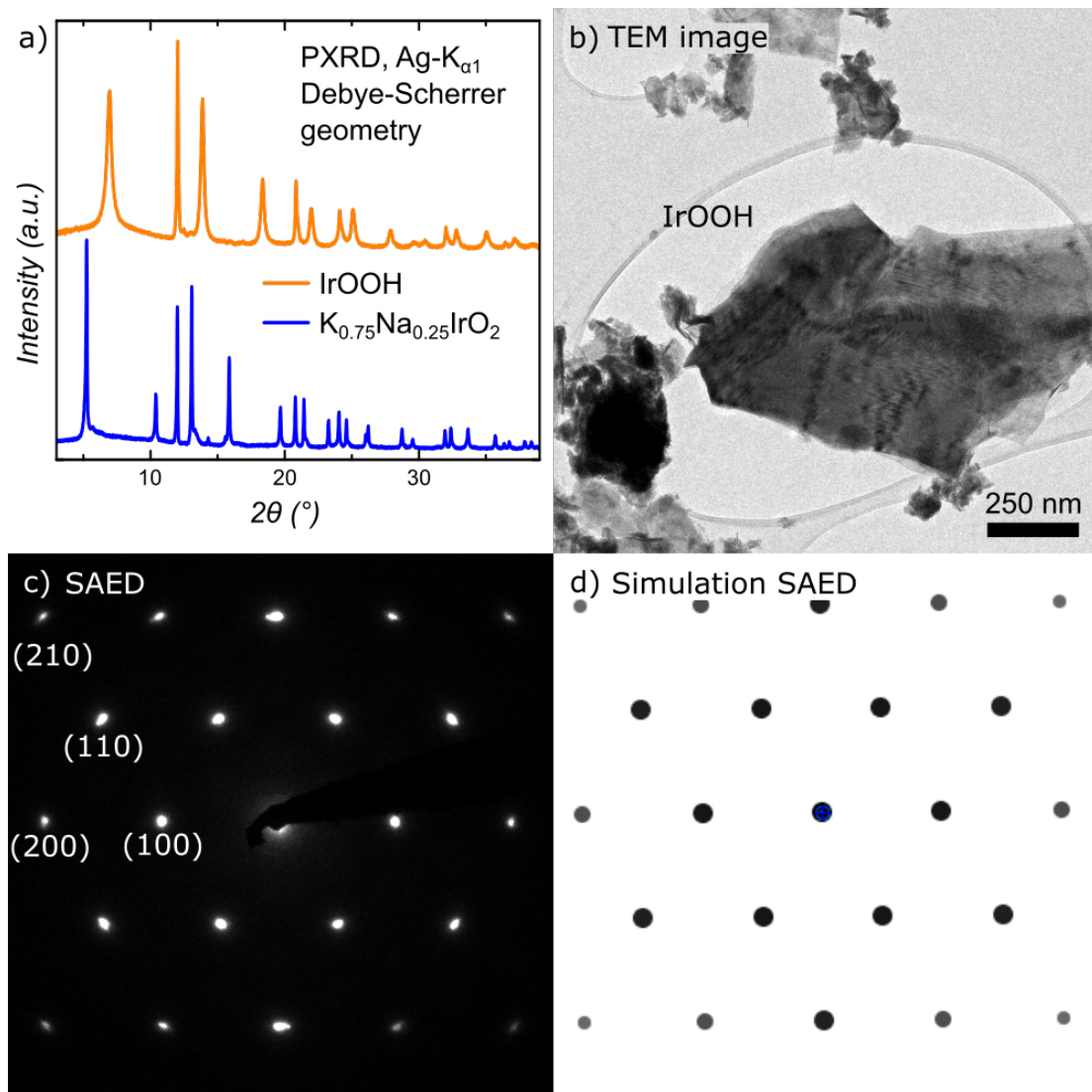


Figure 4.2: a) PXRD pattern of IrOOH compared to K $_{0.75}$ Na $_{0.25}$ IrO $_2$, b) TEM bright field image and c) SAED diffraction pattern with (hkl) indices of IrOOH, d) simulated SAED pattern based on crystallographic data of IrOOH in the space group $P\bar{3}m1$ along [001] zone axis.

4.2.2 Synthesis and structure of $[\text{IrO}_2]^{x-}$ nanosheets

Nanosheet preparation IrOOH was exfoliated by neutralizing the interlayer protons with TBAOH, which resulted in a dark blue aqueous dispersion of $[\text{IrO}_2]^{x-}$ nanosheets with TBA^+ as counterions. The zeta-potential of the dispersion is - 36.4 mV, indicating that the nanosheets are negatively charged. In combination with the elemental composition of the nanosheets determined by TEM-EDX of Ir:O = 1:2, this indicates that a significant portion of the iridium ions is trivalent according to the sum formula $[\text{Ir}_x^{3+}\text{Ir}_{1-x}^{4+}\text{O}_2]^{x-}$. The $[\text{IrO}_2]^{x-}$ nanosheets were investigated by AFM on Si substrates with a thermally grown SiO_2 layer of 270 nm and by TEM on a lacey carbon grid. To establish the height of a single nanosheet, the dispersion was diluted to optimize the surface coverage and dropped on a SiO_2 -Si substrate. The nanosheets could be identified by optical microscopy due to their interference contrast.^{21,22} The height of a $[\text{IrO}_2]^{x-}$ monolayer was determined with AFM and is found to be 1.02(8) nm. The result is an average of the height measurements of 35 edges. To exclude measurement artifacts by the change of chemical potential while crossing from the substrate to the $[\text{IrO}_2]^{x-}$ monolayers, the height of a single layer was detected by measuring single layers stacked on other $[\text{IrO}_2]^{x-}$ nanosheets. Nanosheets directly on the substrate were found to be 1.3(2) nm high. Exemplary optical microscope and AFM images are shown in Figure 4.3.

The detected height of 1.02(8) nm for a single monolayer is higher than the height of 0.5 nm which is expected for a single slab in the crystalline bulk material. Yet, the height value is similar to the height of chemically exfoliated MoS_2 ²³ or $[\text{RuCl}_3]^{x-}$ which are 1.0 - 1.2 nm high respectively, as seen in section 2.2.2. This indicates that a layer of water was trapped between the nanosheet and the underlying support, which has a height of 0.3 nm per monolayer of water.²⁴ As IrOOH does not incorporate water in its bulk form, the AFM data suggests that the exfoliation into monolayers changed the hydration

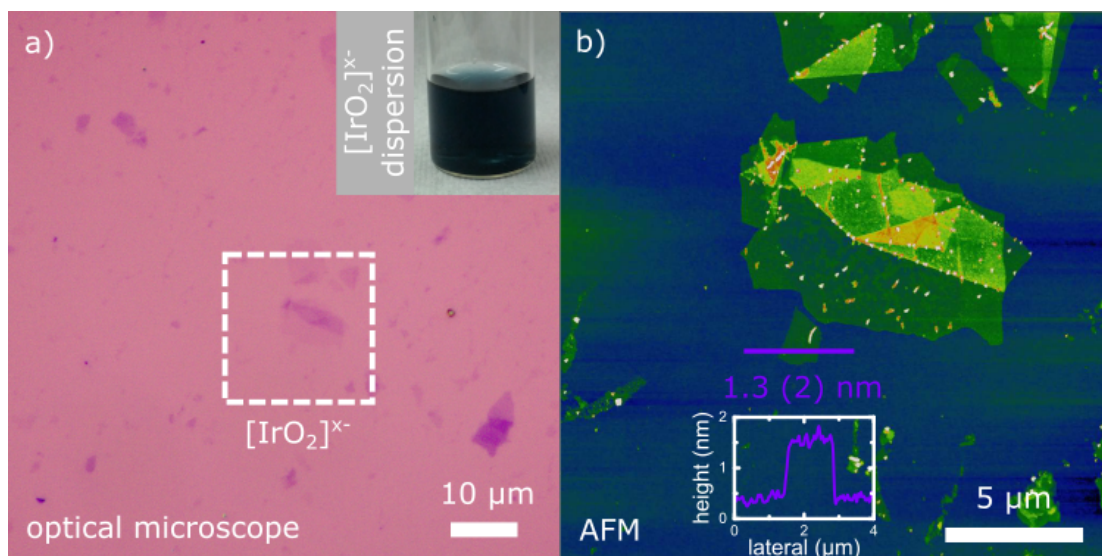
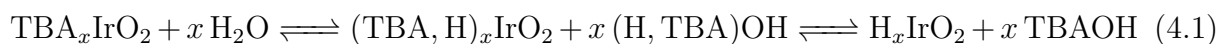


Figure 4.3: a) Optical microscope and b) AFM image of [IrO₂]^{x-} nanosheets, inset in a) shows blue aqueous dispersion of [IrO₂]^{x-} nanosheets, inset in b) displays an exemplary height profile with average height value of a [IrO₂]^{x-} single layer measured on a SiO₂(270 nm)-Si substrate.

behavior of the compound. Similar changes in hydration behavior have been observed in phosphatoantimonic acid H₃Sb₃P₂O₁₄ and its salts, where hydration depending on the relative humidity goes from a stepwise water intake in K₃Sb₃P₂O₁₄ to a continuous uptake in the nanosheet stack.²⁵

The presence of large amounts of TBA⁺ ions between [IrO₂]^{x-} nanosheets was excluded for nanosheets deposited from the dilute dispersion, as the size of the TBA⁺ cation would increase the height by 1 nm²⁶ to a total of 1.5 nm when combined with the [IrO₂]^{x-} slab, a value not observed in this set of experiments. The exchange of TBA⁺ for protons is a known effect of the dilution of the nanosheet dispersion, which influences the composition of the electrical double layer surrounding the nanosheet²⁷ according to the equilibrium between TBAOH and H₂O described by the following reaction equation 4.1:



To check whether the degree of dilution influenced the incorporation of TBA^+ cations, wafers with nanosheets deposited from an undiluted dispersion were characterized by AFM. The height was 1.60(8) nm measured on nanosheets folded onto themselves, which fits to the combined height of the 0.5 nm for the single layer slab and the height of 1 nm added by the presence of TBA^+ . Exemplary AFM images of nanosheets deposited from an undiluted dispersion are displayed in Figure C.1. Therefore, the height of nanosheets without TBA^+ is 1.02(8) nm, while the incorporation of TBA^+ leads to a height of 1.60(8) nm.

In-plane structure of nanosheets To check whether a structural change occurred during exfoliation, the $[\text{IrO}_2]^{x-}$ nanosheets were analyzed by TEM. Figure 4.4 a) shows several translucent nanosheets on a lacey carbon support. The translucence towards the electron beam is typical for very thin samples and indicates that the specimen consists of one or a few layers. TEM-EDX measurements showed that the ratio of iridium to oxygen was $\text{Ir} : \text{O} = 1 : 2.3$ measured on the Ir M-line and O K-line. Considering the overestimation of light elements such as oxygen by EDX detectors, the ratio is close to the ideal stoichiometry of $[\text{IrO}_2]^{x-}$ nanosheets. Figure 4.4 b) displays the hexagonal in-plane

Table 4.1: Comparison of d -values from TEM of a $[\text{IrO}_2]^{x-}$ single layer, TEM of IrOOH microcrystals, PXRD and single crystal X-ray diffraction of $\text{K}_{0.75}\text{Na}_{0.25}\text{IrO}_2$.

(hkl)	d -values TEM $[\text{IrO}_2]^{x-}$ [nm]	d -values TEM IrOOH [nm]	d -values PXRD IrOOH [nm]	d -values SXRD $\text{K}_{0.75}\text{Na}_{0.25}\text{IrO}_2$ [nm]
(010)	0.267	0.271	0.270	0.272
(110)	0.154	0.156	0.156	0.157
(020)	0.134	0.135	0.135	0.136
(210)	0.101	0.102	0.102	0.103
(030)	0.089	0.090	0.090	0.091

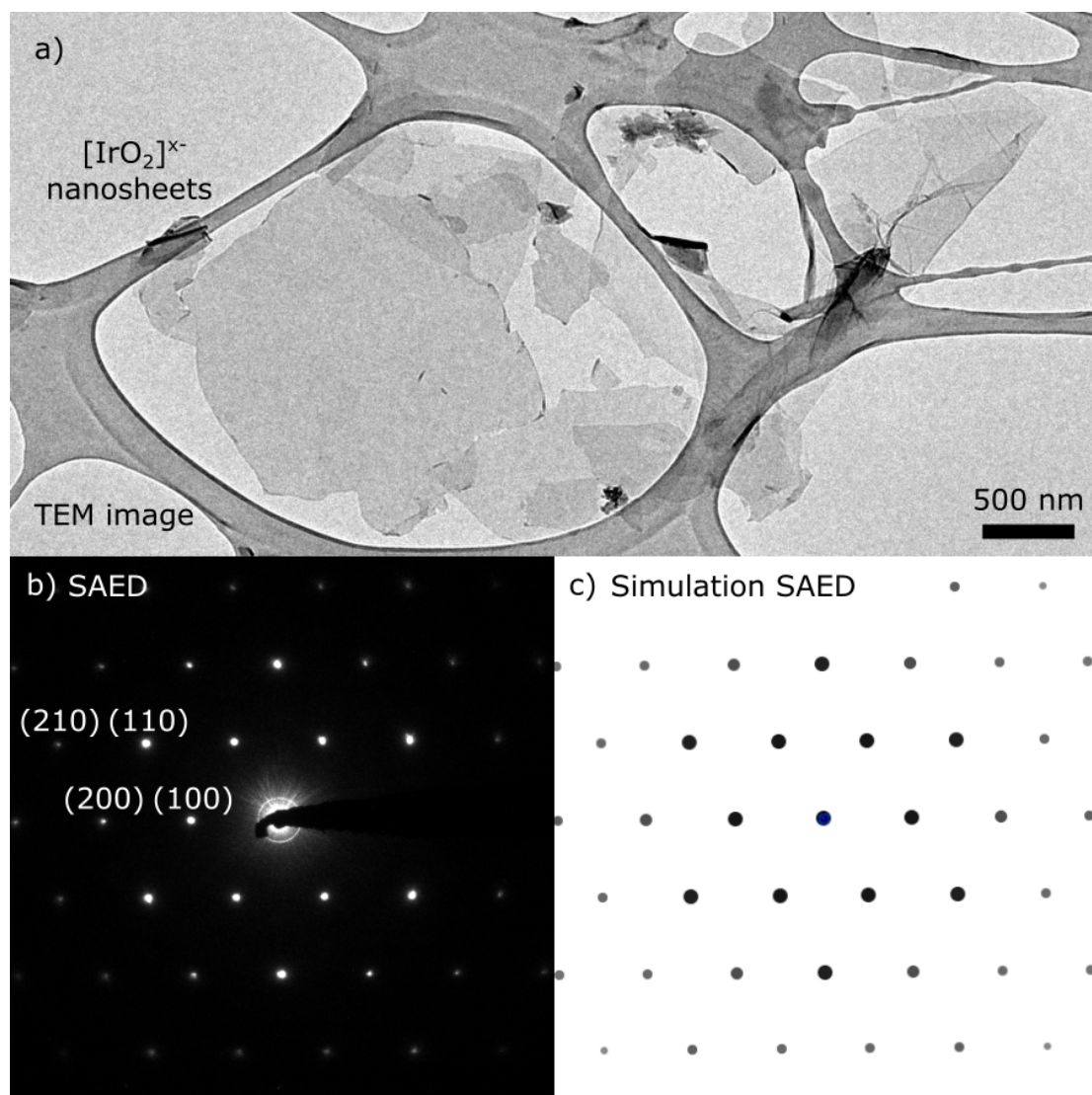


Figure 4.4: a) TEM image and b) SAED pattern of $[\text{IrO}_2]^{x-}$ nanosheets, c) simulated SAED pattern based on crystallographic data from IrOOH in space group $P\bar{3}m1$ along $[001]$ zone axis.

SAED pattern of the layers of $[\text{IrO}_2]^{x-}$. The reflections have d -values of 2.67 Å, 1.54 Å, 1.34 Å, 1.01 Å as well as 0.089 Å and were assigned to (hkl) values by simulating the single layer based on the crystallographic data from IrOOH in chapter 3 along the $[001]$ zone axis. The d -values of $[\text{IrO}_2]^{x-}$ nanosheets from TEM are compared to the data of IrOOH and $\text{K}_{0.75}\text{Na}_{0.25}\text{IrO}_2$ in table 4.1. The results from the SAED measurements of the nanosheets only slightly deviate from the values obtained from TEM and x-ray diffraction of the bulk compounds. As the deviations are well within the margin of error of electron diffraction ($\approx 5\%$) and TEM-EDX suggests a composition close to the formula IrO_2 , these indicate the retention of the in-plane CdI_2 structural motif in the $[\text{IrO}_2]^{x-}$ layers during the exfoliation process. Consequently, the nanosheets consist of layers of triangular, edge sharing IrO_6 octahedra, similar to the nanosheets of $[\text{MnO}_2]^{x-}$, $[\text{CoO}_2]^{x-}$, and $[\text{RuO}_2]^{x-}$.^{28–30}

4.2.3 Electrochemical characterization of $[\text{IrO}_2]^{x-}$ nanosheets

Electrodes of $[\text{IrO}_2]^{x-}$ nanosheets on Ti As electrodes consisting of titanium plates covered with catalyst are a standard setup for industrial applications^{31,32}, the $[\text{IrO}_2]^{x-}$ nanosheets were applied to titanium plates to investigate their electrochemical properties. This kind of setup is called a dimensionally stable anode (DSA). To remove the layer of TiO_2 naturally covering titanium and thus improve the reproducibility of the electrochemical measurements, the substrates were heated in a solution of 10 wt% oxalic acid to etch the surface oxide.³³ Figure 4.5 shows SEM images of the $\text{H}_2\text{C}_2\text{O}_4$ -treated Ti-surface.

The polycrystalline nature of the Ti substrate is emphasized, as crystallites with clear facets and edges stick out of the surface. The rippled surface structure of the Ti substrate visible in the highly magnified image in Figure 4.5 b) could result from a thin oxide layer, which is unavoidable when handling titanium in air. BSE detection shows that the Ti-substrates have a homogeneous composition.

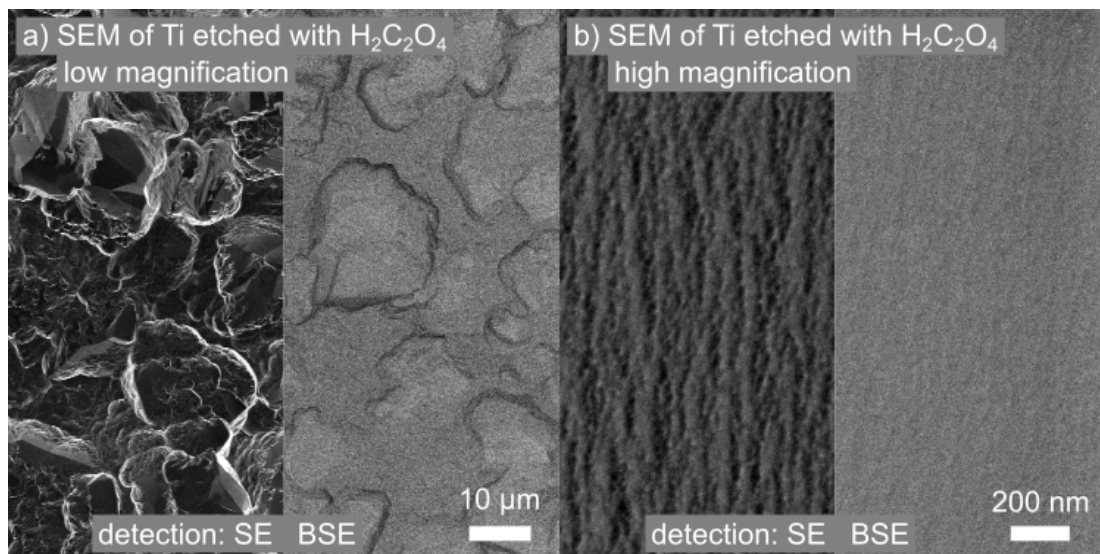


Figure 4.5: SEM images of $\text{H}_2\text{C}_2\text{O}_4$ -etched Ti substrates with low (a) and high (b) magnification, imaged with SE (left) and BSE (right) detection.

The $[\text{IrO}_2]^{x-}$ nanosheets were deposited at various temperatures between 120 $^\circ\text{C}$ and 300 $^\circ\text{C}$ by dropping the undiluted dispersion onto the hot Ti platelet, letting the water evaporate and annealing the platelets for another 20 min. As shown by the exemplary SEM images in Figure 4.6, the nanosheets covered the entire surface of the substrate and were distinguishable from titanium by using the BSE detector.

The thermal decomposition of $\text{TBA}_x\text{IrO}_2 \cdot y\text{H}_2\text{O}$ was investigated by DTA-TG to optimize the deposition temperature of $[\text{IrO}_2]^{x-}$ nanosheets. The result is displayed in Figure C.2 of the appendix. The temperatures of $T_1 = 144$ $^\circ\text{C}$ and $T_2 = 257$ $^\circ\text{C}$ were identified as critical for the nanosheet deposition. At $T_1 = 144$ $^\circ\text{C}$, the interlayer hydrate layer is ejected, and at $T_2 = 257$ $^\circ\text{C}$ the organic counterion TBA^+ starts to decompose. Therefore, the $[\text{IrO}_2]^{x-}$ dispersion was applied to Ti platelets at temperatures of below the dehydration temperature ($T = 120$ $^\circ\text{C}$ and $T = 140$ $^\circ\text{C}$), below the decomposition temperature of TBA^+ ($T = 180$ $^\circ\text{C}$ and $T = 200$ $^\circ\text{C}$) and well above the TBA^+ decomposition temperature ($T = 300$ $^\circ\text{C}$). The effect of the different temperature regimes was investigated by SEM, with the results displayed in Figure 4.7. Below $T = 257$ $^\circ\text{C}$, the deposition produces a

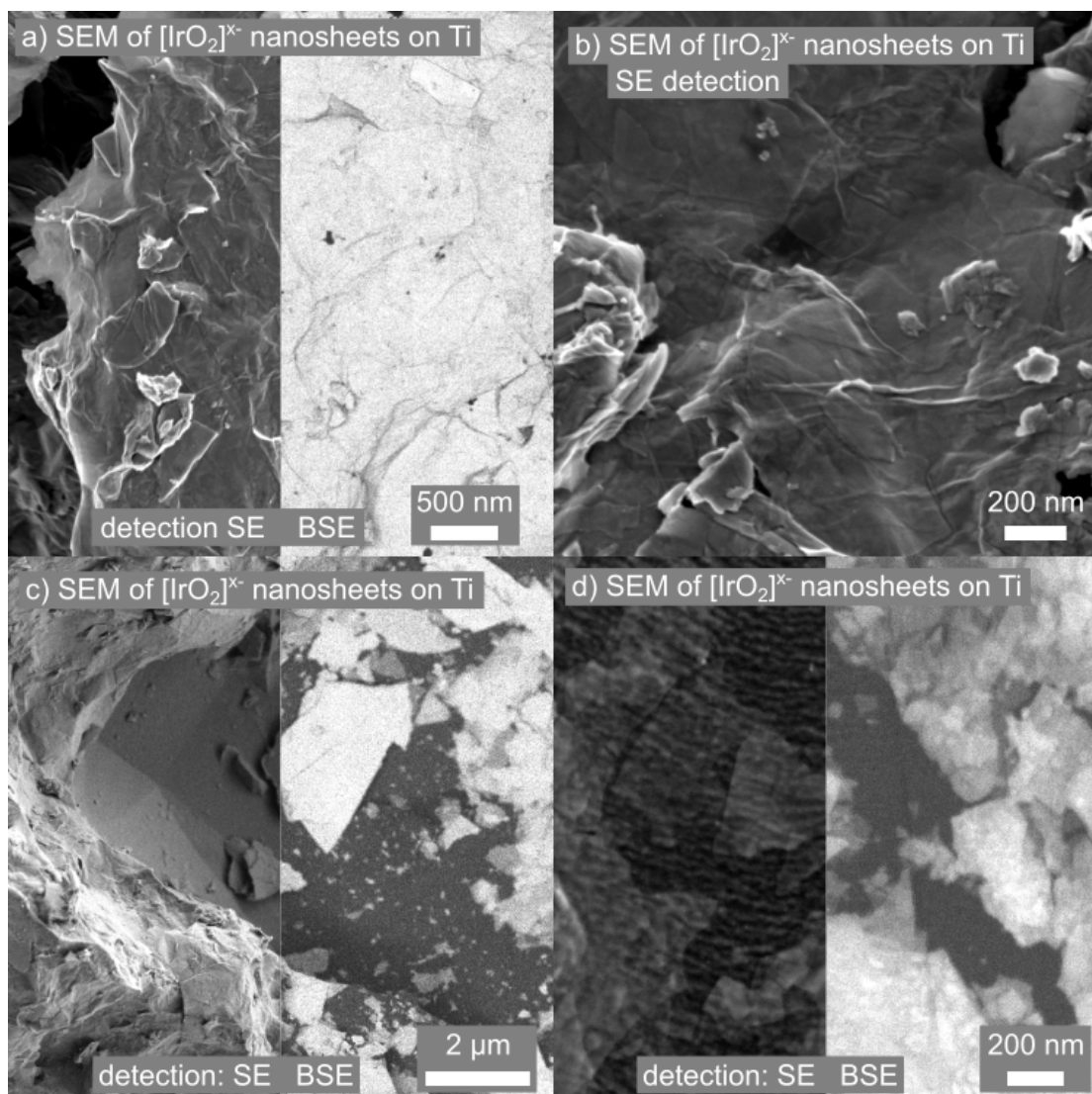


Figure 4.6: SEM images of $[\text{IrO}_2]^{x-}$ nanosheets on etched Ti substrate, deposition at 160°C.

homogenous film. The dehydration occurring at $T = 144^\circ\text{C}$ does not damage the $[\text{IrO}_2]^{x-}$ nanosheets. Above $T = 257^\circ\text{C}$, the film starts to crack as the decomposition products are ejected. Yet the thermal energy does not damage the $[\text{IrO}_2]^{x-}$ film by detaching it from the Ti surface or by reconstructing the layered motif of the 2D material.

The coverage was estimated to be greater than 95 % of the substrate surface, as only very few spots of different composition were found by BSE. At areas of low coverage, such as those depicted in Figure 4.6 c) and d), the nanosheets closely followed the rippled

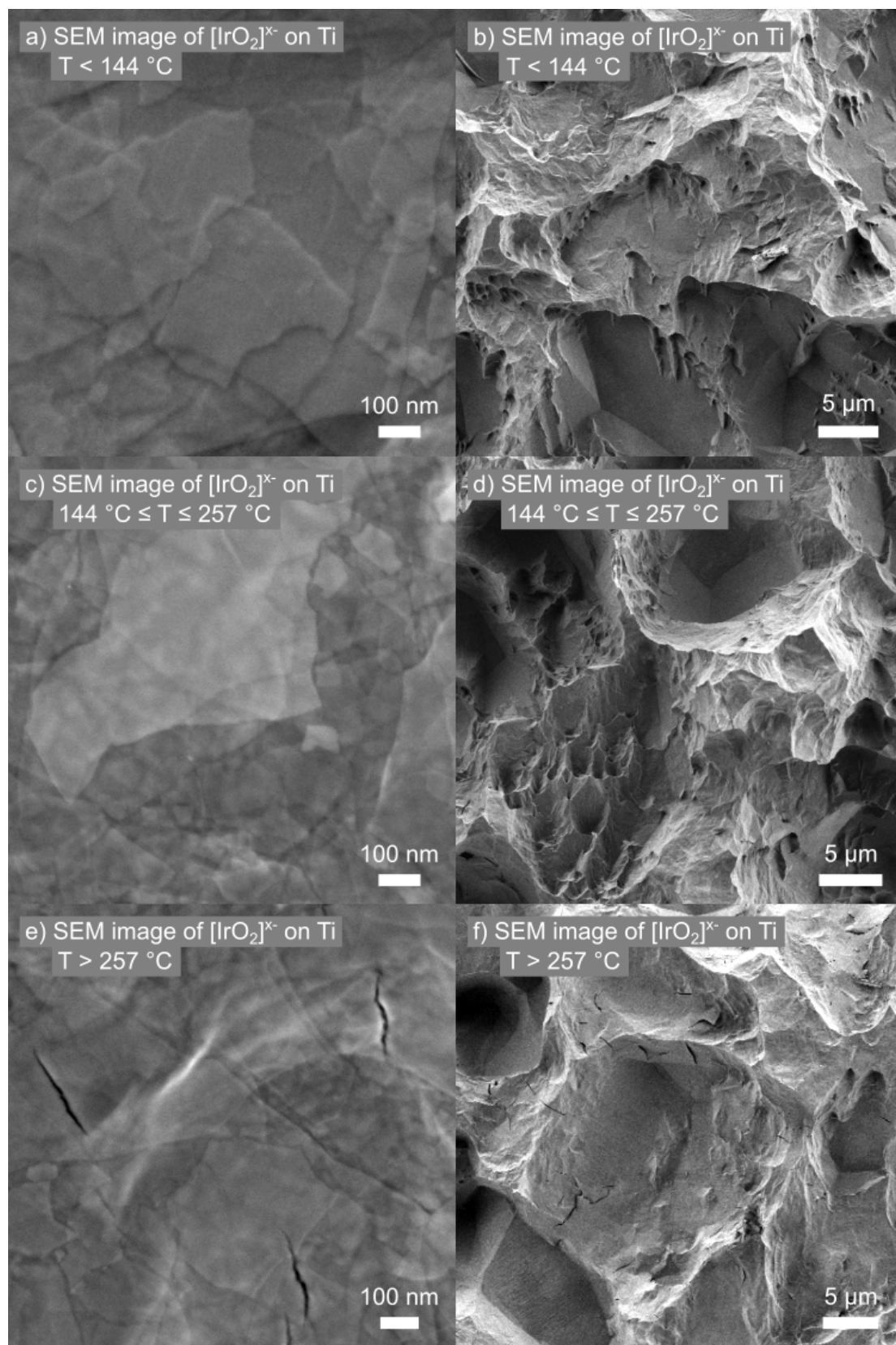


Figure 4.7: SEM images of $[\text{IrO}_2]^{x-}$ nanosheets applied in different temperature regimes on Ti substrate.

surface structure of the Ti substrate observed in Figure 4.5 b). With increasing nanosheet film thickness, the film becomes smoother, which suggests that at least several layers lie between the Ti substrate and the $[\text{IrO}_2]^{x-}$ -air interface.

Electrochemical characterization of $[\text{IrO}_2]^{x-}$ nanosheets on Ti The electrocatalytic properties of $[\text{IrO}_2]^{x-}$ nanosheets on Ti were investigated by collecting current-voltage curves in a 0.1 M perchloric acid electrolyte with a Ag/AgCl/saturated KCl reference electrode on five electrodes for each compound. The data was fitted to the Tafel equation (eq. 4.2).

$$\eta = b \log \frac{j}{j_0} = b \log j + b \log j_0 \quad (4.2)$$

where η is the overpotential, b the Tafel slope, j the current density, and j_0 the exchange current density. The data was corrected by subtraction of the open circuit potential of a Pt/Pt electrode couple and applying a correction for the internal resistance, thereby excluding the effect of variations of the pH. The plots of the collected data are displayed in Figure 4.8.

The Tafel slope was used as the first indicator for electrochemical activity, as it allows to estimate how efficiently the electrode converts the applied potential into charge carriers used in the electrochemical reaction. The values were extracted by fitting the Tafel equation to the linear region of the plot of η vs $\log j$. Bulk IrO_2 and IrOOH have a Tafel slope of 70(2) mV dec⁻¹ and 79(3) mV dec⁻¹ respectively, while electrodes modified with $[\text{IrO}_2]^{x-}$ nanosheets feature a slope of only 58(3) mV dec⁻¹. This is a reduction of 12 mV dec⁻¹ compared to bulk IrO_2 and of 21 mV dec⁻¹ compared to bulk IrOOH . The Tafel slope also depends on the rate determining step of the surface reaction. The Tafel slope also allows to identify the rate determining step of the OER, but is very dependent on the catalyst, pH, electrode setup and electrolyte. In bulk IrO_2 electrocatalysts investigated under acidic

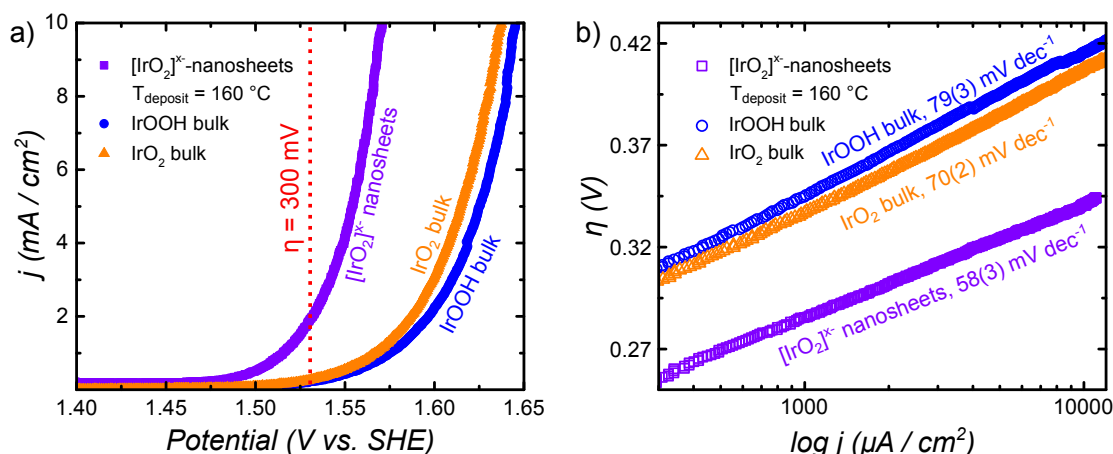


Figure 4.8: Plot of a) the current density j against the potential with the red dotted line as a visual cue for the readout of j at $\eta = 0.3 \text{ V}$ and b) the overpotential η against the logarithmic representation of the current density j , scan rate was 5 mV sec^{-1} and Ag/AgCl/saturated KCl as a reference electrode.

conditions, the restructuring process between two energetically inequivalent bound surface hydroxyl groups has been associated with a Tafel slope of approximately 60 mV dec^{-1} .^{34,35} While this might be a first hint towards the rate determining step in bulk IrOOH and the $[\text{IrO}_2]^{x-}$ nanosheets, careful systematic investigations are needed to elucidate the surface chemistry of bulk IrOOH and the $[\text{IrO}_2]^{x-}$ nanosheets.

The overpotential η is the potential needed beyond the intrinsic potential of 1.23 V to overcome kinetic barriers for the water oxidation reaction and was calculated for a current density of $j = 10 \text{ mA cm}^{-2}$ utilizing the Tafel equation. The current density of $j = 10 \text{ mA cm}^{-2}$ mimics the output of a high end solar to hydrogen device with 12 % efficiency.⁸ The overpotential of $[\text{IrO}_2]^{x-}$ nanosheets at $j = 10 \text{ mA cm}^{-2}$ was $344(7) \text{ mV}$, while the bulk compounds IrO₂ and IrOOH had an overpotential of $\eta_{10 \text{ mA cm}^{-2}} = 415(5) \text{ mV}$ and $\eta_{10 \text{ mA cm}^{-2}} = 433(5) \text{ mV}$, respectively. Therefore, the exfoliation resulted in a significant reduction of the overpotential of the $[\text{IrO}_2]^{x-}$ nanosheets.

A third indicator used to compare the performance of electrocatalysts is the current density j measured at an overpotential of 300 mV . Bulk IrO₂ and IrOOH have relatively

Table 4.2: Comparison of b , η and, j of the electrodes of bulk IrO_2 , bulk IrOOH , and $[\text{IrO}_2]^{x-}$ nanosheets.

electrode	Tafel slope b	η at	j at
344 material		10 mA cm^{-2}	at $\rho = 300 \text{ mV}$
	$[\text{mV dec}^{-1}]$	$[\text{mV}]$	$[\text{mA cm}^{-2}]$
$[\text{IrO}_2]^{x-}$	58(3)	344(7)	1.8(4)
IrOOH	79(3)	433(5)	0.172(15)
IrO_2	70(2)	415(5)	0.217(7)

low current densities of $j_{300\text{mV}} = 0.217(7) \text{ mA cm}^{-2}$ and $j_{300\text{mV}} = 0.172(15) \text{ mA cm}^{-2}$, respectively, while the current density of the electrodes of $[\text{IrO}_2]^{x-}$ nanosheets at $\eta = 300 \text{ mV}$ was approximately one order of magnitude larger with $j_{300\text{mV}} = 1.8(4) \text{ mA cm}^{-2}$.

As can be seen in all three electrocatalytic indicators in table 4.2, the exfoliation results in an increased activity compared to the bulk compounds. In general, the activity depends on the loading, concentration and nature of the electrolyte, the valency of the highest and lowest iridium oxidation state³⁶ and the effective active area. The loading was 0.2 mg cm^{-2} for all samples and all experiments shown here were conducted in 0.1 M perchloric acid, thus excluding the loading and electrolyte as critical factors. As the structure of the $[\text{IrO}_2]^{x-}$ nanosheets did not change significantly, the valency of most of the iridium ions is probably close to that of IrOOH , as a significant change in valency would lead to a reconstructive phase transition and hence to notable changes in the crystal structure. Yet, as the tetravalent state is in general favorable to the iridium ion, it cannot be excluded that some fraction of iridium converted to the tetravalent state, similar to the nanosheets of $[\text{MnO}_2]^{x-}$.²⁸ At this point, it cannot be estimated whether the valency of iridium is a critical or even beneficial parameter for the reaction under study. X-ray photoemission spectroscopy experiments are in progress to verify the average oxidation state of iridium covering the electrodes. The last parameter for electrocatalysts is the active surface area.

In IrO_x nanoparticles, a decrease in the average diameter from 75 nm to 2 nm leads to an enhancement of the electrocatalytic activity.^{15,37} A similar trend has been observed in LDHs, where exfoliation also yields an increased activity. Therefore, the data suggests that the effective area is a critical parameter which is influenced by exfoliation.

To establish whether the nanosheets of $[\text{IrO}_2]^{x-}$ are also competitive with other iridium oxide based OER catalysts, data on the Tafel slopes and overpotentials in the acidic pH regime were extracted from the literature, adjusted to $j = 10 \text{ mA cm}^{-2}$ where applicable and listed with a short remark on the experimental conditions in table 4.3. The tabulated data highlight how the overpotential and Tafel slope vary depending on the measurement regime of the current density j and pH, the utilized electrode setup, sort of electrolyte used as well as the lowest and highest oxidation state in the iridium species.³⁶ In a qualitative assessment, $[\text{IrO}_2]^{x-}$ nanosheet electrodes are able to compete with and outperform some IrO_x OER catalysts under acidic conditions. Yet, a quantitative evaluation based on the tabulated data is challenging due to the widely varying reaction and measurement conditions, thus emphasizing the need for experiments for a direct comparison under the same measurement conditions.

Another direction for further investigations lies in measurements at high pH values to directly compare the new $[\text{IrO}_2]^{x-}$ nanosheets to other OER catalysts such as NiFe-LDH¹⁹ or perovskites.^{10,11} Table 4.3 also emphasizes how the Tafel slope and overpotential varies with the pH for IrO_2 itself. As a change of compound adds another parameter to the experiment, the direct comparison necessitates a careful systematic study.

4.3 Conclusion

We report a procedure for the exfoliation of IrOOH into an aqueous dispersion of $[\text{IrO}_2]^{x-}$ nanosheets. TEM investigations show that the single layers retain the triangular lattice

Table 4.3: Comparison of η of $[\text{IrO}_2^{x-}]$ nanosheet electrode to values reported in the recent literature or calculated (*) from literature data to fit $j_0 = 10 \text{ mA cm}^{-2}$.

electrode material	b [mV dec ⁻¹]	η [V] @ 10 mA cm ⁻²	conditions, reference
$[\text{IrO}_2]^{x-}$ nanosheets	58(3)	0.344(7)	0.2 mg cm ⁻² loading on Ti, measured at pH = 1 in HClO ₄ 0.1 M, this work
IrOOH, bulk	79(3)	0.433(5)	0.2 mg cm ⁻² loading on Ti, measured at pH = 1 in HClO ₄ 0.1 M, this work
IrO ₂ , bulk	70(2)	0.415(5)	0.2 mg cm ⁻² loading on Ti, measured at pH = 1 in HClO ₄ 0.1 M, this work
KIr ₄ O ₈ , bulk	65	0.350	0.2 mg cm ⁻² loading on Ti, pH = 1 in HClO ₄ 0.1 M ³⁸
IrO ₂ , bulk	74	0.424	0.2 mg cm ⁻² loading on Ti, pH = 1 in HClO ₄ 0.1 M ³⁸
IrO ₂ -(100) \geq 25 nm thick thin film	87 *	0.240 *	PLD grown film on SrTiO ₃ -(001), pH = 1 in HClO ₄ 0.1 M ¹²
IrO ₂ -(110) \geq 25 nm thick thin film	83 *	0.317 *	PLD grown film on BaTiO ₃ /MgO-(001), pH = 1 in HClO ₄ 0.1 M ¹²
IrO ₂ , \varnothing = 6 nm nanoparticles	46.5 *	0.350 *	0.05 mg cm ⁻² loading, glassy carbon, rotating disc, pH = 1 in HClO ₄ 0.1 M ¹³
IrO ₂ film, electro- floculated from \varnothing = 2 nm nanoparticles	187 *	0.493 *	two data points undefined pH, glassy carbon, rotating disc ¹⁵
NiFe-LDH nanosheets	40	0.302	0.07 mg cm ⁻² , pH = 14 in KOH 1 M, glassy carbon electrodes ¹⁹
IrO ₂ particles	47	0.338	0.21 mg cm ⁻² , pH = 14 in KOH 1 M, glassy carbon electrodes ¹⁹

of the CdI_2 -type structure of the parent compound IrOOH consisting of edge-sharing IrO_6 octahedra. The lateral size and height were determined by AFM to be up to $7\ \mu\text{m}$ and $1.02(8)\ \text{nm}$, respectively. As the height of a single crystal slab is only $0.5\ \text{nm}$ in the bulk crystal data, this indicates a change in the hydration behavior upon exfoliation. The nanosheets were incorporated into a dimensionally stable anode on titanium, yielding a Tafel slope and overpotential competitive and even superior to other state-of-the-art iridium oxide catalysts. The electrocatalytic activity is also significantly higher than the precursor bulk compound IrOOH and that of the benchmark catalyst IrO_2 with a rutile-type structure, thus indicating that the trend of increased activity by exfoliation observed in LDHs is a more general characteristic of layered catalysts. As the nanosheets of $[\text{IrO}_2]^x-$ are the first iridium oxide nanostructures featuring a layered structure and the presence of trivalent iridium ions, the layers offer a platform for various studies regarding the difference in electrocatalysis depending on the starting valence of the iridium ion, the active sites in the layered CdI_2 -type structure, and theoretical studies to map the position of the novel iridate nanosheets on the OER volcano plot.

4.4 Experimental

$\text{K}_{0.75}\text{Na}_{0.25}\text{IrO}_2$ The synthesis was adopted from chapter 3 and modified. In a typical experiment, $38.2\ \text{mg}$ ($0.2\ \text{mmol}$, $1\ \text{eq.}$) iridium was ground with a flux of $82\ \text{mg}$ ($0.6\ \text{mmol}$, $3\ \text{eq.}$) $90\ \text{wt\%}\ \text{K}_2\text{CO}_3$ and $10\ \text{wt\%}\ \text{Na}_2\text{CO}_3$, then heated in an corundum crucible in air for $15\ \text{h}$ at $900\ ^\circ\text{C}$. The resulting dark grey, powdery mixture was characterized by PXRD and SEM-EDX.

IrOOH The mixture of $\text{K}_{0.75}\text{Na}_{0.25}\text{IrO}_2$ and remaining flux was washed with HCl ($1\ \text{M}$, $1\ \text{mL}\ \text{mg}^{-1}$) to exchange potassium against protons and to remove remaining carbonate flux

as well as side phases. The mixture was shaken with an orbital shaker for 5 d, the acid was exchanged daily. The product was washed with water and dried at 100 °C for 30 min. The resulting powder was examined by PXRD, DTA-TG and SEM-EDX.

$[\text{IrO}_2]^{x-}$ nanosheets 33.8 mg (1.5 mmol) IrOOH was shaken in an excess of 25 mL of TBAOH 0.1 M. Afterwards, the solution was exchanged for 25 mL of 10 wt% (0.375 M) TBAOH for 2 d. The dispersion was centrifuged at 15000 rpm for 30 min to precipitate all components, the TBAOH solution decanted and exchanged for doubly distilled H_2O . The resulting dark blue, translucent suspension was ultrasonicated for another 30 min to promote the exfoliation into $[\text{IrO}_2]^{x-}$ nanosheets. The dispersion was centrifuged at 1000 rpm for 30 min, the supernatant collected and immediately processed. The dispersion had a concentration of 13.3 mM. To prevent agglomeration, the suspension was stored at 4 °C. The properties of the nanosheets were investigated by TEM, AFM and zeta potential measurements.

Electrode preparation To obtain electrode substrates with an activated surface, the oxide layer present on titanium in air was removed by etching. 1.00 cm x 1.00 cm Ti platelets were etched in a slightly boiling solution of 10 wt% oxalic acid dihydrate in H_2O for 2 h, washed and dried. The bulk compounds, IrOOH , and commercially available powder of IrO_2 were processed into inks by dispersing 4 mg mL^{-1} in an ultrasonic bath for 30 min, then deposited onto the Ti platelets at $T = 160$ °C and heated for another 20 min. The dispersion of $[\text{IrO}_2]^{x-}$ nanosheets was used as is and deposited onto the Ti substrate on a hot plate at 120 °C, 140 °C, 160 °C 180 °C or 200 °C. For the deposition at 300 °C, the dispersion was applied at 120 °C, dried and annealed at 300 °C in a muffle furnace for 20 min. The Ti platelets were loaded by suspension, dried and the weight checked by a microbalance, until a loading of 0.2 mg cm^{-2} was reached. To convert the platelets into electrodes, the backside was contacted side using silver-paste and insulated with epoxy

glue. The electrodes were characterized by SEM and electrochemical means.

4.5 Characterization

Electrochemical characterization The prepared electrodes were investigated in a three-electrode setup with 0.1 M HClO₄ as the electrolyte. The setup consisted of the working electrode, a platinum counter electrode as well as a Ag/AgCl/saturated KCl reference electrode (0.197 V vs SHE), attached to an Ivium CompactStat potentiostat/galvanostat/zero resistance ammeter. The scan speed was set to 5 mV s⁻¹ to avoid bubble formation. The system was calibrated by measuring the open circuit potential of a Pt working and Pt counter electrode in a H₂ saturated solution. For OER measurements, the system was saturated with O₂ prior to characterizing the working electrodes. Ohmic drop correction was performed using the current interrupt method. All data were corrected for internal resistance (iR) using the Ivium Potentiostat software. Tafel slopes were calculated from the overpotential η vs. logarithmic current density $\log j$ curves at the current density range of 0.3 - 10 mA cm⁻².

Other characterization methods PXRD measurements were performed on a Stoe Stadi-P (Stoe, Darmstadt, Germany) utilizing Ag-K _{α 1} radiation (Ge(111) monochromator, $\lambda = 0.559407$ Å) and a Mythen Dectris detector in transmission geometry. All powder diffraction patterns were recorded at room temperature. The powders of all products were intermixed with approximately the same volume of ground capillary glass to reduce the effect of absorption and preferred orientation.

Elemental analysis was performed on a scanning electron microscope (SEM; Vega TS 5130 MM, Tescan, Kohoutovice, Czech Republic) with a SEM-EDX using a Si/Li detector (Oxford, United Kingdom). ICP-AES was measured on a Vista Pro ICP-AES spectrome-

ter. SEM imaging was performed on a Merlin SEM (Carl Zeiss AG, Jena, Germany).

AFM was performed on a MFP-3D AFM by Asylum Research / Oxford Instruments in intermittent contact mode with Olympus cantilever (resonance frequency approximately 300 kHz).

TEM samples were prepared by dropping the colloidal nanosheet suspension of [RuCl₃]^{x-} onto a lacey carbon film/copper grid (Plano) and subsequent drying under IR-light irradiation. TEM was performed with a Phillips CM30 ST (300 kV, LaB₆ cathode), with a CMOS camera (TemCam-F216, Tietz) for recording bright field images and selected area electron diffraction (SAED) patterns. The simulation of the diffraction pattern was performed with the program JEMS (Stadelmann).

Differential thermal analysis with thermogravimetry was performed on a STA 409 CD cell (Netzsch GmbH, Germany).

References

- [1] Lewis, N. S.; Nocera, D. G. *Proc. Natl. Acad. Sci. U.S.A.* **2006**, *103*, 15729–35.
- [2] Rossmeisl, J.; Qu, Z.-W.; Zhu, H.; Kroes, G.-J.; Nørskov, J. *J. Electroanal. Chem.* **2007**, *607*, 83–89.
- [3] Koper, M. T. *J. Electroanal. Chem.* **2011**, *660*, 254–260.
- [4] Gray, H. B. *Nat. Chem.* **2009**, *1*, 7.
- [5] Bockris, J.; Otagawa, T. *Journal of The Electrochemical Society* **1984**, *131*, 290–302.
- [6] Matsumoto, Y.; Sato, E. *Mater. Chem. Phys.* **1986**, *14*, 397–426.
- [7] Lu, Z.; Xu, W.; Zhu, W.; Yang, Q.; Lei, X.; Liu, J.; Li, Y.; Sun, X.; Duan, X. *Chemical Communications* **2014**, *50*, 6479.

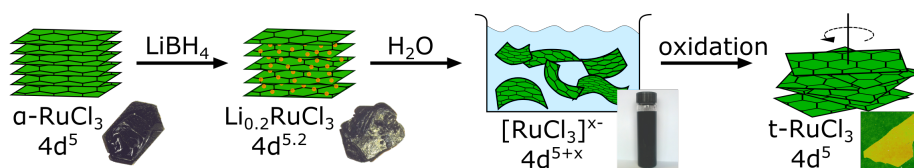
- [8] Song, F.; Hu, X. *Nat. Commun.* **2014**, *5*.
- [9] Walter, M. G.; Warren, E. L.; McKone, J. R.; Boettcher, S. W.; Mi, Q.; Santori, E. A.; Lewis, N. S. *Chem. Rev.* **2010**, *110*, 6446–6473.
- [10] McCrory, C. C. L.; Jung, S.; Peters, J. C.; Jaramillo, T. F. *J. Am. Chem. Soc.* **2013**, *135*, 16977–16987.
- [11] Suntivich, J.; May, K. J.; Gasteiger, H. A.; Goodenough, J. B.; Shao-Horn, Y. *Science* **2011**, *334*, 1383–1385.
- [12] Stoerzinger, K. A.; Qiao, L.; Biegalski, M. D.; Shao-Horn, Y. *Journal of Physical Chemistry Letters* **2014**, *5*, 1636–1641.
- [13] Lee, Y.; Suntivich, J.; May, K. J.; Perry, E. E.; Shao-Horn, Y. *Journal of Physical Chemistry Letters* **2012**, *3*, 399–404.
- [14] Zhao, Y.; Hernandez-Pagan, E. A.; Vargas-Barbosa, N. M.; Dysart, J. L.; Mallouk, T. E. *The Journal of Physical Chemistry Letters* **2011**, *2*, 402–406.
- [15] Nakagawa, T.; Beasley, C. A.; Murray, R. W. *Journal of Physical Chemistry C* **2009**, *113*, 12958–12961.
- [16] Voiry, D.; Salehi, M.; Silva, R.; Fujita, T.; Chen, M.; Asefa, T.; Shenoy, V. B.; Eda, G.; Chhowalla, M. *Nano Letters* **2013**, *13*, 6222–6227.
- [17] Jenjeti, R. N.; Austeria, M. P.; Sampath, S. *ChemElectroChem* **2016**, *3*, 1392–1399.
- [18] Zhao, W.; Dong, B.; Guo, Z.; Su, G.; Gao, R.; Wang, W.; Cao, L. *Chem. Commun.* **2016**, *52*, 9228–9231.
- [19] Long, X.; Li, J.; Xiao, S.; Yan, K.; Wang, Z.; Chen, H.; Yang, S. *Angewandte Chemie International Edition* **2014**, *53*, 7584–7588.

- [20] Ma, T. Y.; Cao, J. L.; Jaroniec, M.; Qiao, S. Z. *Angew. Chem. Int. Ed.* **2016**, *55*, 1138–1142.
- [21] Novoselov, K. S.; Jiang, D.; Schedin, F.; Booth, T. J.; Khotkevich, V. V.; Morozov, S. V.; Geim, A. K. *Proceedings of the National Academy of Sciences* **2005**, *102*, 10451–10453.
- [22] Benameur, M. M.; Radisavljevic, B.; Héron, J. S.; Sahoo, S.; Berger, H.; Kis, A. *Nanotechnology* **2011**, *22*, 125706–125710.
- [23] Eda, G.; Yamaguchi, H.; Voiry, D.; Fujita, T.; Chen, M.; Chhowalla, M. *Nano Lett.* **2011**, *11*, 5111–5116.
- [24] Lerf, A.; Schoellhorn, R. *Inorganic Chemistry* **1977**, *16*, 2950–2956.
- [25] Szendrei, K.; Ganter, P.; Sánchez-Sobrado, O.; Eger, R.; Kuhn, A.; Lotsch, B. V. *Adv. Mater.* **2015**, *27*, 6341–6348.
- [26] Nakayama, M.; Konishi, S.; Tagashira, H.; Ogura, K. *Langmuir* **2005**, *21*, 354–359.
- [27] Ziegler, C.; Werner, S.; Bugnet, M.; Wrsching, M.; Duppel, V.; Botton, G. A.; Scheu, C.; Lotsch, B. V. *Chemistry of Materials* **2013**, *25*, 4892–4900.
- [28] Omomo, Y.; Sasaki, T.; Wang, L.; Watanabe, M. *Journal of the American Chemical Society* **2003**, *125*, 3568–75.
- [29] Kim, T. W.; Oh, E.-J.; Jee, A.-Y.; Lim, S. T.; Park, D. H.; Lee, M.; Hyun, S.-H.; Choy, J.-H.; Hwang, S.-J. *Chemistry - A European Journal* **2009**, *15*, 10752–61.
- [30] Sugimoto, W.; Iwata, H.; Yasunaga, Y.; Murakami, Y.; Takasu, Y. *Angew. Chem. Int. Ed.* **2003**, *42*, 4092–6.
- [31] Kuhn, A. T.; Wright, P. M. *Industrial Electrochemical Processes* **1971**, 525.

-
- [32] Menzel, N.; Ortel, E.; Mette, K.; Kraehnert, R.; Strasser, P. *ACS Catal.* **2013**, *3*, 1324–1333.
- [33] Sun, W.; Song, Y.; Gong, X.-Q.; Cao, L.-m.; Yang, J. *ACS Applied Materials & Interfaces* **2016**, *8*, 820–826.
- [34] Hu, J.-M.; Zhang, J.-Q.; Cao, C.-N. *International Journal of Hydrogen Energy* **2004**, *29*, 791–797.
- [35] Lyons, M. E. G.; Floquet, S. *Phys. Chem. Chem. Phys.* **2011**, *13*, 5314–5335.
- [36] Rasiyah, P.; Tseung, A. *J. Electrochem. Soc.* **1984**, *131*, 803–808.
- [37] Nakagawa, T.; Bjorge, N.; Murray, R. *J. Am. Chem. Soc.* **2009**, *131*, 15578–15579.
- [38] Sun, W.; Song, Y.; Gong, X.-Q.; Cao, L.-m.; Yang, J. *ACS Applied Materials & Interfaces* **2016**, *8*, 820–826.

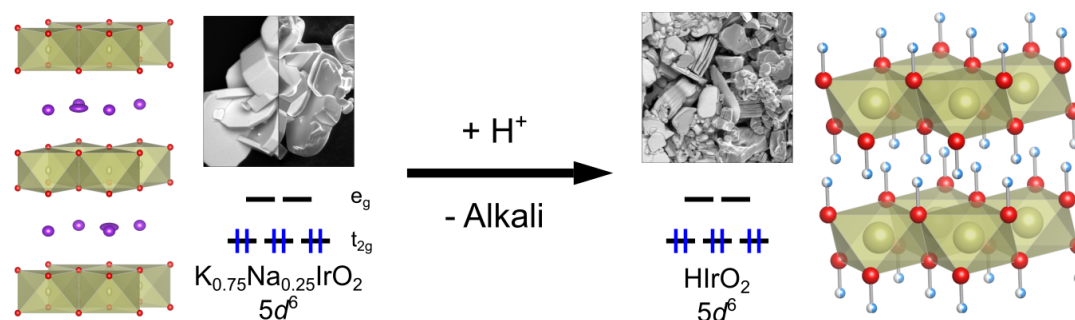
5 Summary

Magnetic properties of restacked 2D spin 1/2 honeycomb RuCl_3 nanosheets



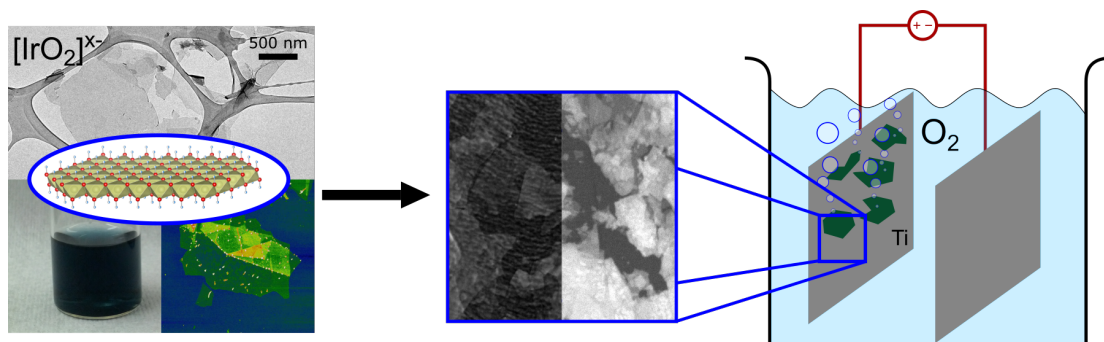
Nanosheets of with the composition $[\text{RuCl}_3]^{x-}$ have been synthesized from the layered bulk crystals of $\alpha\text{-RuCl}_3$ with the honeycomb structure by lithiation and subsequent hydration of Li^+ in water. The resulting nanosheets were 1.06(6) nm high and have a lateral area of up to $450 \mu\text{m}^2$. The in-plane AlCl_3 -type structure was retained during the exfoliation process. Due to the electron injection and the change of the average electron configuration, the spin lattice in the intermediate compound $\text{Li}_{0.2}\text{RuCl}_3$ and the restacked nanosheet pellet was disordered, leading to paramagnetic behavior which deviates from the cooperative magnetism of $\alpha\text{-RuCl}_3$. Oxidation of the nanosheet pellet does not damage the in-plane structure, but restores the trivalent state of ruthenium and leads to a return of cooperative magnetism. PXRD shows signs of turbostratic disorder in the nanosheet pellet along in the stacking direction, which leads to a disruption of the crystal as well as spin lattice along the stacking direction.

Structure and Magnetic Behavior of the Layered Triangular Lattice Iridates $\text{K}_{0.75}\text{Na}_{0.25}\text{IrO}_2$ and IrOOH



A new layered iridate $\text{K}_{0.75}\text{Na}_{0.25}\text{IrO}_2$ has been prepared under high temperature conditions in the presence of air and an alkali carbonate flux. The average space group is $P\bar{3}m1$ with the lattice parameters $a = 3.137(2)$ Å and $c = 6.254(4)$ Å. The iridium and oxygen atoms arrange in a CdI_2 -type layer of $[\text{IrO}_2]^-$, while the alkali ions occupy the interlayer space. By a reaction with hydrochloric acid, the alkali cations were exchanged for protons, yielding the compound IrOOH . While the protonated form crystallizes in the same space group $P\bar{3}m1$ with a similar lattice parameter $a = 3.11345(9)$ Å, the layer repeating distance shrinks to $c = 4.6396(3)$ Å due to the difference in cation size. The layered $[\text{IrO}_2]^-$ structural motif found in the alkali-form was retained in IrOOH . Resistivity measurements reveal the semiconducting nature of $\text{K}_{0.75}\text{Na}_{0.25}\text{IrO}_2$. Magnetic measurements as well as the composition of $\text{K}_{0.75}\text{Na}_{0.25}\text{IrO}_2$ and IrOOH indicate a $5d^6$ electron configuration for iridium, a valency not yet found in crystalline oxoiridates with an octahedral coordination sphere of iridium.

Synthesis of $[\text{IrO}_2]^{x-}$ Nanosheets and Investigations of their Electrocatalytic Properties



Exfoliation of IrOOH in TBAOH solution yields nanosheets with the composition $[\text{IrO}_2]^{x-}$, the first iridium based monolayers. The single layers have a height of 1.02(8) nm and a lateral extension of up to 7 μm . The structural investigations by TEM suggest that the CdI_2 -type layer structure seen in IrOOH is retained during the exfoliation process and the elemental composition of the nanosheets is iridium : oxygen = 1:2. The nanosheets were applied to Ti platelets as the active component for electrochemical water oxidation. With a Tafel slope of 58(3) mV dec^{-1} , an overpotential at 10 mA cm^{-2} of $\eta = 344(7)$ mV and a current density at $\eta = 300$ mV of $j = 1.8(4)$ mA cm^{-2} , the electrodes of $[\text{IrO}_2]^{x-}$ show an increased activity compared to bulk IrO_2 and bulk IrOOH electrodes under the same measurement conditions. The comparison to literature values for known IrO_x -based electrocatalysts suggests that $[\text{IrO}_2]^{x-}$ is competitive regarding the catalytic activity for water oxidation under acidic conditions.

6 Outlook

As can be seen from the previous chapters, the synthesis and characterization of inorganic monolayers is a vivid and growing field. The composition of 2D compounds is a degree of freedom which is a rich playground for chemists on the nanoscale and requires a solid knowledge of synthetic procedures and nanoscale characterization techniques. When comparing Table 1.1 to predictions from the literature,¹⁻³ one can see that there is still a lot of work waiting to be done to fill the white spots on the map.

Yet, the discovery of new monolayer systems and procedures for large-scale synthesis are only two of the possible future directions. Equally important is the post-synthetic modification of nanosheets by soft chemistry. One possibility is the variation of the valency of the cation. In bulk solids, this approach was used to induce superconductivity in NaCoO_2 by oxidizing cobalt with bromine. This led to a reduced layer charge and enabled the hydration and thus separation of the $[\text{CoO}_2]^{x-}$ layers.⁴ As shown in chapter 2, the monolayers of inorganic compounds can withstand such harsh treatment. Therefore, one can imagine the modification of trivalent iridate oxide layers by redox chemistry, to alter their catalytic and magnetic behavior due to non-integer valence states.

Other possibilities are the modification of monolayers with organic functional groups. Initial experiments in this direction investigated the electronic effect of methyl-termination in $\text{Ge}-\text{CH}_3$ compared to germanane GeH .⁵ Both compounds result from a topotactic reaction of CaGe_2 , yet the methyl termination greatly improved the thermal stability, as

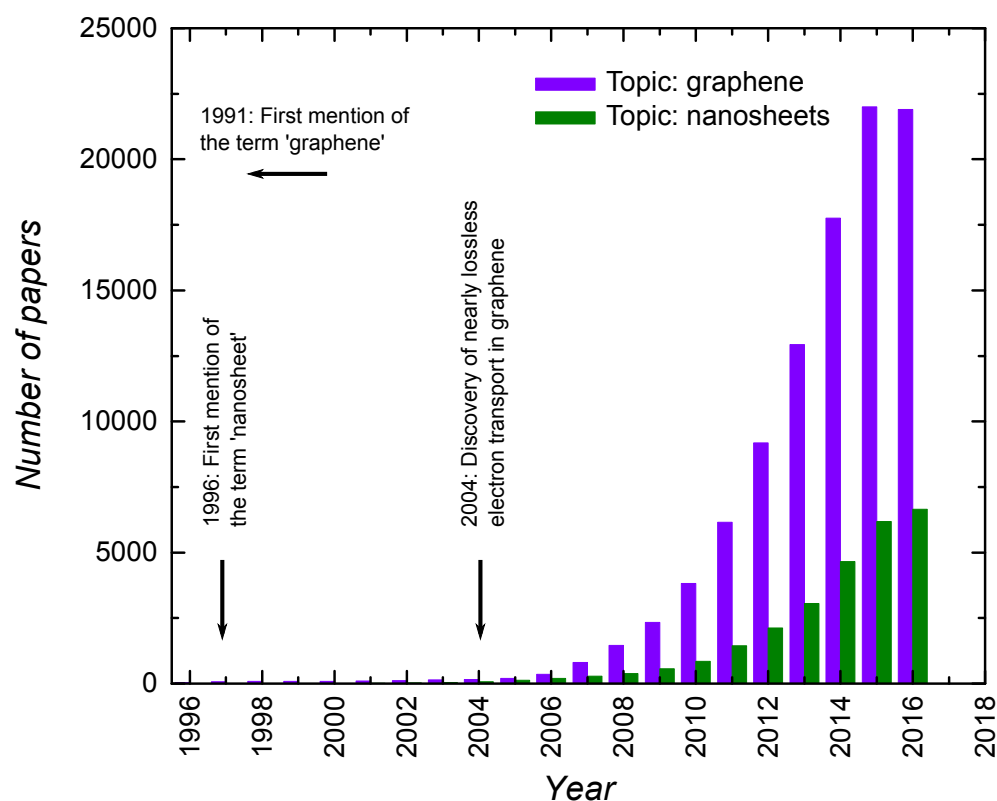


Figure 6.1: Number of papers published on the topics 'graphene' and 'nanosheet', from Web of Science.⁷

Ge-CH₃ decomposes at 250 °C instead of 75 °C like GeH. This emphasizes how kinetics, a concept utilized by chemists on a daily basis, can be used to stabilize otherwise sensitive monolayer compounds. The functionalization also increases the band gap from 0.1 eV in the hydrogen-terminated to 1.7 eV in the methyl-terminated compound, pointing out the possibility to manipulate the electronic structure by the right functional group. Modifying the already sensitive monolayers with functional groups of specific chemical reactivity could allow to build sensors which react to certain, maybe even chiral chemicals. Initial investigations have been launched by modification of MoS₂ for bio-sensing.⁶

But next to the knowledge about chemical methods, the collaboration with the physics community is key. Investigations into nanoscopic objects can yield surprising results, once local probes such as confocal Raman scattering or scanning tunneling microscopes are

applied. In RuCl_3 , Raman spectroscopy at low temperature was applied to investigate the magnon behavior in the bulk compound. As inelastic light scattering has been applied to many nanosheet systems, it could be one tool to investigate the effect of exfoliation on the magnetic structure and thereby support the exploration of Kitaev-Heisenberg-physics.

Luckily, there is plenty of momentum for research on 2D compounds, as can be seen by the number of papers published on the topic 'graphene' and 'nanosheet*' in Figure 6.1 and the two roadmaps for exploring the technological relevant aspects of graphene³ and 2D compounds.² But it is not only the research community, that is fascinated with monolayers of matter. The European Union started the Graphene Flagship in 2013,⁸ funding various projects with 1 billion euros over the time span of 10 years. This is testament to the political will to capitalize on the properties of monolayers and the curiosity of many scientists will drive the future research and bring nanosheet devices to the high-tech world and households alike.

References

- [1] Miró, P.; Audiffred, M.; Heine, T. *Chem. Soc. Rev.* **2014**, *43*, 6537.
- [2] Ferrari, A. C. et al. *Nanoscale* **2015**, *7*, 4598–4810.
- [3] Novoselov, K. S.; Fal'ko, V. I.; Colombo, L.; Gellert, P.; Schwab, M.; Kim, K. *Nature* **2012**, *490*, 192–200.
- [4] Takada, K.; Sakurai, H.; Takayama-Muromachi, E.; Izumi, F.; Dilanian, R. A.; Sasaki, T. *Nature* **2003**, *422*, 53–55.
- [5] Jiang, S.; Butler, S.; Bianco, E.; Restrepo, O. D.; Windl, W.; Goldberger, J. E. *Nature Communications* **2014**, *5*.

-
- [6] Voiry, D.; Goswami, A.; Kappera, R.; e Silva, C. d. C. C.; Kaplan, D.; Fujita, T.; Chen, M.; Asefa, T.; Chhowalla, M. *Nature chemistry* **2015**, 7, 45–49.
- [7] Web of Science - search: 'topic:graphene' and 'topic:nanosheet*'. <http://apps.webofknowledge.com>, Accessed: 2017-12-14, 9:23.
- [8] The Graphene Flagship is a Future and Emerging Technology Flagship by the European Commission. <http://graphene-flagship.eu/project/Pages/About-Graphene-Flagship.aspx>, Accessed: 2017-12-23, 15:28.

A Supporting Information on Chapter 2

A.1 Synthesis

α -RuCl₃ Large crystals were grown by chemical vapor transport as described in the literature.¹ Commercial RuCl₃ powder (99.9 %, Roth) was sealed under vacuum in a quartz ampoule. The powder was heated with 3 K min⁻¹ to 1023 K and held there for 36 h to 120 h, depending on the amount with a temperature gradient of approximately 50 K to 75 K from the feed to the growth zone. The reaction yielded black, crystalline platelets with edge lengths of up to 3 mm, which were analysed by means of PXRD, single crystal X-ray diffraction, SEM-EDX and elemental analysis. Smaller crystals for single crystal X-ray diffraction were grown at 923 K.

Li_{0.2}RuCl₃ The synthesis is a modification of a known procedure.² α -RuCl₃ was combined with tetrahydrofuran (THF) and LiBH₄ under argon atmosphere. In a typical synthesis, 11.77 mL dry THF were added to 483 mg (2.33 mmol, 1 eq.) α -RuCl₃ crystals in a Schlenk flask under Ar atmosphere. 0.23 mL of LiBH₄ (2 mol L⁻¹ in THF, 0.466 mmol, 0.2 eq.) were added under counter flow of argon and the mixture was stirred over night. After washing the product with 3x 12 mL dry THF, Li_{0.2}RuCl₃ was introduced into double distilled H₂O and shaken over night to yield a black suspension. The remaining solid was separated by centrifugation. The concentration of the dispersion was 2.3 mM. The dis-

persion was washed by centrifugation at 18000 rpm and the remaining clear supernatant separated from the pellet. The solid pellet was redispersed in water and the washing procedure repeated three times. Pellets were prepared by dropping parts of the dispersion onto a glass substrate at 60 °C. Upon solvent evaporation, new drops were added until the desired amount was reached.

t-RuCl₃ [RuCl₃]^{x-} pellets on substrates were placed in a closed vessel with some droplets of bromine or granules of iodine over night.

A.2 Single crystal X-ray diffraction

Diffraction data sets were collected at 298 K on a three circle diffractometer (Bruker AXS, Karlsruhe, Germany) equipped with SMART APEX I CCD, using Mo-K $_{\alpha}$ radiation ($\lambda = 0.71073$ Å). The collection and reduction of data were carried out with the BRUKER SUITE software package.⁴ It turned out that the crystal under investigation was systematically twinned (dovetail twin for the monoclinic system), and the twin-law (100, 0-10, 001) had to be applied during data reduction. The intensities were corrected for absorption effects applying a multi-scan method with TWINABS.³ The structure was solved by Direct Methods and refined by full matrix least-squares fitting with the SHELXTL software package.⁵ Some residual occupancy was found in the empty octahedron of the α -RuCl $_3$ structure, a consequence of disorder in the layer stacking. Experimental details of data collection and crystallographic data are given in Tables SA.1, SA.2 and SA.3.

A.3 Other analytical methods

PXRD in-plane measurements were performed on a Stoe Stadi-P (Stoe Darmstadt, Germany) utilizing Cu-K $_{\alpha 1}$ radiation (Ge(111) monochromator, $\lambda = 1.54059$ Å) and a Mythen Dectris detector in transmission geometry. The out-of-plane measurements were performed on a Bruker D8-Advance with Cu-K $_{\alpha 1}$ radiation (Ge(111) monochromator, $\lambda = 1.54059$ Å), in reflection geometry, using a Vantec detector. All powder diffraction patterns were recorded at room temperature.

Elemental analysis for lithium and ruthenium was performed on a Vista Pro ICP-AES spectrometer. Ruthenium to chloride ratios were measured on a scanning electron microscope (SEM; Vega TS 5130 MM, Tescan) with a SEM-EDX using a Si/Li detector (Oxford).

AFM was performed on a MFP-3D AFM by Asylum Research / Oxford Instruments in intermittent contact mode with Olympus cantilever (resonance frequency approximately 300 kHz).

TEM samples were prepared by dropping the colloidal nanosheet suspension of $[\text{RuCl}_3]^{\text{x-}}$ onto a lacey carbon film/copper grid (Plano) and subsequent drying under IR-light irradiation. TEM was performed with a Phillips CM30 ST (300 kV, LaB_6 cathode), with a CMOS camera (TemCam-F216, Tietz) for recording bright field images and selected area electron diffraction (SAED) patterns. The simulation of the diffraction pattern was performed with the program JEMS (Stadelmann).

Measurements of the magnetic properties were performed on a MPMS by Quantum Design. The specific heat data was collected on a PPMS, also by Quantum Design.

Table A.1: Crystal data and structure refinement data of α -RuCl₃.

	α -RuCl ₃
Temperature / K	298(2)
Formula weight / g/mol ⁻¹	207.43
Space group (no.), Z	<i>C</i> 2/ <i>m</i> , 4
Lattice constants / Å	$a = 5.9917(13)$ $b = 10.367(2)$ $c = 6.0543(13)$
V / Å ³ , $\rho_{\text{X-ray}}$ / g cm ⁻³	356.21(13), 3.868
Crystal size / mm ⁻³	0.10 x 0.08 x 0.04
Diffractometer	SMART APEX I, Bruker AXS
X-ray radiation, λ / Å	0.71073
Absorption correction	Multi-scan, TWINABS ³
2θ range / °	5.73 - 68.75
Index range	$-9 \leq h \leq 9$ $0 \leq k \leq 16$ $0 \leq l \leq 9$
Reflection collected	2803
Data, R_{int}	748, 0.052
No. of parameters	27
Transmission: t_{max} , t_{min}	0.271, 0.167
$R_1[F^2 > 2\sigma(F^2)]$	0.043
$wR(F^2)$	0.108
Twin volume fraction	0.27
$\Delta\rho_{\text{max}}$, $\Delta\rho_{\text{min}}$ / e Å ⁻³	2.437, -1.880

Table A.2: Atomic coordinates and equivalent displacement parameters U^{eq} ($\text{\AA}^2 \times 10^4$) for $\alpha\text{-RuCl}_3$ at 298 K.

Atom	site	x	y	z	SOF	U^{eq}
Ru1	$4g$	0	0.33338(4)	0	0.955(4)	124(2)
Ru2	$2a$	0	0	0	2-2xSOF(Ru1)	394(44)
Cl1	$8j$	0.7513(2)	0.1736(1)	0.7681(2)	1	174(3)
Cl2	$4i$	0.7277(3)	0	0.2340(3)	1	181(4)

Table A.3: Anisotropic displacement parameters U^{ij} ($\text{\AA}^2 \times 10^4$) for $\alpha\text{-RuCl}_3$ at 298 K.

Atom	U^{11}	U^{22}	U^{33}	U^{12}	U^{13}	U^{23}
Ru1	128(3)	107(3)	155(3)	0	70(2)	0
Ru2	583(91)	367(70)	315(68)	0	262(60)	0
Cl1	180(6)	181(5)	191(6)	-35(3)	101(4)	-37(3)
Cl2	183(7)	147(7)	196(7)	0	37(6)	0

A.4 Further Results

A.4.1 Images of $[\text{RuCl}_3]^{x-}$ and RuCl_3 monolayers

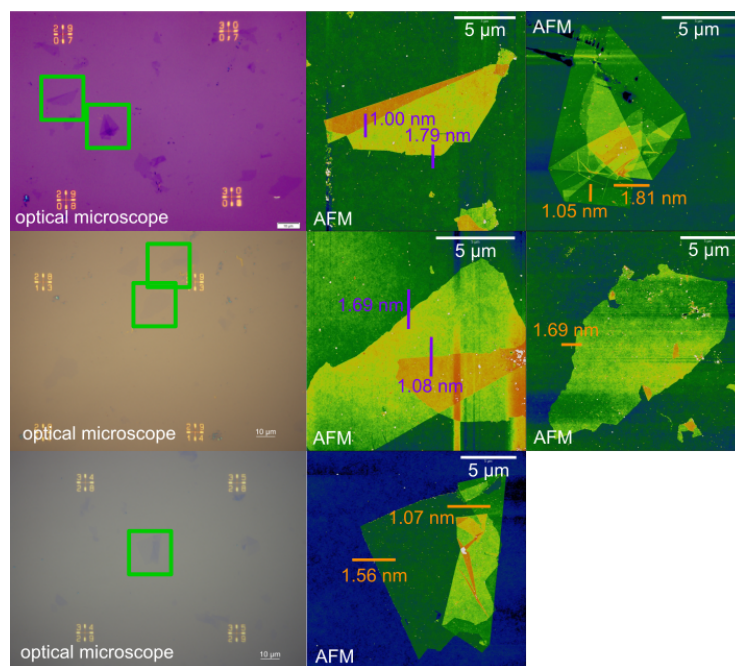


Figure A.1: Optical microscope and AFM images of $[\text{RuCl}_3]^{x-}$ with height from line scan in purple/orange. The height of a single layer with a hydrate shell is consistently around 1.69(9) nm on the wafer and around 1.06(6) nm when measured on an underlayer of $[\text{RuCl}_3]^{x-}$.

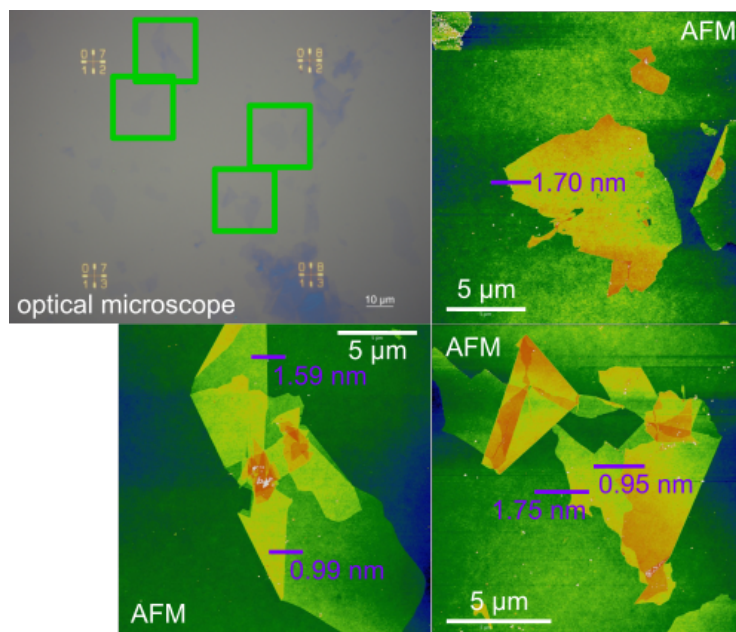


Figure A.2: Second set of optical microscope and AFM images of $[\text{RuCl}_3]^\times$ with height from line scan in purple. The height of a single layer with a hydrate shell is consistently around 1.69(9) nm on the wafer and around 1.06(6) nm when measured on an underlayer of $[\text{RuCl}_3]^\times$.

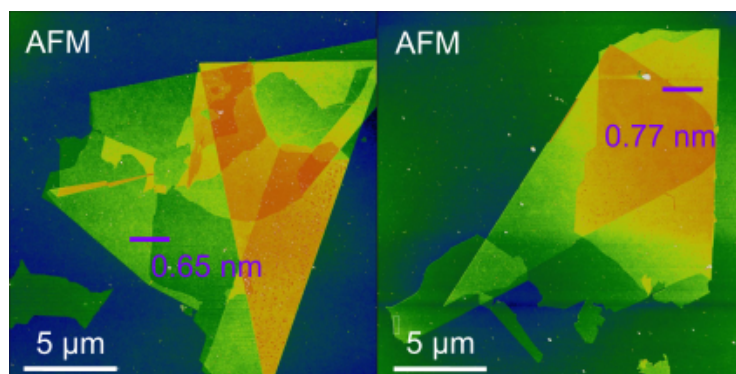


Figure A.3: AFM images of oxidized RuCl_3 monolayer with height from line scan in purple. The height of an oxidized single layer without a hydrate shell is consistently around 0.72(11) nm for all measured batches.

A.4.2 TEM data on $[\text{RuCl}_3]^{x-}$ nanosheets

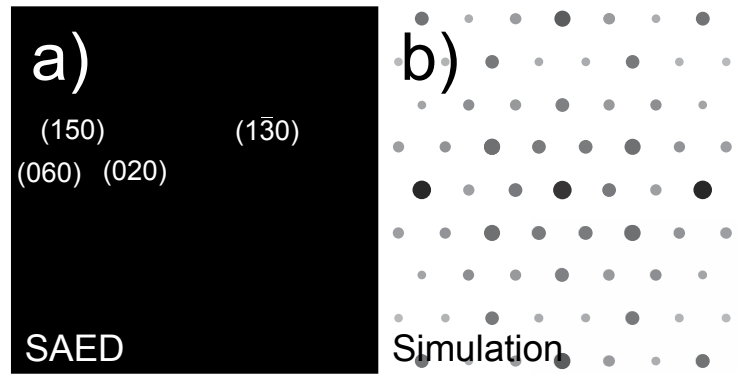


Figure A.4: a) Selected area electron diffraction pattern of $[\text{RuCl}_3]^{x-}$ along $[001]$ zone axis, b) simulation of $\alpha\text{-RuCl}_3$ based on the space group $C2/m$ obtained from single crystal X-ray diffraction.

Table A.4: Comparison of d -values from TEM of a $[\text{RuCl}_3]^{x-}$ single layer, PXRD on the restacked pellet of $[\text{RuCl}_3]^{x-}$ and single crystal X-ray diffraction on $\alpha\text{-RuCl}_3$.

(hkl)	d -values TEM $[\text{RuCl}_3]^{x-}$ [nm]	d -values PXRD $[\text{RuCl}_3]^{x-}$ [nm]	d -values $\alpha\text{-RuCl}_3$ [nm]
(020)	0.527	0.516	0.518
(130)	0.304	0.298	0.295
(040)	0.264	0.257	0.259
(150)	0.199	0.196	0.195
(060)	0.176	0.172	0.173

A.4.3 Magnetic data and Curie-Weiss fits

Table A.5: Weiss temperature θ_{CW} and effective magnetic moment μ_{eff} from Curie-Weiss fits for the in-plane (ip) and out-of-plane (op) direction.

Compound	$\theta_{CW,ip}$ [K]	$\theta_{CW,op}$ [K]	$\mu_{eff,ip}$ [μ_B / Ru]	$\mu_{eff,op}$ [μ_B / Ru]
α -RuCl ₃	31.2(3)	- 137.7(5)	2.26(1)	2.22(1)
Li _{0.2} RuCl ₃	0.6(2)	- 17.8(3)	1.08(2)	1.58(1)
[RuCl ₃] ^{x-}	- 13.5(7)	- 13.5(3)	0.87(1)	1.47(1)
RuCl ₃ -T	17.8(7)	2(2)	2.33(1)	1.27(1)

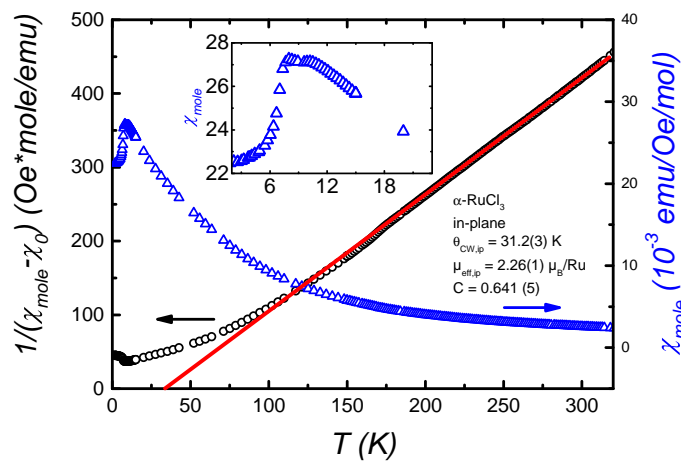


Figure A.5: In-plane magnetic susceptibility and inverse magnetic susceptibility of α -RuCl₃ vs temperature at $\mu_0 H = 1$ T, inset shows susceptibility from $T = 3$ K to 23 K.

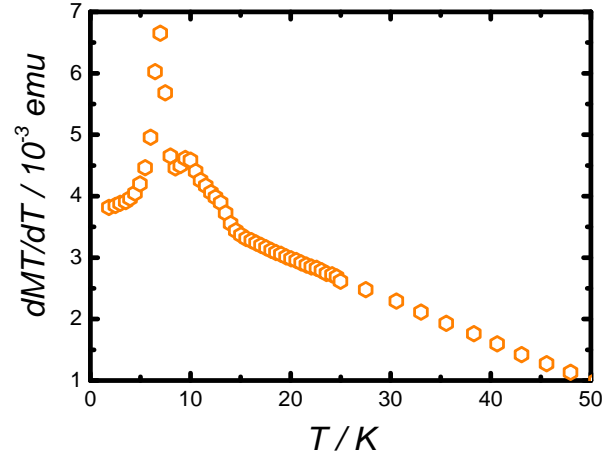


Figure A.6: Plot of dMT/dT for $T = 3$ K to 23 K for the in-plane measurement of α - RuCl_3 . Magnetization (M) is taken as χH .

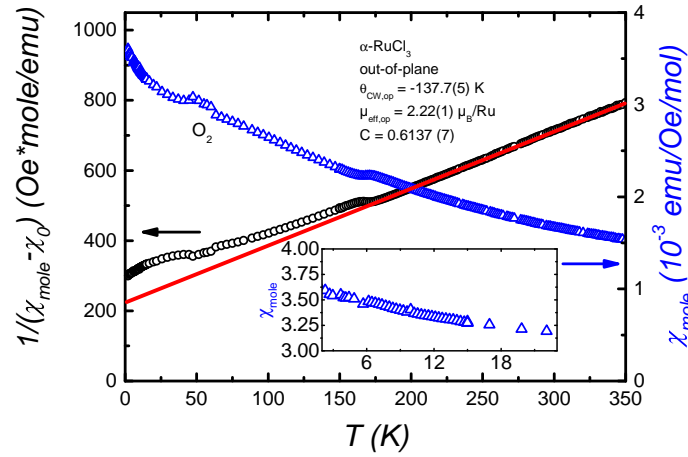


Figure A.7: Out-of-plane magnetic susceptibility and inverse magnetic susceptibility of α - RuCl_3 vs temperature at $\mu_0 H = 1$ T, inset shows susceptibility from $T = 3$ K to 23 K. The discontinuity at around 160 K was observed in the literature⁶ and assumed to be a change in the stacking behavior resulting in a structural phase transition from $C2/m$ to $R\bar{3}$.

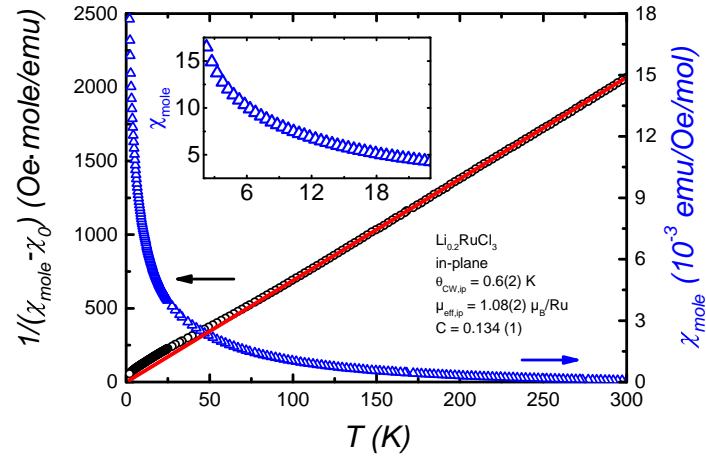


Figure A.8: In-plane magnetic susceptibility and inverse magnetic susceptibility of $\text{Li}_{0.2}\text{RuCl}_3$ vs temperature at $\mu_0 H = 1$ T, inset shows susceptibility from $T = 3$ K to 23 K.

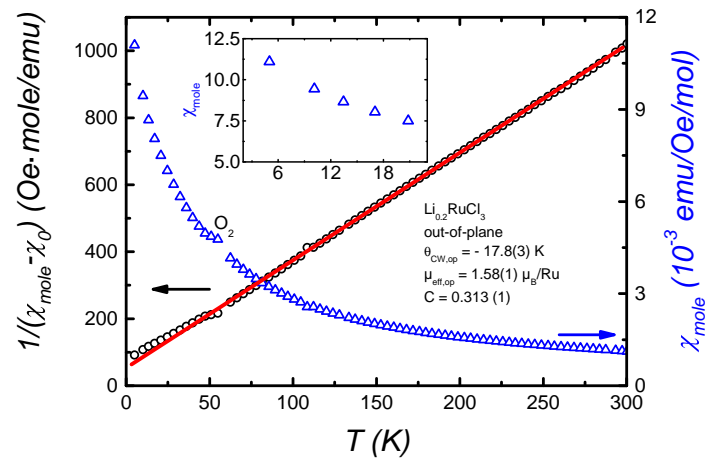


Figure A.9: Out-of-plane magnetic susceptibility and inverse magnetic susceptibility of $\text{Li}_{0.2}\text{RuCl}_3$ vs temperature at $\mu_0 H = 1$ T, inset shows susceptibility from $T = 3$ K to 23 K.

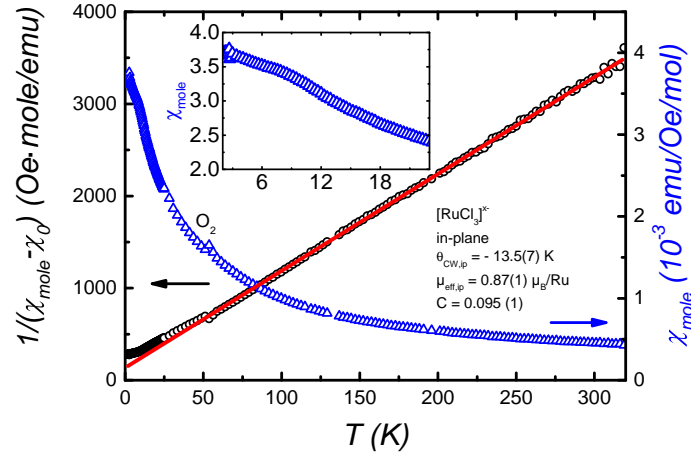


Figure A.10: In-plane magnetic susceptibility and inverse magnetic susceptibility of $[\text{RuCl}_3]^{x-}$ vs temperature at $\mu_0 H = 1$ T, inset shows susceptibility from $T = 3$ K to 23 K.

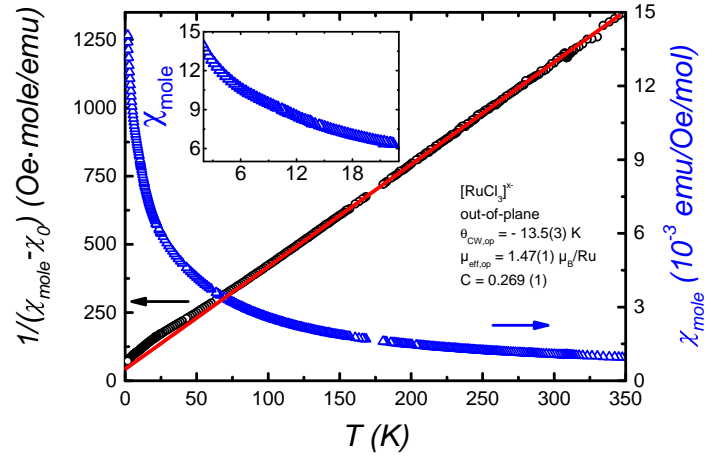


Figure A.11: Out-of-plane magnetic susceptibility and inverse magnetic susceptibility of $[\text{RuCl}_3]^{x-}$ vs temperature at $\mu_0 H = 1$ T, inset shows susceptibility from $T = 3$ K to 23 K.

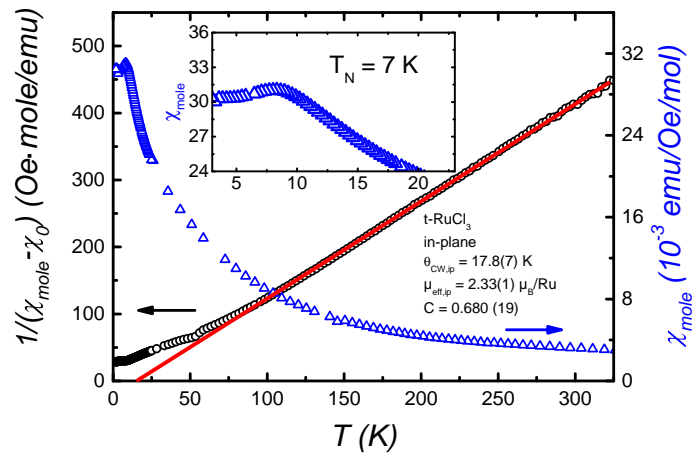


Figure A.12: In-plane magnetic susceptibility and inverse magnetic susceptibility of $t\text{-RuCl}_3$ vs temperature at $\mu_0 H = 1$ T, inset shows susceptibility from $T = 3$ K to 23 K.

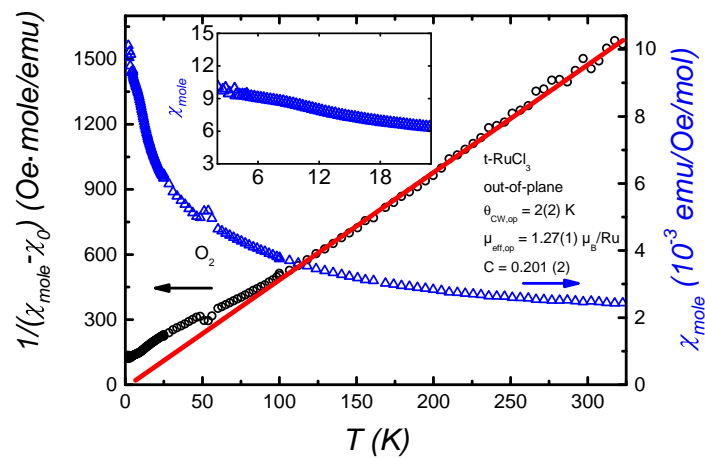


Figure A.13: Out-of-plane magnetic susceptibility and inverse magnetic susceptibility of $t\text{-RuCl}_3$ vs temperature at $\mu_0 H = 1$ T, inset shows susceptibility from $T = 3$ K to 23 K.

A.4.4 Specific heat measurement

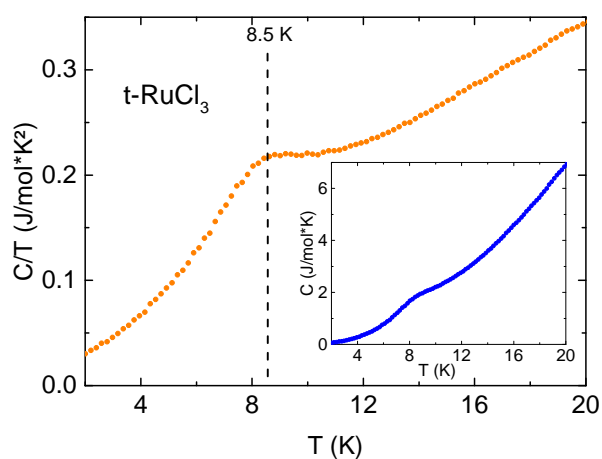


Figure A.14: Temperature dependent specific heat of t-RuCl_3 . A magnetic transition is visible at 8.5 K, no further transitions can be detected below 20 K.

References

- [1] Oppermann, H.; Schmidt, M.; Schmidt, P. *Zeitschrift für anorganische und allgemeine Chemie* **2005**, *631*, 197–238.
- [2] Wang, L.; Rocci-Lane, M.; Brazis, P.; Kannewurf, C. R.; Kim, Y.-I.; Lee, W.; Choy, J.-H.; Kanatzidis, M. G. *J. Am. Chem. Soc.* **2000**, *122*, 6629–6640.
- [3] Sheldrick, G. M. TWINABS. 2012.
- [4] Bruker Suite. 2014.
- [5] Sheldrick, G. M. *Acta Crystallogr., Sect. A: Found. Crystallogr.* **2008**, *64*, 112–122.
- [6] Kubota, Y.; Tanaka, H.; Ono, T.; Narumi, Y.; Kindo, K. *Physical Review B* **2015**, *91*, 094422.

B Supporting Information on Chapter 3

B.1 $\text{K}_{0.75}\text{Na}_{0.25}\text{IrO}_2$

B.2 Single crystal X-ray diffraction

Table B.1: Crystallographic data of $\text{K}_{0.75}\text{Na}_{0.25}\text{IrO}_2$.

Temperature / K	250(2)	100(2)
Space group (no.)	$P6_3/mmc$ (194)	
Lattice parameters / Å	$a = 3.1202(5)$	$a = 3.1194(10)$
	$c = 12.440(2)$	$c = 12.407(4)$
V / Å ³ , Z	104.89(4), 2	104.56(8), 2
ρ / g cm ⁻³	8.210	8.235
Index range	$-5 \leq h \leq 5$ $-5 \leq k \leq 5$ $-20 \leq l \leq 19$	
Number of total reflections	1781	1768
Number of unique reflections	129	
R_{int}	0.0322	0.0285
Number of parameters	14	
Number of restraints	3	
Goodness of Fit	1.453	1.495
Final R indices [$F^2 > 2\sigma(F^2)$]	$R_1 = 0.0322$	$R_1 = 0.0285$
	$wR_2 = 0.0666$	$wR_2 = 0.0642$
Final R indices (all data)	$R_1 = 0.0322$	$R_1 = 0.0285$
	$wR_2 = 0.0666$	$wR_2 = 0.0642$
$\Delta\rho_{\text{max}}, \Delta\rho_{\text{min}}$ / e Å ⁻³	1.273, -2.298	1.277, -1.663

Table B.2: Atomic coordinates and isotropic displacement parameters U^{iso} (\AA^2) for $\text{K}_{0.75}\text{Na}_{0.25}\text{IrO}_2$ at 250 K; parameters without standard deviation were not refined.

Atom	Wyckoff position	x	y	z	SOF	U^{iso}
Ir	$1a$	0	0	0	1	0.0125(2)
O	$2d$	1/3	2/3	0.5819(9)	1	0.0111(16)
K1	$1b$	1/3	2/3	1/4	0.535(2) ^{a)}	0.095(9)
Na1					0.218(2) ^{a)}	
K2	$1b$	0	0	1/4	0.215(2) ^{a)}	0.043(8)
Na2					0.032(2) ^{a)}	

^{a)} Site occupation factors (SOFs) were refined with the following

constraint derived from the SEM-EDX analysis:

$$\text{SOF}(\text{K1}) + \text{SOF}(\text{K2}) = 0.75 \text{ and } \text{SOF}(\text{Na1}) + \text{SOF}(\text{Na2}) = 0.25.$$

Table B.3: Anisotropic atomic displacement parameters U^{ij} (\AA^2) in $\text{K}_{0.75}\text{Na}_{0.25}\text{IrO}_2$ at 250 K; parameters without standard deviation were not refined.

Atom	$U^{11} = U^{22}$	U^{33}	$U^{12} = U^{13}$	U^{23}
Ir	0.0086(2)	0.0204(3)	0	0.00428(12)
O	0.011(2)	0.011(3)	0	0.0056(12)
K1, Na1	0.122(14)	0.042(8)	0	0.061(7)
K2, Na2	0.044(12)	0.041(16)	0	0.022(6)

B.2.1 Band structure

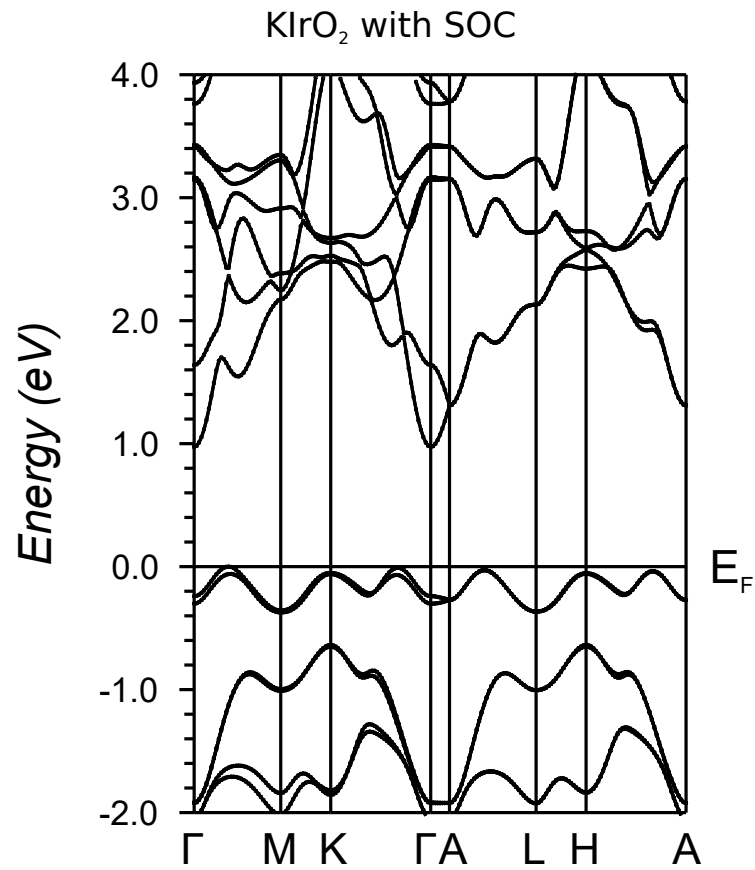


Figure B.1: Electronic band structure of $K_{0.75}Na_{0.25}IrO_2$ based on FP-LAPW (PBE-GGA) with spin-orbit coupling (SOC), simulated with alkali position fully occupied by K^+ .

B.2.2 Density of states

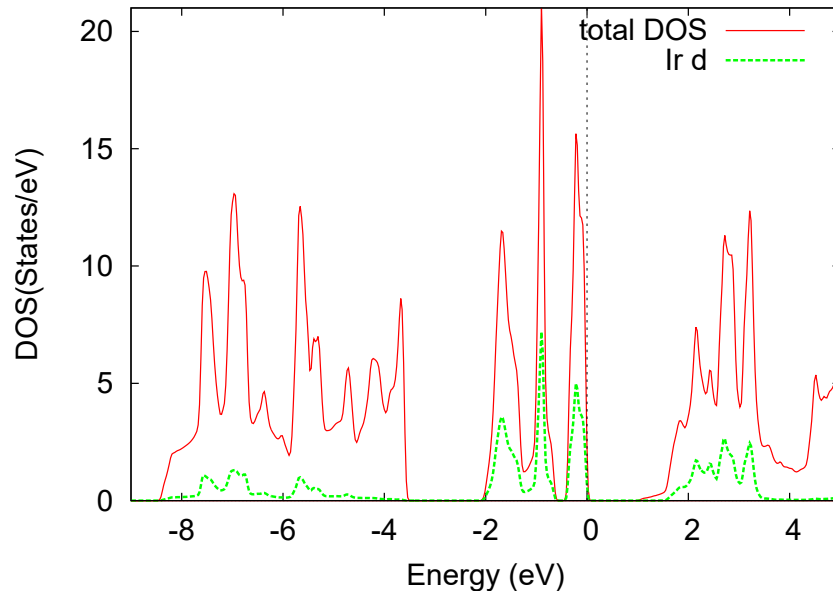


Figure B.2: Total density of states in $\text{K}_{0.75}\text{Na}_{0.25}\text{IrO}_2$ calculated with FP-LAPW (PBE-GGA), simulated with alkali position fully occupied by K^+ .

B.3 IrOOH

B.3.1 Powder X-ray diffraction

Table B.4: Crystallographic data of IrOOH.

Temperature / K	298(2) K
Crystal system	hexagonal
Space group (no.)	$P\bar{3}m1$ (164)
Lattice parameters / Å	$a = 3.11345(9)$ $c = 4.6396(3)$
Z, V / Å ³	1, 38.949(4)
Formula weight / g/mol ⁻¹ , $\rho_{\text{X-ray}}$ / g cm ⁻³	224.216, 9.5592(9)
Absorption coefficient / mm ⁻¹	46.534(4)
detector 2θ range / °	3.080 - 59.756
X-ray radiation, λ / Å	Ag-K $_{\alpha 1}$, 0.559410
Diffractometer, Monochromator	Stoe StadiP, Ge(111)
Data points	4723
Number of observed reflections	65
Number of parameters	44
Number of constraints	1
Structure refinement	Rietveld method
Profile function	Fundamental parameter approach
Background function, order number	Chebyshev, 4th
R_{exp} , R_{wp}	0.0373, 0.0432
R_{p} , R_{Bragg}	0.0345, 0.0186
χ^2	1.16

Table B.5: Atomic coordinates and isotropic displacement parameters U^{eq} (\AA^2) for IrOOH at 298 K; parameters without standard deviation were not refined, * marks constrained parameters.

Atom	Wyckoff position	x	y	z	SOF	U^{eq}
Ir	$1a$	0	0	0	1	$0.295(11)^*$
O	$2d$	$1/3$	$2/3$	$0.2083(18)$	1	$0.295(11)^*$

B.3.2 Thermogravimetry

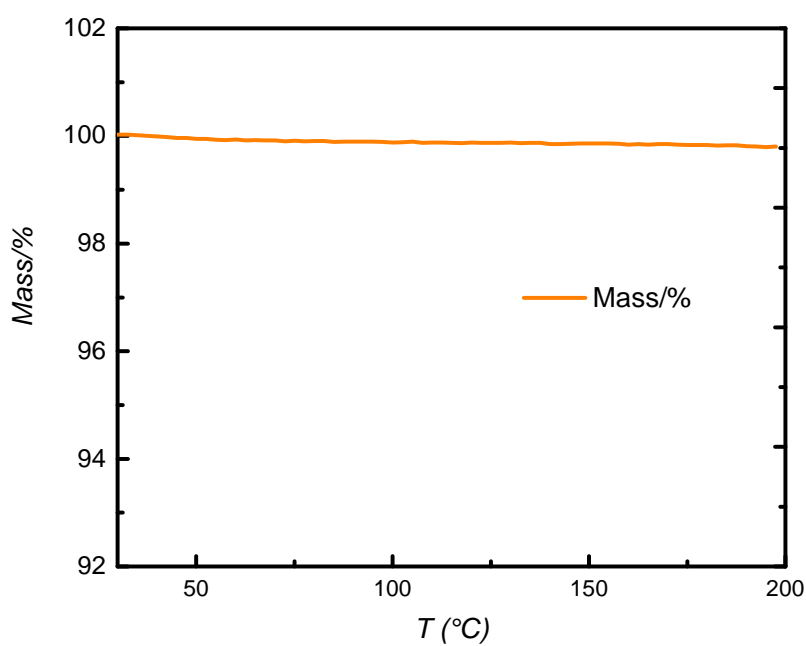


Figure B.3: TG of IrOOH, measured from 30 °C to 200 °C with 2 °C / min in air.

B.4 Electron dispersive X-ray spectroscopy

Table B.6: Expected and measured atomic percentages of K, Na, Ir and O averaged over 12 measurements for each $\text{K}_{0.75}\text{Na}_{0.25}\text{IrO}_2$ and IrOOH .

Atoms in $\text{K}_{0.75}\text{Na}_{0.25}\text{IrO}_2$	K	Na	Ir	O
expected / atom%	18.75	6.25	25	50
measured / atom%	15.7(14)	6.0(8)	22(3)	56(4)
Atoms in IrOOH	K	Na	Ir	O
expected / atom%	0	0	33	67
measured / atom%	0.3(3)	0	27(2)	72(2)

B.5 Magnetometry data including error bars

The error in the SQUID data was determined as a relative error. The two contributing sources were the standard deviation as well as the R^2 fit parameter of the sample position within the superconducting coils. The latter was the dominating contribution, especially at higher temperatures. In the case of the $\text{K}_{0.75}\text{Na}_{0.25}\text{IrO}_2$ crystals, the magnetization decreased strongly, leading to a decrease in the fit quality of the sample position and ultimately to a loss of the sample signal above 73 K.

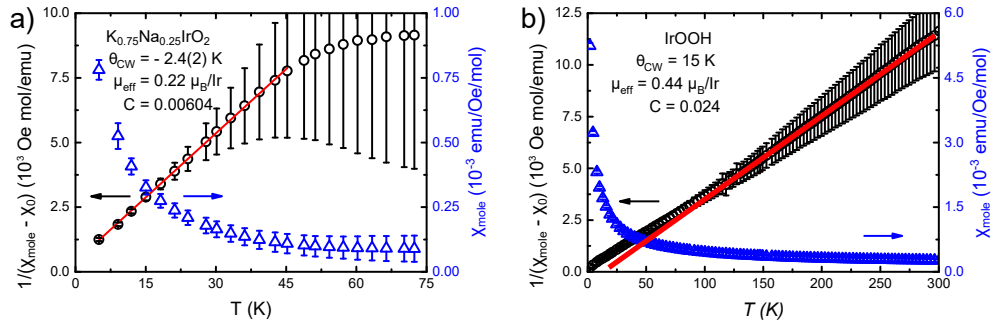


Figure B.4: Susceptibility (blue) and inverse susceptibility (black) of a) $\text{K}_{0.75}\text{Na}_{0.25}\text{IrO}_2$ single crystals and b) IrOOH powder measured in a field of $\mu_0 H = 1 \text{ T}$ with error bars based on the standard deviation and R^2 fit parameter of the sample position, Curie-Weiss fits shown as a red line.

B.6 Bond valence analysis

To prevent a distortion of the bond lengths due to low quality data, datasets older than 40 years as well as structures with mixed site occupancies on the iridium site (i.e. Na_2IrO_3) were excluded. The data used to plot Figure 6 in the main paper is listed in Tables B.7 and B.8.

Table B.7: List of ternary iridium oxide compounds with tri- and pentavalent iridium, their structure type (ST), formal oxidation state (OS), the bond-valence parameters R_0 and B (both in Å),¹ average Ir-O distance \bar{R}_{ij} (in Å), average bond valence per bond \bar{S}_{ij} and bond valence sum $\sum \bar{S}_{ij}$.

Compound	ST	OS	R_0	B	\bar{R}_{ij}	\bar{S}_{ij}	$\sum \bar{S}_{ij}$
$\text{H}_3[\text{Ir}(\text{C}_2\text{O}_4)_3] \cdot 2 \text{H}_2\text{O}^2$	amorphous	3	1.755	0.414	2.02	0.527	3.163
$\text{K}_{0.75}\text{Na}_{0.25}\text{IrO}_2$	β - RbScO_2	3	1.755	0.414	2.070	0.467	2.804
IrOOH	CdI_2	3	1.755	0.414	2.041	0.501	3.006
$\text{Pr}_3\text{IrO}_7^3$	La_3NbO_7	5	1.909	0.449	1.975	0.863	5.1798
$\text{Nd}_3\text{IrO}_7^4$	La_3NbO_7	5	1.909	0.449	2.028	0.767	4.603
$\text{Nd}_3\text{IrO}_7^4$	Nd_3IrO_7	5	1.909	0.449	2.027	0.769	4.613
$\text{Sm}_3\text{IrO}_7^4$	La_3NbO_7	5	1.909	0.449	2.003	0.811	4.867
$\text{Eu}_3\text{IrO}_7^4$	La_3NbO_7	5	1.909	0.449	2.021	0.779	4.675
NaIrO_3^5	NaIrO_3	5	1.909	0.449	1.95	0.913	5.476

Table B.8: Rutile and ternary iridium oxide compounds with tetravalent iridium, their structure type (ST), formal oxidation state (OS), the bond-valence parameters R_0 and B (both in Å),¹ average Ir-O distance \bar{R}_{ij} (in Å), average bond valence per bond \bar{S}_{ij} and bond valence sum $\sum \bar{S}_{ij}$.

Compound	ST	OS	R_0	B	\bar{R}_{ij}	\bar{S}_{ij}	$\sum \bar{S}_{ij}$
IrO ₂ ⁶	rutile–TiO ₂	4	1.909	0.258	1.98	0.759	4.557
Li ₈ IrO ₆ ⁷	Li ₈ SnO ₆	4	1.909	0.258	1.998	0.708	4.249
CaIrO ₃ ⁸	CaIrO ₃	4	1.909	0.258	2.018	0.655	3.933
Ca ₄ IrO ₆ ⁹	K ₄ CdCl ₆	4	1.909	0.258	1.996	0.714	4.283
SrIrO ₃ ¹⁰	SrIrO ₃	4	1.909	0.258	1.973	0.780	4.682
Sr ₅ Ir ₃ O ₁₁ ¹¹	Sr ₅ Ir ₃ O ₁₁	4	1.909	0.258	1.989	0.734	4.400
Sr ₂ IrO ₄ ¹²	Ca ₂ MnO ₄	4	1.909	0.258	2.004	0.692	4.152
BaIrO ₃ ¹³	BaRhO ₃	4	1.909	0.258	2.02	0.651	3.902
Ba ₄ Ir ₃ O ₁₀ ¹⁴	Cs ₄ Mg ₃ F ₁₀	4	1.909	0.258	2.01	0.676	4.056
Ba ₄ Ir ₃ O ₁₀ ¹⁵	Cs ₄ Mg ₃ F ₁₀	4	1.909	0.258	2.03	0.626	3.754
Eu ₂ Ir ₂ O ₇ ¹⁶	Ca ₂ Nb ₂ O ₇	4	1.909	0.258	2.033	0.618	3.710
Pr ₂ Ir ₂ O ₇ ¹⁶	Ca ₂ Nb ₂ O ₇	4	1.909	0.258	2.013	0.668	4.009

References

- [1] Gagné, O. C.; Hawthorne, F. C. *Acta Crystallogr., Sect. B: Struct. Sci.* **2015**, *71*, 562–578.
- [2] Hüppauff, M.; Lengeler, B. *J. Electrochem. Soc.* **1993**, *140*, 598–602.
- [3] Nishimine, H.; Wakeshima, M.; Hinatsu, Y. *J. Solid State Chem.* **2004**, *177*, 739–744.
- [4] Hinatsu, Y.; Doi, Y.; Nishimine, H.; Wakeshima, M.; Sato, M. *J. Alloys Compd.* **2009**, *488*, 541–545.
- [5] Wallace, D. C.; McQueen, T. M. *Dalton Trans.* **2015**, *44*, 20344–20351.

- [6] Bolzan, A. A.; Fong, C.; Kennedy, B. J.; Howard, C. J. *Acta Crystallogr., Sect. B: Struct. Sci* **1997**, *53*, 373–380.
- [7] Kroeschell, P.; Wolf, R.; Hoppe, R. *Z. Anorg. Allg. Chem.* **1986**, *536*, 81–91.
- [8] Martin, C. D.; Smith, R. I.; Marshall, W. G.; Parise, J. B. *Am. Mineral.* **2007**, *92*, 1912–1918.
- [9] Segal, N.; Vente, J. F.; Bush, T. S.; Battle, P. D. *J. Mater. Chem.* **1996**, *6*, 395–401.
- [10] Schmalle, H.; Gurtner, C.; Oswald, H.; Reller, A. *Z. Anorg. Allg. Chem.* **1990**, *191*, 239–248.
- [11] Harlow, R. L.; Li, Z. G.; Marshall, W. J.; Crawford, M. K.; Subramanian, M. A. *Mater. Res. Bull.* **1995**, *30*, 217–223.
- [12] Shimura, T.; Inaguma, Y.; Nakamura, T.; Itoh, M.; Morii, Y. *Phys. Rev. B* **1995**, *52*, 9143.
- [13] Siegrist, T.; Chamberland, B. *J. Less-Common Met.* **1991**, *170*, 93–99.
- [14] Wilkens, J.; Müller-Buschbaum, H. *Z. Anorg. Allg. Chem.* **1991**, *592*, 79–83.
- [15] Stitzer, K. E.; Smith, M. D.; zur Loye, H.-C. *J. Alloys Compd.* **2002**, *338*, 104–111.
- [16] Millican, J. N.; Macaluso, R. T.; Nakatsuji, S.; Machida, Y.; Maeno, Y.; Chan, J. Y. *Mater. Res. Bull.* **2007**, *42*, 928–934.

C Supporting Information on Chapter 4

C.1 AFM images of $[\text{IrO}_2]^{x-}$ nanosheets deposited from undiluted dispersion

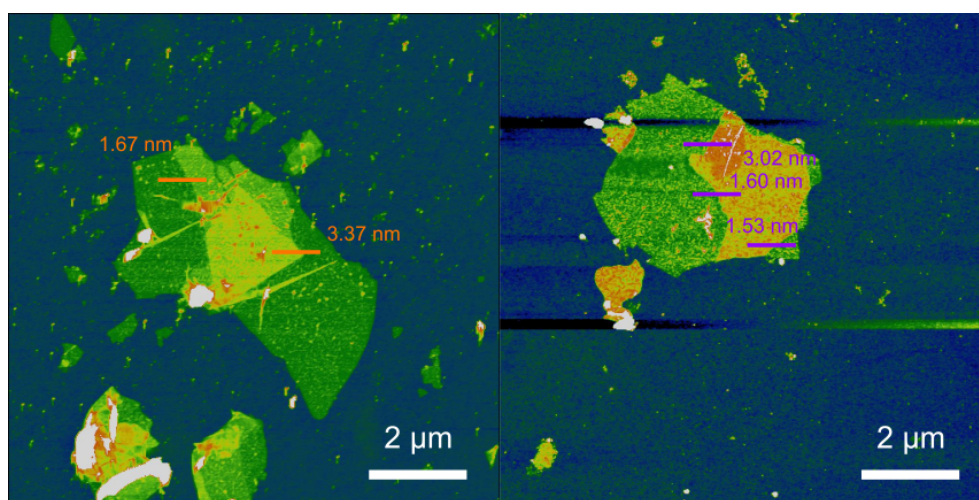


Figure C.1: Exemplary AFM images of $[\text{IrO}_2]^{x-}$ nanosheets deposited from an undiluted dispersion.

C.2 DTA-TG of $(\text{H}, \text{TBA})_x\text{IrO}_2 \cdot y \text{H}_2\text{O}$

The DTA-TG curve of $(\text{H}, \text{TBA})_x\text{IrO}_2 \cdot y \text{H}_2\text{O}$ displayed in figure C.2 shows four mass losses at 67 °C, 144 °C, 257 °C and 532 °C. The first and second mass loss at $T = 67$ °C and 144

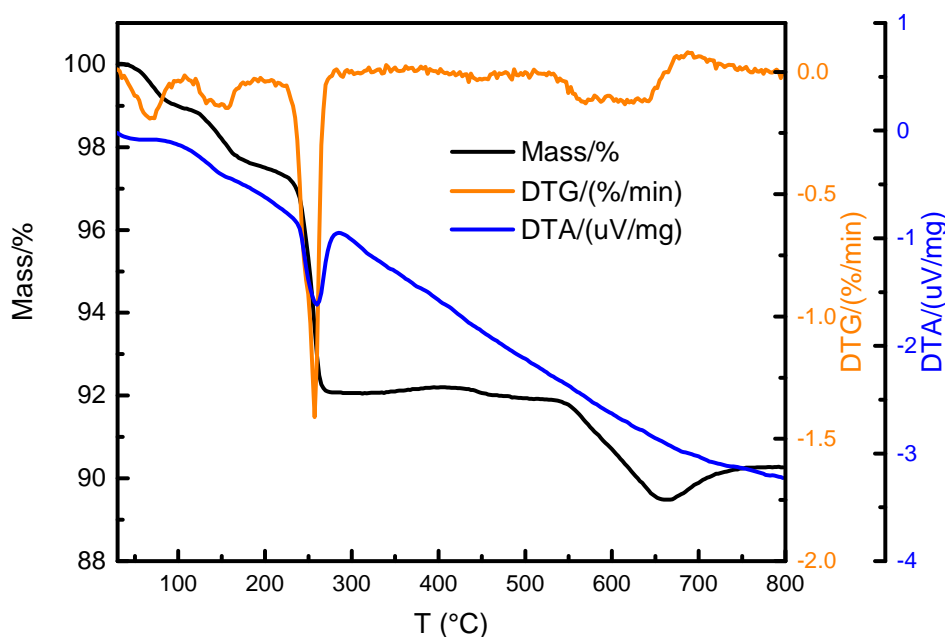
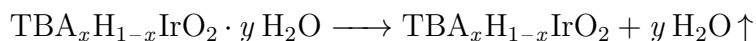


Figure C.2: DTA-TG curve of $\text{TBA}_x\text{IrO}_2 \cdot y\text{H}_2\text{O}$ heated in air with 5 K / min to 800 °C, with first derivative of the TG signal as an indicator for mass change processes.

°C were interpreted as the loss of textural and interlayer water according to:



The mass loss at $T = 144$ °C was interpreted as the decomposition of the interlayer TBA^+ ions by a Hofmann elimination, resulting in gaseous tributylamine and 1-butene as well as a proton which stays in the interlayer space according to:



The final mass loss at 550 °C was interpreted as the decomposition of IrOOH to IrO_2 and oxidation of remaining carbon and nitrogen impurities into the oxides.

D Miscellaneous

D.1 List of Publications

The results compiled in this thesis were either published in scientific journals or are in preparation for submission as detailed in the following list. Publications exceeding the scope of this thesis are not included in the previous chapters and are compiled in a separate list.

D.1.1 Publications within this Thesis

Magnetic properties of restacked 2D spin1/2 honeycomb RuCl_3 nanosheets

Daniel Weber, Leslie M. Schoop, Viola Duppel, Judith M. Lippmann, Jürgen Nuss, Bettina V. Lotsch

Nano Letters **2016**, *16*, 3578–3584, DOI: 10.1021/acs.nanolett.6b00701.

Trivalent Iridium Oxides: Layered Triangular Lattice Iridate $\text{K}_{0.75}\text{Na}_{0.25}\text{IrO}_2$ and Oxyhydroxide IrOOH

Daniel Weber, Leslie M. Schoop, Daniel Wurmbrand, Jürgen Nuss, Robert E. Dinnebier, Bettina V. Lotsch

Submitted to Chemistry of Materials

Synthesis and Electrocatalytic Properties of $[\text{IrO}_2]^{x-}$ Nanosheets

Daniel Weber, Leslie M. Schoop, Daniel Wurmbrand, Sourav Laha, Viola Duppel, Bettina V. Lotsch
in preparation

D.1.2 Publications beyond this Thesis

Biogenic metal-organic frameworks: 2,5-Furandicarboxylic acid as versatile building block

Marcus Rose, Daniel Weber, Bettina V. Lotsch, Reinhard K. Kremer, Richard Goddard, Regina Palkovits
Microporous and Mesoporous Materials **2013**, 181, 217-221, DOI: 10.1016/j.micromeso.2013.06.039.

Tuning the magnetoresistance of ultrathin WTe_2 sheets by electrostatic gating

Junhong Na, Alexander Hoyer, Leslie Schoop, Daniel Weber, Bettina M. Lotsch, Marko Burghard, Klaus Kern
Nanoscale **2016**, 8, 18703-18709, DOI: 10.1039/C6NR06327F.

Temperature dependent magnetic anisotropy in the layered magnetic semiconductors CrI_3 and CrBr_3

Nils Richter, Daniel Weber, Franziska Racky, Nirpendra Singh, Udo Schwingenschlögl, Bettina V. Lotsch, Mathias Kläui
Submitted to Physical Review Materials

Electronic transport in thin flakes of $\alpha\text{-RuCl}_3$

Daniel Weber, Soudabeh Mashhadi Sheikholharam, Leslie M. Schoop, Armin Schulz, Jürgen Nuss, Marko Burghard, Klaus Kern, Bettina V. Lotsch
In preparation

D.2 Conference Contributions & Talks

The structure and magnetism of restacked spin-1/2 honeycomb RuCl_3 single layers (poster presentation)

Daniel Weber, Leslie M. Schoop, Viola Duppel, Judith M. Lippmann, Jürgen Nuss, Bettina V. Lotsch

Workshop on Spins, Valleys, and Topological States in 2D and Layered Materials, June 2017, Columbus, OH, USA

The structure and magnetism of restacked spin-1/2 honeycomb RuCl_3 single layers (poster presentation) s Daniel Weber, Leslie M. Schoop, Viola Duppel, Judith M. Lippmann, Jürgen Nuss, Bettina V. Lotsch

Physics of Emergent Materials, May 2017, Columbus, OH, USA

Magnetic Properties of Turbostratically Restacked spin- $\frac{1}{2}$ honeycomb RuCl_3 monolayers (oral presentation)

Daniel Weber, Leslie M. Schoop, Viola Duppel, Judith M. Lippmann, Jürgen Nuss, Bettina V. Lotsch

John Hopkins University, Invited Talk, July 2016, Baltimore, MD, USA

Magnetic Properties of Turbostratically Restacked spin- $\frac{1}{2}$ honeycomb RuCl_3 monolayers (oral presentation)

Daniel Weber, Leslie M. Schoop, Viola Duppel, Judith M. Lippmann, Jürgen Nuss, Bettina V. Lotsch

Ohio State University, Invited Talk, July 2016, Columbus, OH, USA

Magnetic Properties of Turbostratically Restacked spin- $\frac{1}{2}$ honeycomb RuCl_3 monolayers (poster presentation)

Daniel Weber, Leslie M. Schoop, Viola Duppel, Judith M. Lippmann, Jürgen Nuss, Bettina V. Lotsch

Gordon Research Conference - Solid State Chemistry 2016, New London, NH, USA

Magnetic Properties of Turbostratically Restacked spin- $\frac{1}{2}$ honeycomb RuCl₃ monolayers (poster presentation)

Daniel Weber, Leslie M. Schoop, Viola Duppel, Judith M. Lippmann, Jürgen Nuss, Bettina V. Lotsch

Gordon Research Seminar - Solid State Chemistry 2016, New London, NH, USA

Single Layers of Magnetic Semiconducting RuCl₃ - A True 2D Honeycomb Lattice (oral presentation)

Daniel Weber, Leslie M. Schoop, Viola Duppel, Judith M. Lippmann, Jürgen Nuss, Bettina V. Lotsch

Gordon Research Seminar - Solid State Chemistry 2016, New London, NH, USA

Magnetic Properties of Turbostratically Restacked spin- $\frac{1}{2}$ honeycomb RuCl₃ monolayers (poster presentation)

Daniel Weber, Leslie M. Schoop, Viola Duppel, Judith M. Lippmann, Jürgen Nuss, Bettina V. Lotsch

Spring Meeting of the German Physical Society (DPG) 2016, Regensburg, Germany

Magnetic Properties of Turbostratically Restacked spin- $\frac{1}{2}$ honeycomb RuCl₃ monolayers(oral presentation)

Daniel Weber, Leslie M. Schoop, Viola Duppel, Judith M. Lippmann, Jürgen Nuss, Bettina V. Lotsch

Pacificchem Conference 2015, Honolulu, HI, USA

Chromium Trihalide Single Layers - Ferromagnetic Insulators on the Nanoscale

(poster presentation)

Daniel Weber, Leslie M. Schoop, Alexander Kuhn, Bettina V. Lotsch

Chemistry Meets Physics Ringberg Meeting 2015, Schloss Ringberg, Germany

2D Single Crystals - A Chemist's Perspective (oral presentation)

Daniel Weber, Bettina V. Lotsch

Invited Talk at North Arizona University 2014, Flagstaff, AZ, USA

Copper(II) Furan-2,5-dicarboxylate Investigation of Structure, Magnetic and Sorption Behaviour (poster presentation)

Daniel Weber, Marcus Rose, Reinhard K. Kremer, Regine Palkovits and Bettina V. Lotsch

Solid State Symposium 2012, Stuttgart, Germany

D.3 Curriculum Vitae

D.3.1 Personal Details

Name	Daniel Weber
Date of Birth	13.06.1985
Place of Birth	München, Germany
Nationality	German

D.3.2 Education

02/2017 PhD defense, LMU Munich, Germany

PhD work done in the group of Bettina V. Lotsch,
MPI for Solid State Research, Stuttgart, Germany

07/2011 Master of Science - Chemistry, Ludwig Maximilian University,
Munich, Germany, top 10 % of graduates

02/2009 Bachelor of Science, Chemistry and Biochemistry, Ludwig
Maximilian University, Munich, Germany